# Lung Cancer On-Chip for Immunotherapy Response Profiling

Irina Veith

Thèse de doctorat

NNT : 2020UPASL036

université PARIS-SACLAY

# Lung cancer on-chip for immunotherapy response profiling

**Thèse de doctorat de l'université Paris-Saclay**

École doctorale n° 582 cancérologie: biologie-médecine–santé (CBMS)
Spécialité de doctorat : science de la vie et de la santé
Unité de recherche : unité 830 Inserm cancer, hétérogénéité, instabilité et plasticité (CHIP)
Référent : Faculté de médecine

**Thèse présentée et soutenue à Paris, le 23/11/2020, par**

**Irina Veith**

## Composition du Jury

| | |
|---|---|
| **Eric Deutsch**<br>PU, Institut Gustave Roussy | Président |
| **Emmanuel Donnadieu**<br>DR2 CNRS, Institut Cochin | Rapporteur & Examinateur |
| **Pablo Vargas**<br>CR1 INSERM, Institut Curie | Rapporteur & Examinateur |
| **Eliane Piaggio**<br>DR2 INSERM, Institut Curie | Examinatrice |
| **Nicolas Girard**<br>Pr., Institut du thorax Curie-Montsouris | Examinateur |
| **Maria Carla Parrini**<br>Dr., Institut Curie | Directrice de thèse |
| **Hamasseh Shirvani**<br>Dr., Institut Roche | Co-encadrante de thèse |

*Dubium sapientiae initium*

René Descartes

**Université Paris-Saclay**
Espace Technologique / Immeuble Discovery
Route de l'Orme aux Merisiers RD 128 / 91190 Saint-Aubin, France

université PARIS-SACLAY | ÉCOLE DOCTORALE Cancérologie : biologie - médecine - santé (CBMS)

# I Abstract

**Title: Lung cancer on-chip for immunotherapy response profiling**

**Keywords:** cancerology, immunotherapy, precision medicine, microfluidics, tumors-on-chip

**Abstract**: Non-small cell lung cancer (NSCLC) is one of the few tumor diseases, with melanoma and vesical carcinoma, for which immuno-oncology drugs led to a therapeutic revolution. Only 20 to 30% of the NSCLC patients benefit from immune checkpoint inhibitors (ICI) monotherapy with durable responses, while combinations led up to 40% of long responder patients. Our study aims to better characterize the modulation of the tumor microenvironment upon ICI treatment, plus or minus concurrent chemotherapy, in order to guide more compelling immunotherapy strategies.

Inspired by the organ-on-a-chip technology, we implemented the reconstitution ex vivo of a simplified immunocompetent lung tumor microenvironment by performing 3D co-cultures in microfluidic devices. This approach allowed us to perform live-imaging and quantification of the effects of ICI on the tumor ecosystem.

The design of the chip consists of three parallel micro-chambers, separated by micro-pillars that allow the confinement of a biomimetic hydrogel in the central channel by capillarity. By co-culturing autologous NSCLC cells and cytotoxic T lymphocytes (harvested from the TILs of the same patient and furtherly amplified in vitro) we could recapitulate, visualize and quantify an efficient and specific cytotoxic activity of the T cells against the autologous cancer cells. For this purpose, we developed a novel algorithm that could localize the cancer

cells and, thanks to a fluorescent reporter of the caspase activity, measure their death in a time- and space-specific manner. In these 3D co-cultures the cytotoxic activity of T cells was enhanced by the treatment with PD-1 inhibitor and PD-L1 inhibitor, therefore reconstituting on-chip an ICI response. Furthermore, this method allowed us to extract a parameter, the potential of death induction, which mathematically estimates the "contagiousness of death" by computing the proximity in space and time of death signals. Interestingly, this analysis revealed us that the death of cancer cells caused by either chemotherapy or cytotoxic T cells is contagious, whereas in control conditions the cancer cells death is stochastic.

Furthermore, in order to have a molecular insight on the impact of the co-culture on T cells, in presence or absence of ICI, we analyzed by flow cytometry the expression of several T cell markers. After 3 days of co-culture on chip, the T cells showed an increased expression of activation markers, such as CD69 and CD25, as well as an increased expression of exhaustion markers, notably PD-1, TIGIT, TIM-3, LAG-3, CD137 and OX-40. The coupling of image analysis and the study of T cell plasticity, allowed us to associate for the first time the finely quantified cytotoxic activity of the T cells and their activation/exhaustion status and describe a responsive phenotype to immunotherapies.

In this thesis, we demonstrated that the tumor-on-chip is suitable to evaluate the efficacy of immune checkpoint inhibitors, to potentially assess the effect of combined drugs and to study the mechanisms of cancer cell primary resistance.

**Titre: Caractérisation de la réponse à l'immunothérapie sur puce microfluidique dans un modèle de cancer du poumon**

**Mots clés:** cancérologie, immunothérapie, médecine de précision, microfluidique, tumeurs-sur-puce

**Résumé:** Le cancer du poumon non à petites cellules (CPNPC) est l'une des rares maladies tumorales, avec mélanome et carcinome vésical, pour lesquelles les médicaments immuno-oncologiques ont conduit à une révolution thérapeutique. Seuls 20 à 30% des patients atteints de CPNPC bénéficient de la monothérapie avec inhibiteurs des points de contrôle immunitaires (ICP) avec des réponses durables, tandis que les combinaisons ont conduit à réponse longue dans jusqu'à 40% des patients. Notre étude vise à mieux caractériser la modulation du microenvironnement tumoral lors d'un traitement ICP, plus ou moins une chimiothérapie concomitante, afin de guider des stratégies d'immunothérapie plus convaincantes.

Inspiré par la technologie d'organes sur puce, nous avons reconstitué *ex vivo* un microenvironnement de tumeur pulmonaire immunocompétent simplifié en réalisant des co-cultures 3D dans des dispositifs microfluidiques. Cette approche nous a permis de réaliser une imagerie en direct et une quantification des effets de l'ICP sur l'écosystème tumoral.

L'architecture de la puce se compose de trois micro-chambres parallèles, séparées par des micro-piliers qui permettent le confinement d'un hydrogel biomimétique dans le canal central par capillarité. En co-cultivant des cellules CPNPC et des lymphocytes T cytotoxiques autologues (récoltés à partir des TIL du même patient et amplifiés ultérieurement *in vitro*), nous pourrions récapituler, visualiser et quantifier une activité cytotoxique efficace et spécifique des cellules T contre les cellules cancéreuses autologues.

Pour cela, nous avons développé un nouvel algorithme qui pourrait localiser les cellules cancéreuses et, grâce à un rapporteur fluorescent de l'activité caspase, mesurer leur mort d'une manière spécifique au temps et à l'espace. Dans ces co-cultures 3D, l'activité cytotoxique des cellules T a été renforcée par le traitement avec l'inhibiteur PD-1 et l'inhibiteur PD-L1, reconstituant ainsi sur puce une réponse ICI. De plus, cette méthode nous a permis d'extraire

un paramètre, le potentiel d'induction de la mort, qui estime mathématiquement la «contagiosité de la mort» en calculant la proximité dans l'espace et le temps des signaux de mort. Fait intéressant, cette analyse nous a révélé que la mort des cellules cancéreuses causée par la chimiothérapie ou par les cellules T cytotoxiques est contagieuse, alors que dans les conditions témoins, la mort des cellules cancéreuses est stochastique.

De plus, afin d'avoir un aperçu moléculaire de l'impact de la co-culture sur les cellules T, en présence ou en l'absence d'ICI, nous avons analysé par cytométrie de flux l'expression de plusieurs marqueurs de cellules T. Après 3 jours de co-culture sur puce, les lymphocytes T ont montré une expression accrue des marqueurs d'activation, tels que CD69 et CD25, ainsi qu'une augmentation de l'expression des marqueurs d'épuisement, notamment PD-1, TIGIT, TIM-3, LAG- 3, CD137 et OX-40. Le couplage de l'analyse d'image et de l'étude de la plasticité des lymphocytes T, nous a permis d'associer pour la première fois l'activité cytotoxique finement quantifiée des lymphocytes T avec leur statut d'activation / épuisement et de décrire un phénotype réactif aux immunothérapies.

Dans cette thèse, nous avons démontré que la tumeur-sur-puce peut être exploité pour évaluer l'efficacité des inhibiteurs de points de contrôle immunitaires, potentiellement pour déterminer l'effet de médicaments combinés et enfin pour étudier les mécanismes de résistance primaire des cellules cancéreuses.

# II List of Abbreviations

Ab: antibody

mAb: monoclonal antibody

ADCC: antibody-dependent cell cytotoxicity

Akt: protein kinase B

ALK: anaplastic lymphoma kinase

AP-1: activator protein 1

APC: antigen presenting cell

BATF: Basic Leucine Zipper ATF-Like Transcription Factor

BEC: blood endothelial cells

BLIMP1: B-lymphocyte-induced maturation protein 1

BRAF: B-Raf

BRCA2: breast cancer 2

CAF: cancer associated fibroblast

CAF-S1: CAF-subtype 1

CAF-S2: CAF-subtype 2

CAF-S3: CAF-subtype 3

CAF-S4: CAF-subtype 4

CAR-T: Chimeric Antigen Receptor T-cell

CCL: C-C Motif Chemokine Ligand 2

CD: cluster of differentiation

CDKN2A: Cyclin Dependent Kinase Inhibitor 2A

Ceacam-1: Carcinoembryonic antigen-related cell adhesion molecule 1

CHEK2: Checkpoint Kinase 2

CHRNA: neuronal acetylcholine receptor subunit alpha

CHT: circular hough transform

COPD: chronic obstructive pulmonary disease

COX-2: cyclooxygenase 2

CPNPC: cancer du poumon non à petites cellules

CTL: cytotoxic T lymphocyte

CTLA-4: Cytotoxic T-Lymphocyte Antigen 4

CXCL: chemokine (C-X-C motif) ligand

CyTOF:

DAMP: damage associated molecular patterns

DC: dendritic cells

DNA: deoxyribonucleic acid

DPP4: dipeptidyl peptidase-4

EC: endothelial cell

ECM: extracellular matrix

EGFR: epithelial growth factor

EMA: European medicine agency

EML4: Echinoderm microtubule-associated protein-like 4

EMT: epithelial-mesenchymal transition

ES: embryonic stem cells

FACS: fluorescence-activated cell sorting

FAP: fibroblast activation protein

FasL: Fas ligand

FDA: food and drug administration

FGF: fibroblast growth factor

FGFR1: fibroblast growth factor receptor 1

FLG-1: fibrinogen-related protein 1

FOXP3: forkhead box protein P3

FSC: forward scatter

FSP1: fibroblast specific protein 1

GEP: gene expression profile

GITR: glucocorticoid-induced TNFR-related protein

GNI: gross national income per capita

GWAS: genome-wide association studies

HAVCR2: see TIM-3

HDI: human development index

HER: Receptor tyrosine-protein kinase erbB-2

HIF: hypoxia inducible factor

HIV: human immunodeficiency virus

HLA: human leukocyte antigen

HMGB-1: high-mobility group box 1

HPV: human papilloma virus

ICI: immune checkpoint inhibitors

IDO: indoleamine 2,3-dioxygenase

IFCT: French Cooperative Thoracic Intergroup

IFN-γ: interferon gamma

IGR-Heu: Institut Gustave Roussy- patient Heu

IGR-Pub: Institut Gustave Roussy- patient Pub

IL: interleukin

IPF: idiopathic pulmonary fibrosis

irAE: immune-related adverse event

IRF: interferon regulative factor

ITAM: Immunoreceptor Tyrosine-based Activation Motif

ITIM: Immunoreceptor Tyrosine-based Inhibition Motif

ITSM: Immunoreceptor Tyrosine-based Switch Motif

ITT: Ig Tail-Tyrosine-like

KEAP1: Kelch-like ECH-associated protein 1

KO: knockout

LAG-3: lymphocyte activation gene-3

LAP: LAG-3-associated protein

LAX: Lymphocyte transmembrane adapter 1

LCC: large cell carcinoma

LSECtin: liver sinusoidal endothelial cell lectin

LUAD: lung adenocarcinoma

LUSC: lung squamous carcinoma

MAPK: mitogen-activated protein kinase

MDSC: myeloid derived suppressive cell

MFI: mean fluorescence intensity

MHC: major histocompatibility complex

myCAF: myofibroblastic CAF

NFAT: Nuclear factor of activated T-cells

NF-κB: nuclear factor kappa-light-chain-enhancer of activated B cells

NHLF: normal human lung fibroblasts

NK: natural killer

NO: nitric oxyde

NOS: Nitric oxide synthase

NSCLC: non small cell lung cancer

OoC: organ on chip

OX-40: tumor necrosis factor receptor superfamily, member 4

PAMP: pathogen associated molecular pattern

PD-1: programmed death 1

PDGF: platelet derived growth factor

PDGFR-β: Platelet-derived growth factor receptor beta

PD-L1: programmed death-ligand 1

PD-L2: programmed death-ligand

PDPN: podoplanin

PGE2: Prostaglandin E2

PI3K: phosphatidylinositol 3-kinase

PI3KCA: Phosphatidylinositol 4,5-bisphosphate 3-kinase catalytic subunit alpha isoform

PLC-γ: phospholipase C gamma

PRR: Pattern Recognition Receptor

PtdSer: Phosphatidylserine

PTEN: phosphatase and tensin homolog

PVR: poliovirus receptor

RB1: retinoblastoma 1

RET: rearranged during transfection

RNA : ribonucleic acid

ROI : region of interest

ROS : reactive oxygen species

SCLC : small cell lung cancer

scRNA-seq : single cell RNA sequencing

SLC34A2: solute carrier family 34 member 2

SSC: side scatter

STAMP: spatio-temporal apoptosis mapper

STAT: signal transducer and activator of transcription

STK11: Serine/Threonine Kinase 11

TAM: tumor associated macrophage

TAN: tumor associated neutrophil

TCF1: T-cell factor 1

TCR: T cell receptor

TDO: tryptophan 2,3-dioxygenase

TERT: telomerase reverse transcriptase

TGF-β: transforming growth factor beta

Th: T helper

TIGIT: T cell immunoreceptor with Ig and ITIM domains

TIL: tumor infiltrating lymphocyte

TIM-3: T cell immunoglobulin and mucin-domain containing protein- 3

TIME: tumor immune microenvironment

TKI: tyrosine kinase inhibitor

TLS: tertiary lymphoid structures

TMB: tumor mutational burden

TME: tumor microenvironment

ToC: tumor on chip

TOX: thymocyte selection-associated high mobility group box protein

TP53: tumor protein 53

TRAIL: TNF-related apoptosis-inducing ligand

$T_{reg}$: regulatory T cell

TRIM: tripartite motif protein

$T_{RM}$: resident memory T cell

TSLP: thymic stromal lymphopoietin

UICC: International Cancer Control

VEGF: vascular endothelial growth factor

WHO: world health organization

WT: wildtype

ZAP-70: Zeta-chain-associated protein kinase 70

α-SMA: alpha smooth muscle actinin

# III List of Figures

# IVList of Tables

# V Table of Contents

# 1 Introduction

## 1.1 Lung cancer

The first chapter of the thesis will describe some clinical and epidemiologic aspects of lung cancer, in order to illustrate the impact of this disease on the global population and the current standard of care. Due to the high frequency and the very low survival rates, it is of crucial importance to improve the understanding of the evolving features the disease, in order to establish more compelling and personalized treatments. Indeed, the study of lung cancer genetic heterogeneity led to the identification of 'actionable' molecular alterations, which nowadays are targetable with specific inhibitors. In addition, the encouraging results obtained in clinics upon immunotherapy treatment of advanced lung cancers, raised the interest of the immune-oncology field on the question of which are the key factors that elicit a good response.

### 1.1.1 Lung cancer epidemiology

I herein describe the epidemiology and etiology of lung cancer in order to address the world-wide amplitude and impact of lung cancer disease. Statistical data retrieved from epidemiological studies helped to assess the etiology of the disease, identify the risk factors and develop policies and social protective strategies in order to prevent the disease.

Lung cancer is the worldwide leading cause of cancer-related deaths. In 2018, 2.1 million (M) new cases of lung cancer were estimated and accounted for 1.76 M deaths, being the 1$^{st}$ cause of death for cancer in men and 4$^{th}$ in women (after breast, cervix/uteri, colorectum) [1]. Combining both sexes, lung cancer is the most commonly diagnosed cancer, accounting for 11.6% of worldwide cancer diagnosis.

The difference of incidence and mortality between genders may be attributed to the historical difference in tobacco consumption. In a systematic review and meta-analysis of prospective cohort studies reporting sex-specific relative risk of lung cancer associated with smoking, O'Keeffe and colleagues concluded that smoking yields similar risks between sexes. In fact, data coming from 99 cohorts and 7 million individuals showed that the pooled women-

to-men ratio of relative risk was 0.92 [2]. In the United States, the increased number of women smoking in the past 20 years resulted in an increased risk of death of lung cancer, which almost reached the risk observed in men [3].

The distribution of lung cancer incidence varies between countries worldwide. As reported in the Globocan 2018, released by the World Health Organization (WHO), incidence and mortality are higher in countries with high Human Development Index (HDI) in both men and women [4]. The HDI is an average of key well being indexes of including life expectancy, the education index and the GNI (gross national income per capita). The correlation between higher incidence and higher HDI could be explained with the smoking social custom, rooted in high HDI countries.

The 5-years survival rate in lung cancer remains poor due to late diagnosis, which often occurs in advanced stages. Unfortunately, the 5-year relative survival rate is only 19% in all lung cancers (23% in Non-small cell lung cancer (NSCLC) and 6% in Small-cell lung cancer (SCLC)) [5].

Multiple risk factors concur in lung cancer development, including behavioral (e.g. smoking), environmental and genetic factors. Tobacco is a main risk factor, causing from 80% to 90% of all lung cancers [6]. Environmental risk factors include the occupational exposure to carcinogens, among which asbestos is the most common, radon exposure, pollution and air quality [7], infections caused by *Mycombacterium tuberculosis*, Human Immunodeficiency viruses (HIV), Human Papillomavirus (HPV) [8].

Regarding the genetic risk factors, a first major susceptibility locus influencing lung cancer risk was first identified by Bailey-Wilson and colleagues in a region on the 6q23-25 [9]. With the advent of genome-wide association studies (GWAS), nowadays a number of susceptibility loci are associated with lung cancer occurrence. These studies allowed the identification of several lung cancer-predisposing genes, namely CHRNA3, CHRNA5, TERT, HLA, BRCA2 ad CHEK2 [10] [11]. CHRNA3 and CHRNA5 encode the cholinergic receptor nicotinic alpha 3 and 5 subunit, respectively. TERT codes for the telomerase reverse transcriptase, the catalytic subunit of the telomerase complex; this complex elongates the DNA strands of telomeres,

allowing cells to overcome senescence and apoptosis. HLA (Human Leucocyte antigen) gene encodes the Major Histocompatibility complex (MHC), essential for antigen presentation to immune cells. Mutations or deletions in the MHC are found in different cancer types capable of evading the immune system. BRCA2 and CHK2 are tumor suppressor genes implied in the homologous recombinational repair of double strand breaks in DNA.

### 1.1.2 Histological classification and genetic characterization

Lung cancer is mainly classified in Non-small cell lung cancer (NSCLC) (85% of cases) and Small-cell lung cancer (SCLC) (15% of cases).

NSCLC include different histological subtypes; lung adenocarcinoma (LUAD) represents the majority of them (40%), 25% to 30% of other subtypes are classified as squamous carcinoma (LUSC) whether large cell carcinoma (LCC) represents the remaining 10 to 15%. NSCLC not otherwise specified (NOS) refer to all the NSCLC that cannot be classified by the previously described histological types. The 2015 WHO classification of tumors of the lung, introduces standardized criteria to diagnose small biopsies (bronchoscopic, needle, or core biopsies) and cytology [12]. Therewith, the severity of the disease is assessed by the TNM classification of Malignant Tumors, developed by the Union for International Cancer Control (UICC). The TNM staging system takes into consideration the size of the original tumor (T0-4), the involvement of proximal lymph nodes (N0-3) and the presence of metastasis in distant organs (M0-1) [13].

As shown by Lawrence and colleagues [14] in Figure 1, lung cancer harbors with melanoma the highest somatic mutation frequency among all cancers. Interestingly, the most mutated cancers are associated with better responses to immunotherapies.

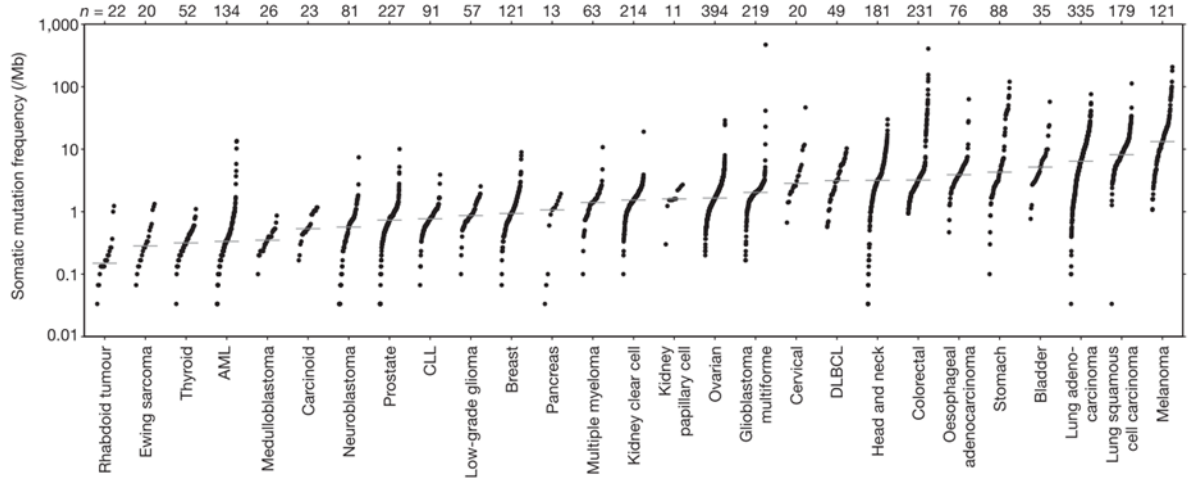


*Figure 1: Somatic mutation frequencies observed in various cancers.*

*Mutation frequencies detected in exomes from 3,083 tumor–normal pairs, adapted from Lawrence et al. Nature 2013.*

Lung cancer is a heterogeneous disease and the identification of molecular alterations led towards more personalized and effective therapies. Several studies established the frequency of statistically significant somatic mutations in the different histological subtypes, as summarized in Table 1.

*Table 1: Recurring genetic alterations in lung cancer subtypes*

| Gene | Type of alteration | Frequencies in LUAD | Frequencies in LUSC | Frequencies in SCLC |
|---|---|---|---|---|
| TP53 | Inactivating mutation | 46% | 81% | 99% |
| RB1 | Inactivating mutation | 4% | 7% | 90% |
| EGFR | Activating mutation | 14% | 9% | N/A |
| KEAP1 | Inactivating mutation | 17% | 12% | N/A |
| STK11 | Inactivating mutation | 17% | 2% | N/A |
| ALK | Rearrangement | 1.3% | <1% | N/A |
| FGFR1 | Activating mutation/ Amplification | N/A | 20% | 6% |
| KRAS | Activating mutation | 33% | 2% | N/A |
| PIK3CA | Mutation | Very rare | 16% | 3% |
| PTEN | Mutation/homozygous deletion | Very rare | 8% | 9% |
| BRAF | Activating mutation | 10% | 4% | N/A |
| ROS1 | Rearrangement | 1.7% | N/A | N/A |
| MET | Rearrangement | 5% | N/A | N/A |
| CDKN2A | Inactivating mutation | 4% | 15% | N/A |
| SOX2 | Amplification | 6% | 65% | 27% |
| NOTCH1 | Mutation | 8% | 1% | 25% |
| MYC | Amplification | 25% | N/A | 16% |
| References | | [13] | [14] | [15] [16] [17] |

As illustrated in the table, the most frequently mutated genes are TP53 and KRAS. TP53, also called the "guardian of the genome", codes for p53 which functions as tumor suppressor. In normal conditions p53 is in an inactive state in complex with mdm2; under stress conditions (DNA damage, oxidative stress, ribonucleotides depletion or osmotic shock), p53 can arrest

the cell cycle, induce the DNA reparation program and induce apoptosis of irreparably damaged cells. KRAS is an oncogene encoding K-ras, a membrane-bound small GTPase implicated in the MAPK signaling cascade. This signaling pathway is downstream several growth factor receptors and activating mutations lead to uncontrolled cell proliferation and survival.

Interestingly, it is reported that EGFR and KRAS mutations are mutually exclusive [15] [16]. This observation could be explained by the fact that these mutations involve the same signaling pathway, therefore the coexistence would be redundant and it would not undergo a selective pressure.

It is thought that smoking is a main cause of the genetic heterogeneity in lung cancer. In fact, tumors harboring EGFR oncogenic mutation, or ALK and ROS rearrangements, observed more frequently in never smokers, present less genetic complexity and occur more frequently in never smokers [17] [18]. EGFR mutations sensitizing to tyrosin kinase inhibitors (TKI) are most frequently represented by exon 19 deletions or by the Leu858Arg substitution in exon 21. ALK rearrangements derive from inversions or translocations on chromosome 2 that fuse the exon 20 of ALK gene with other regions of another gene. EML4 is the most common partner gene in NSCLC ALK translocations, even though 27 variants of ALK have been observed. Similarly, the tyrosine kinase domain of ROS1, located on chromosome 6, can translocate and fuse with 14 different partner genes; the most common translocations are ROS1-CD74 and ROS1-SLC34A2 [19].

Interestingly, the genetic heterogeneity of lung cancer varies over time, depending on the mutations. For example, whereas LUAD harbor KRAS mutations independently from the grade/advancement of the tumors, TP53 mutations are more commonly found in advanced stages, suggesting a role in cancer progression [20]. In fact, the accumulation of TP53 muted cells is likely the result of the selective advantage gained by the more resistant cell clones.

Some studies linked specific mutations to poorer clinical outcomes and resistance to treatments. For instance, LKB1 alterations are linked to primary resistance to PD-1 inhibitors in KRAS mutated LUAD [21]. Similarly, Cristescu and collegues showed that STK11 and KEAP1 mutations in LUAD (and KEAP1 in LUSC) are negatively associated with high TMB (tumor

mutational burden) and T cell inflamed GEP (Gene Expression Profile), both markers of a positive response to anti-PD-1 therapies [22].

### 1.1.3 Lung cancer treatment

Lung cancer treatment is continuously evolving and immune checkpoint inhibitors represent a therapeutic breakthrough.

Various lung cancer treatments can be adopted, depending on tumor staging and the presence of actionable alterations. In fact, the comprehensive genome profiling of lung cancer allowed to identify oncogenic driver alterations, subsequently leading to the development of targeted therapies. In early stages of NSCLC (only 20% of patients), surgery is the advised therapeutic option. Generally, chemotherapy is considered the standard of care for lung cancer therapy. As indicated by a meta-analysis, preoperative chemotherapy increases the absolute survival benefit of 5-6% at 5 years for patients with IB-IIIA stages [23]. Locally advanced NSCLC (stages IIIA-B) are treated with thoracic radiotherapy plus chemotherapy. Ultimately, in case of metastatic lung cancers (stage IV) patients are treated with a combination of chemotherapy, radiation therapy, targeted therapy and immunotherapy.

The indications for chemotherapy administration vary depending on the stage and histology lung cancer subtypes. Neoadjuvant chemotherapy (administered before surgery) is used to reduce the size of the tumor before surgery, while adjuvant chemotherapy (after surgery) aims to clear up possible remaining cancer cells not detectable on imaging tests. Elseways, chemotherapy can be administered for locally advanced lung cancer, or stage IV metastatic lung cancer, where surgery would not be possible. More in detail, pemetrexed is indicated for patients with lung adenocarcinoma and taxol given in combination with carboplatin for large cell carcinoma. Pemetrexed is a folate antimetabolite which blocks cells proliferation. More in detail, it interferes with the production of DNA and RNA by inhibiting the enzymes involved in the synthesis of the precursors of pyrimidine nucleotides. Diversely, taxol targets tubulin and it prevents the microtubule polymer to disassemble. Its action results in defects of cell division and chromosomes segregation. Lastly, carboplatin is a platinum-based chemotherapy which forms crosslinks to DNA and impedes its replication.

NSCLC shows a specific tropism for the brain, which makes it one of the most common sources of brain metastases [24]. Radiation therapy, using high-energy rays able to damage cancer cells, can be of use to treat non-resectable tumors, especially in case of brain and bone metastasis. Nonetheless, some side effects, such as formation of necrotic tissue is one of the facets of side effects brought up by radiotherapy [25].

Targeted therapies are specific inhibitors developed against pro-tumorigenic features of the TME. The induction of angiogenesis is a hallmark of cancer. Specific monoclonal antibodies against VEGF, such as bevacizumab or ramucirumab, are used to treat advanced NSCLC. EGFR was the first mutated growth factor to be successfully targeted by specific inhibitors. These include tyrosine kinase inhibitors (TKI), such as erlotinib and gefitinib, or monoclonal antibodies [26], to mention cetuximab, targeting the extracellular portion of the receptor. Up to date, there are several approved drugs targeting activated EGFR, BRAF, KRAS and rearranged ALK, ROS1, MET and RET [27]. Even if the efficacy these inhibitors is improving, the average progression-free survival is approximately of 10 months. After this time, patients acquire mutations that induce resistance to the treatment leading to the progression of the disease. New-generation inhibitors aim to target multiple mutation in order to overcome or delay resistance.

In this context, a study conducted by the French Cooperative Thoracic Intergroup (IFCT) pointed out the importance of molecular profiling as standard care for NSCLC. In this 1 year-period study, patients with advanced NSCLC were routinely tested to seek for frequently mutated genes, namely EGFR, HER2, KRAS, BRAF and PIK3CA mutations and ALK rearrangements. Out of 17 664 patients with NSCLC, 50% harbored actionable genetic alterations and the results of molecular profiling affected the first-line treatment decision, resulting in improved progression-free survival and overall survival [28]. Younger patients, often never-smokers, are the ones who benefited the most from targeted therapies.

The interactions with the immune system play an important role in lung cancer initiation and progression. Therefore, a number of therapeutic strategies have been developed to act on

the immune system and boost its anti-tumor reactions. From 2015, with the advent of immunotherapies, patients with advanced NSCLC not presenting targetable gene driver mutations could benefit from immune checkpoint inhibitors (ICI) with durable responses [29]. Immune checkpoint inhibitors are a class of immunotherapies that either inactivate inhibitory immune checkpoints or bind activatory immune checkpoints with monoclonal antibodies, with the aim of "unleashing the breaks" of the immune system. The first inhibitory immune checkpoints to be targeted in clinics were against CTLA-4, such as ipilimumab, and against the PD1/PD-L1 axis, with nivolumab and pembrolizumab blocking PD-1 and atezolizumab targeting its ligand, PD-L1. Initially introduced in second line treatment of advanced NSCLC in combination with chemotherapy, in 2019 the the EMA (European Medicines Agency) and the FDA (Food and Drug Administration) approved the monotherapy with antibodies blocking the PD-1 axis as first-line treatment for PD-L1 expressing (≥1%) advanced NSCLC [30] [31].

In Figure 2 is illustrated the mechanisms of action of immune checkpoint blockade against CTLA-4 and PD1 or PD-L1: monoclonal antibodies impede the binding of inhibitory checkpoints (CTLA-4 and PD-1) with their respective ligands, therefore avoiding the generation of inhibitory signals in T cells (Figure adapted from [32]).

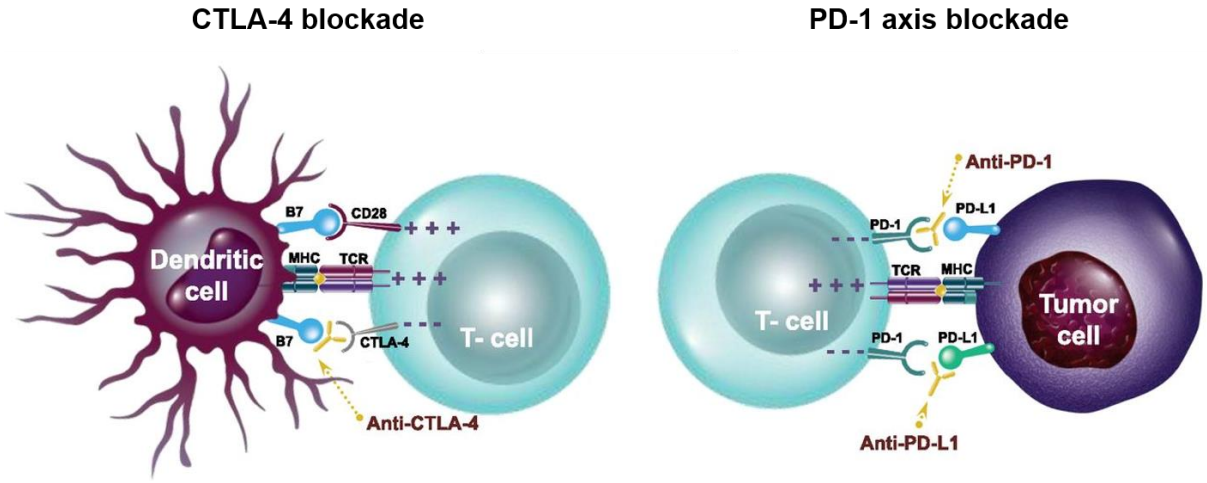


*Figure 2 : mechanism of action of monoclonal antibodies blocking CTLA-4 and PD-1.*

*CTLA-4 is an inhibitory receptor expressed on T cells. It binds with high affinity B7.1 and expletes its inhibitory functions by both competing for B7.1 binding with CD28 (an activatory receptor) and through CTLA-4 downstream inhibitory signals. Monoclonal antibodies (mAbs) targeting CTLA-4 disrupt its interaction with B7.1, thus blocking its inhibitory functions.*

*PD-1 is an inhibitory receptor on T cells. Its downstream signaling pathway dampens the activatory signals coming from the TCR and simultaneously conveys inhibitory signals. The interaction of PD-1 with its ligand, PD-L1, can be blocked by mAbs either targeting PD-1 or PD-L1.*

However, ICI treatments are effective only on 20-30% of the patients and it is of pivotal importance to identify the mechanisms that elicit an effective response in order to comply more adapted therapeutic strategies.

### 1.1.4 Tumor microenvironment of the lung.

The tumor microenvironment (TME) comprises a heterogeneous set of cells, including resident stromal cells and immune cells, but also the extracellular matrix in which are diffused many secreted factors.

In solid tumors, the tumor bed (parenchyma in a normal tissue) is distinguished from the stroma, composed of supportive structures, such as connective tissue, blood and lymphatic vessels. Cancer growth perturbs the surrounding resident cells and stimulates important cellular and architectural changes. The TME is not a passive bystander, as cells and factors within the TME are able to influence cancer cells survival, tumor invasion and response to treatment.

The TME composition varies in function of the type of cancer, both in term of cell types and ECM modeling. Figure 3 displays the cellular composition of the TME. Within the stroma, in addition of infiltrated immune cells (T cells, B cells, dendritic cells (DCs), NK cells, macrophage and neutrophils), the cell types commonly found in tumors include: blood and lymphatic endothelial cells (ECs), cancer-associated fibroblasts (CAFs), pericytes and sometimes adipocytes.

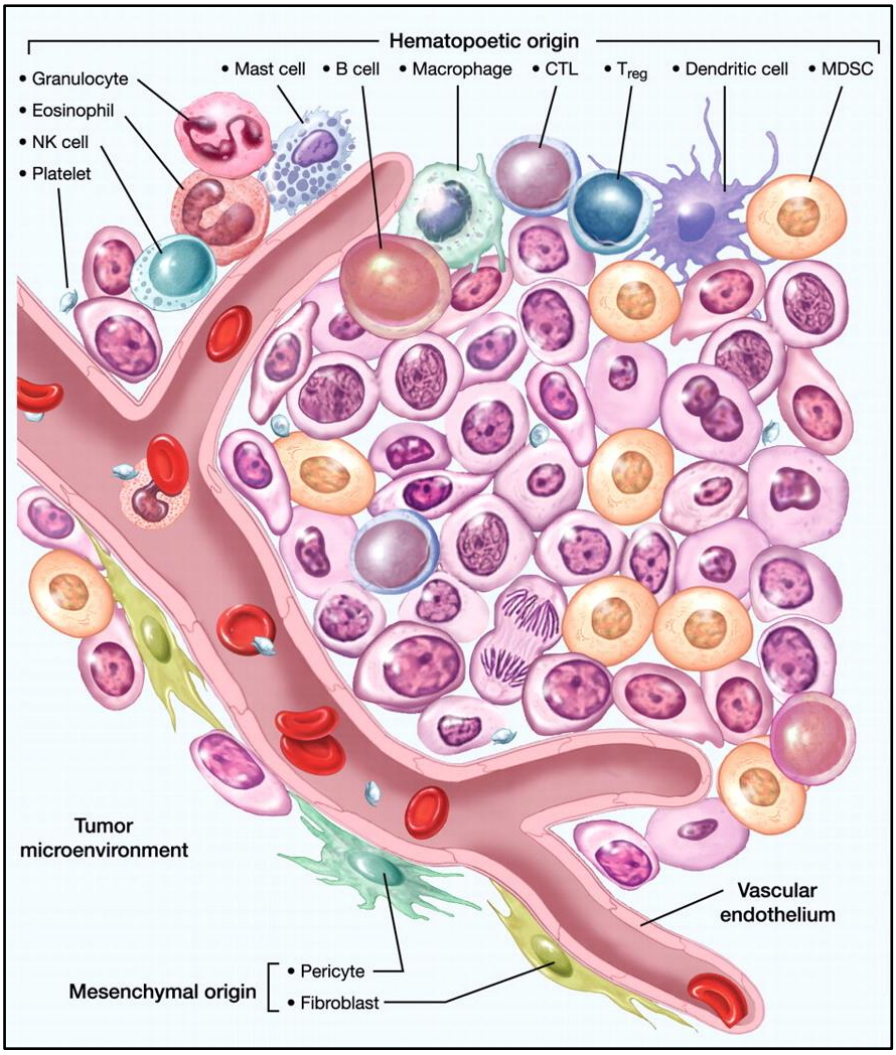


*Figure 3 : Cellular composition of the tumor microenvironment*

*The TME is consists of a variety of cell types that contribute to cancer growth and progression. Infiltrating immune cells include both cells from innate and adaptive immunity, such as neutrophils macrophages, DCs, MDSCs NK cells, CTLs, $T_{reg}$, B cells. Other cell types of mesenchymal origin contribute in shaping the TME, namely endothelial cells, pericytes and fibroblasts.*

### 1.1.4.i The vascular endothelium

In solid tumors, cancer cells growth is sustained by passive diffusion of soluble nutrients and oxygen. When the tumor mass reaches few $mm^3$ in volume, the TME becomes hypoxic and acidic (due to the accumulation of metabolic waste). Hypoxia-inducible factors (HIF) induce the secretion of platelet-derived growth factor (PDGF) and vascular endothelial growth factor A (VEGF-A), which stimulate endothelial cells proliferation and new blood vessels sprouting [33]. Indeed, angiogenesis is a hallmark of cancer and it is characterized by leaky vessels

(due to incomplete angiogenesis and lack of basal membrane secretion). In a study combining single-cell RNA-sequencing and proteomic (CyTOF) analysis of endothelial cells isolated from NSCLC patients, emerged a migratory and a basement-membrane remodeling breach phenotype [34]. These phenotypes could correlate a facilitated extravasation of cancer cells in the metastatic process and in the recruitment of immune cells to the tumor site.

#### 1.1.4.ii The extracellular matrix

The extracellular matrix serves as scaffold for the parenchyma and is composed of collagen fibers, proteoglycans, elastin and laminin. Integrins, present on the surface of cells, bind to the ECM fibers and transfer mechanotransduction signals through their intracellular association with actin filaments [35]. Additionally to the mechanical and structural support conferred by the ECM, this component of the TME stores cytokines and growth factors (VEGF, FGF, PDGF, TGF-β). During matrix remodeling, for instance by cells releasing metalloproteases, those factors are released in the TME, favoring tumor growth and neoangiogenesis. In solid tumors the ECM can constitute up to 60% of the total volume. Desmoplasia is defined as the accumulation of dense fibrotic tissue produced by fibroblasts [36] during tumor development and is associated to poor prognosis in pancreatic and breast cancer and to reduced response to treatments [37]. In lung, Idiopathic pulmonary fibrosis (IPF) is a chronic disease which has been described as a risk factor for lung carcinogenesis [38].

#### 1.1.4.iii The cancer-associated fibroblasts (CAFs)

Cancer-associated fibroblasts contribute to shape the TME in different ways. Mainly, the CAFs exert an immunosuppressive role through their secretome (either releasing immunosuppressive cytokines or attracting immunosuppressive cell types), the remodeling of the ECM, the interaction with the immune system and the metabolic-based immunosuppression [39]. The VEGF and TGF-β released by CAFs contribute to the neoangiogenic process. The latter may also induce the epithelial-mesenchymal (EMT) transition, an essential process in the initiation of cancer invasiveness. Moreover, the secretion of metalloproteases by CAFs degrades the ECM furtherly promoting cancer cell invasion [36]. Furthermore, CAFs recruit immunosuppressive population, such as MDSCs and $T_{reg}$ cells by releasing IL-6 and the chemokines CCL2, CXCL1, CXCL12 and CCL5 [40]. Interestingly, CAF in lung was detected the

presence of co-regulatory molecules on CAFs surface, namely PD-L1 and PD-L2, which dampen the antitumor response directly inhibiting the TILs [41]. Finally, CAF can release in the TME various enzymes whose action results in immunosuppression, such as cyclooxygenase-2 (COX-2), tryptophan 2,3-dioxygenase (TDO) and and indoleamine 2,3-dioxygenase (IDO). COX-2 is an enzyme involved in the synthesis of prostaglandins; in NSCLC prostaglandin E2 ($PGE_2$) was found to increase the production of IL-10, contributing to an immunosuppressive TME [42]. Similarly, TDO and IDO are enzymes involved in the metabolism of tryptophan, essential for immune cells; thus, the release of these enzymes depletes the tryptophan available in the TME, causing the formation of kynurenine suppressive metabolite [43].

CAFs include a heterogeneous population of fibroblasts. In the physiological process of wound healing, resident fibroblast are activated by TGF-β and become myofibroblasts. These cells express alpha muscle actin (α-SMA), highly contract the ECM and actively deposit matrix proteins. In analogy, the activated CAFs are called myCAF (myofibroblastic CAF) [39]. In our lab, Costa and colleagues characterized in breast cancer 4 different subtypes of CAFs through the differential expression of CAF markers in freshly isolated CAFs [44]. Among these subtypes, CAF-S2 and CAF-S3 are not activated resident fibroblasts, expressing low CD29, FAP and α-SMA. Instead, CAF-S1 and CAF-S4 highly express activation markers and were shown to have immunosuppressive [45] and pro-metastatic [46] characteristics, respectively. Moreover, thanks to single cell RNA-sequencing (scRNA-seq), our lab was able to identify 8 clusters within the CAF-S1 subtype and they correlate some of these clusters with an immunosuppressive environment, poor in CD8+ cytotoxic T cells and enriched in CD4+ Tregs cells expressing high levels of immune checkpoints, including PD-1 and CTLA4 [47]. These CAF-S1 clusters exist in different cancer types, including NSCLC. Importantly, specific CAF-S1 clusters were associated with primary resistance to immunotherapy in both melanoma and NSCLC patients; in particular, in a cohort of 79 patients with NSCLC treated at Bichat hospital, CAF-S1 subtype and specific CAF-S1 clusters were significantly enriched in non-responders [47].

### 1.1.4.iv The immune infiltrate

The immune system is composed of cells belonging to the innate immunity and to the adaptive immunity. Innate cells recognize in a non-specific way pathogen-associated molecular patterns (PAMPs), danger-associated molecular patterns (DAMPS), "non-self" antigens and initiate the immune response through inflammatory signals. Differently, the adaptive response is characterized by specificity towards a unique epitope and memory of it, building up a specialized response (through cytotoxic T cells and antibodies released by plasma cells).

Due to their genetic alterations, cancer cells express mutated proteins, which will be processed and exposed at the cancer cell surface bound to the major histocompatibility complex class I (MHC-I). These new "self" cancer-specific peptides, defined cancer neoantigens, can be recognized by $CD8^+$ T cells and rise an immune response against the tumor, as Boon and colleagues showed in 1994 [48]. Then, dendritic cells (DCs) will collect the antigens released by $CD8^+$-eliminated cancer cells and deliver them to the draining lymph nodes. Here, naïve T cells will be primed and these effector T cells will exit the lymph node, enter the bloodstream and reach the tumor, guided by chemokine gradients. In the chapter "tumor immunology" of this thesis, I will describe how this initial immune response against the tumor will shape the tumor, through the immunoediting process.

$CD3^+$ T cells represent the 40-50% of all $CD45^+$ infiltrate leukocytes in NSCLC [49]. Different T cell subtypes infiltrate the tumor and take part in responses within the TME. $CD8^+$ cytotoxic T lymphocytes, as described forehead, can detect tumor neoantigens expressed on the MHC-I complex and eliminate the cancer cells through the release of granzymes and perforines, resulting in the lysis of the cancer cell. Alternatively, these cells can induce the apoptosis cascade in the target cell through the engagement of the death receptor Fas (CD95) [50]. Moreover, $CD8^+$ T cells produce IFN-γ, which increases the expression of MHC-I molecules, promotes the differentiation towards $T_h1$ (T helper 1) cells, increases macrophages activity and inhibits angiogenesis [51]. $CD4^+$ cells can differentiate in a large number of subtypes, which contribute differently to immune responses. $T_h1$ promote inflammation and support $CD8^+$ survival releasing IL-2 and IFN-γ. Nonetheless, due to their contribution to

inflammation, high presence of $T_h1$in the TME is associated to a poor prognosis in NSCLC patients [52]. A profoundly different $CD4^+$ subtype, regulatory T cells ($T_{reg}$), is designated to the down modulation of the immune response, after the elimination of its cause. In brief, $T_{reg}$ cells are $CD4^+$ $CD25^+$ cells, characterized by the expression of FOXP3 (Forkhead box protein P3) transcription factor. In cancer $T_{reg}$ present immunosuppressive features, including consumption of IL-2 (necessary for other T cells survival), CTLA-4-mediated suppression of antigen presenting cells and secretion of immunosuppressive factors such as IL-10 and adenosine [53].

The infiltration of immune cells, in particular $CD8^+$ cytotoxic lymphocytes (CTLs), within the tumor core is a prognostic factor in lung cancer [54] [55]. Figure 4 illustrates the classes of tumor immune microenvironment (TIME) landscape, based on the immune infiltration. Figure from [56]. In an infiltrated-excluded TIME (Figure 4a), CTLs are excluded from the tumor core; these tumors are the so-called "cold" tumors due to the weak immune response. Contrarily, in case of an infiltrated-inflamed TIME (Figure 4b), activated CTLs (INF-γ-producing and expressing Granzyme B and programmed death 1 (PD-1)) and macrophages infiltrate the tumor core and build up an anti-tumor response. Cancer cells, as a mechanism of evasion from anti-tumor immunity overexpress PD-L1, the ligand of PD-1 inhibitory receptor on T cells. Tumors showing an infiltrated-inflamed TIMEs are often referred as "hot" tumors, known to respond better to immune checkpoint inhibitors treatments.

Lastly, the infiltrated TLS TIMEs are characterized by the association with tertiary lymphoid

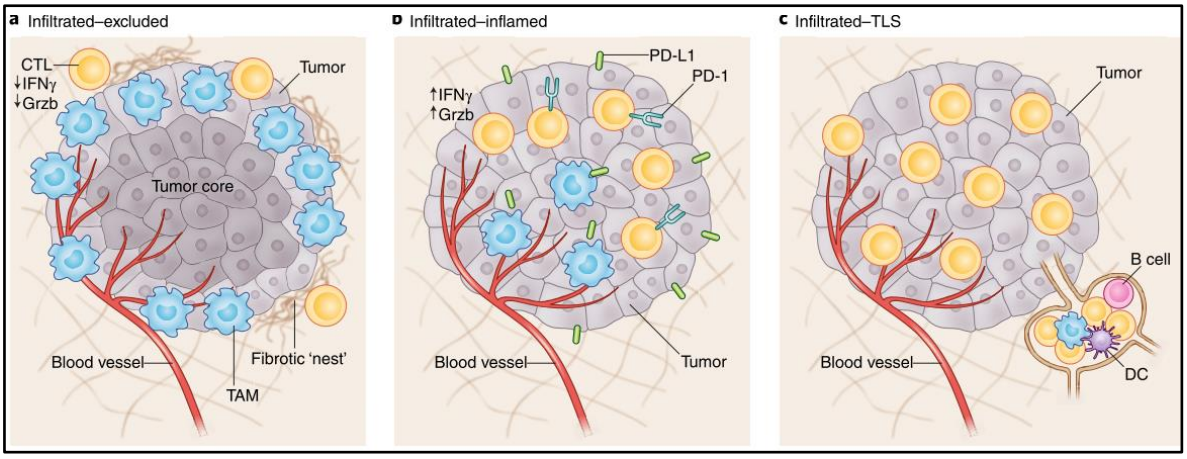


*Figure 4 Classes of tumor immune microenvironment.*

*Three classes of TIME include.* ***a)*** *in infiltrated-excluded TIMEs CTLs are excluded from the tumor core and are retained in tumor borders by fibrotic tissue or tumor-associated macrophages.* ***b)*** *Infiltrated-inflamed TIMEs are highly infiltrated by activated CTLs and PD-L1 is abundantly expressed on tumor and myeliod cells.* ***c)*** *infiltrated-TLS TIMEs present TLSs, aggregates of immune cells that organize in simplified structures similar to lymph nodes. TLS include B cells, dendritic cells and T cells.*

structures, found in the tumor margin and adjacent stroma. Tertiary lymphoid structures are "discrete and structured organizations of infiltrating immune cells" [57] which, differently from the primary and secondary lymphoid organs, form subsequently to chronic inflammation, autoimmune diseases and cancer. TLS commonly contain high endothelial venules, DCs, T cells and B cells and act as closer (to the tumor) priming and activation sites for immune cells. B cells are lymphocytes specialized in the production of antibodies, secretion of cytokines and antigen presentation. Normally, few B cells infiltrate the tumor and they are typically found in the draining lymph nodes of the tumor. In lung adenocarcinoma TLS accumulated near to the tumor margin; moreover, lesions presenting TLS showed a significantly increase in TILs infiltrated and less mononuclear phagocytes [58].

Innate immune cells (e.g. natural killer cells, neutrophils, macrophages, myeloid-derived suppressor cells) play multiple roles in the tumor microenvironment, with both antitumor and pro-tumor activities. The link between chronic inflammation and carcinogenesis, due to the persistent activity of the immune system, was established in different types of cancers [59].

Similarly, chronic obstructive pulmonary disease (COPD), a smoking-related disease, is associated with higher incidence and mortality in lung cancer [60]. Additionally, the increase of immune infiltration with the progression of the disease [61] underlies that the effector cells are over time inhibited by the TME.

Natural killer cells (NK) function is to kill cells infected by viruses and tumor cells. The absence of the MHC-I complex on cancer cells (frequent escape mechanism) will not engage the KIR (killer-cell immunoglobulin-like receptor) inhibitory receptors expressed on NK cells and will lead to killing of the target. However, the efficacy of NK cells in tumor containment is limited by the immunosuppressive TME.

Neutrophils, also called polymorphonucleates, are short-living phagocytes. These granulocytes are recruited from the blood stream to damaged or infected tissue by acute inflammation signals. Tumor-associated neutrophils (TANs) infiltration is correlated with lung cancer progression, with no markedly difference between the cancer subtypes [61]. At the beginning of tumor growth, neutrophils promote inflammation releasing cytokines and reactive oxygen species (ROS), which initially promote cancer cells apoptosis. Later on, TANs can play a pro-tumor role in metastasis by retaining circulating cancer cells and so helping the formation of secondary tumors [62]. In a NSCLC mouse model, Mollaoglu and colleagues observed that the expression of SOX2 in Kras-driven adenocarcinomas induced the production of CXCL5 and subsequently the recruitment of tumor-associated neutrophils [63]. Gentles and colleagues identified the abundance of neutrophils in the TIME as a predictor of poor outcome in multiple cancers, including NSCLC [64]. Accordingly, a high neutrophils/lymphocytes ratio is as well associated to poor prognosis in NSCLC and other tumors [65].

Macrophages are part of TIME. Macrophages are IFN-γ stimulated granulocytes that can be distinguished in M1, typically activated in inflamed contexts, and immune-suppressive M2, which contribute to wound healing. M1 macrophages can phagocyte or kill cancer cells by releasing the content of their granules, namely lysosomal enzymes, ROS and NO (nitric oxide). Oppositely, M2 macrophages facilitate tumor progression and angiogenesis through the release of VEGF and TGF-β. The presence of IL-4 in the TME favors the differentiation of

macrophages in the M2 subtype [66]. Similarly to TANs, also a high density of tumor-associated macrophages (TAMs) was associated to poor prognosis in lung cancer [67].

Myeloid-derived suppressor cells (MDSCs) originate from neutrophils and macrophages; MDSCs are absent in physiologic conditions and generated in chronic pathologic conditions, such as tumors. In KRAS mutant lung cancer it was observed that chronic inflammation contributes to MDSCs accumulation, as their number can be reversely reduced by IL-6 blockade [68]. These cells, along with regulatory T cells contribute to the formation of an immunosuppressive microenvironment; the release of a set of chemokines, including CCL5, CCL17, CCL22, CXCL8, and CXCL12, contribute to recruit MDSCs and Tregs in the TME, thus boosting an immunosuppressive TME [69].

## Tumor immunology

The interplay between cancer and the TME is very complex. In this chapter, I will describe some interactions occurring between the immune system and tumor cells. First, I will illustrate how the immune system may play a dual role during tumor growth, summarized in the immunoediting theory. Here, the immune system has an anti-tumorigenic function through the elimination of emerging cancer cells, thereby selecting immune-evasive cancer cells.

Then, after defining the characteristics of activated and functional effector cells, I will outline some dysfunctional states of T cells that are observed in chronic infections and cancer. Encouraging results, obtained in the past years with ICI treatments, prove that effector functions can be restored in T cells. The identification of the mechanisms that underlie the dynamics of T cell dysfunction could guide towards more effective ICI strategies and also identify predictive biomarkers.

The shift from effector T cells towards terminally exhausted lymphocytes may be triggered by chronic TCR stimulation in cancer, but this is not the only mechanism that could impair T cell activity. In the last section of this chapter I will describe some evasion strategies of cancer cells and how they can down-modulate the tumor immune microenvironment (TIME).

### 1.2.1 Immunosurveillance and immunoediting

Immunosurveillance, first hypothesized by Paul Ehrlich at the beginning of the XX century, is the concept for which the immune system constantly impedes the development of tumors, that otherwise would appear throughout the life of an individual. This theory could only be demonstrated by the end of the century and, thanks to milestone findings in the immunology field, e.g. the discovery of tumor neo-antigens, was included in a more complex concept called immunoediting. This newer notion described by Schrieber [70] brings to light the dual role of the immune system, which in first instance eliminates tumor cells, but doing so shapes the tumor and inevitably selects tumor variants either with reduced immunogenicity or that have acquired evasive or immunosuppressive abilities. This process may be described through 3 sequential phases: elimination, equilibrium, and escape.

Elimination is the reinterpretation of the immunosurveillance concept. It is now clear that innate and adaptive immunity actively protect from tumor formation. Studies conducted on IFN-γ or perforin-deficient mouse models showed that they are essential to control tumor growth induced by chemical carcinogens. Moreover, the presence of infiltrating $CD8^+$ T lymphocytes correlate with a favorable prognosis in patients with different types of cancer [71]. Additionally, several reports indicate that individuals with severe immune deficits, for example people taking immunosuppressive agents after a transplant or patients with acquired immunodeficiency syndrome, have indeed a higher probability to develop a variety of cancers with no known viral etiology. During the elimination phase, the innate immune cells (NK cells, macrophages, dendritic cells, γδ T cells) are recruited in the tumor area thanks to the inflammatory cytokines released as consequence of the local tissue damage caused by the tumor growth [72]. Then, dendritic cells ingest tumor cells debris formed after tumor killing and migrate to the draining lymph nodes. Here, naïve T cells will be exposed with the tumor antigen; the concomitant inflamed environment will promote the activation and expansion of tumor-specific $CD8^+$ and $CD4^+$ Th1 cells. These T cell clones will migrate back to the tumor site and promote the clearance of the specific antigen-bearing cancer cells.

Equilibrium is the phase in which tumor growth is dynamically counterbalanced by immune clearance. In this process, the lymphocytes exert a potent Darwinian selection on the cancer cells, as brought to evidence by a number of studies. In fact, it was observed that the repassage of transplantable tumors through immunocompetent mice generated tumor variants with reduced immunogenicity. In contrast, tumors originated in immunodeficient mice were rejected when transplanted into immunocompetent hosts, suggesting that without the immune system there is a lack of selective pressure in favor of poorly immunogenic cancer cells [73]. These results show that the immunologic context in which tumors grow sculpts the cancer cells; the apparition of immune-escaping alterations in cancer cells and the induction of an immunosuppressive microenvironment is undoubtedly facilitated by their genomic instability. It is likely that the editing of the tumor by the immune system is a continuous process, happening probably for a long time before the tumor could be clinically detectable.

Eventually, in the escape process, tumor variants that have survived thanks to the poor immunogenicity or the gain of an immunosuppressive phenotype will begin to expand uncontrollably. This unrestrained tumor growth then leads to the development of clinically detectable malignancies.

### 1.2.2 From T lymphocyte activation to T cells exhaustion and dysfunction

T cell priming occurs in secondary lymphoid organs, when a naïve T cell recognize a specific epitope presented by APCs. The priming of a naïve T cell is induced by the synergy of 3 signals: the first is the MHC-restricted recognition of the antigen by the TCR, the second is the "co-stimulus", or else the interaction of the CD28 with its ligand (CD80 or CD86) on APCs and the third is the presence of pro-inflammatory cytokines. A successful activation of the T cells induces the exit from the quiescence state, with metabolic and transcriptomic reprogramming that fuels the initiation of clonal expansion, survival and differentiation in effector cells and memory. An inappropriate activation, due to the lack of the second and third stimulus would induce anergy, an inactive state unresponsive to further stimuli.

The priming induces radical changes in the T cell, the hallmarks of T cell activation include: cell cycle entry, cell growth, nutrient uptake, autocrine or paracrine IL-2 signaling, increase of anabolic metabolism and reprogramming of mitochondrial metabolism [74]. The shift from $G_0$ to $G_1$-S-$G_2$ is coordinated by cyclin-dependent kinases (CDKs) and cyclines. The rapid cell duplication (every 6hrs *in vitro*) and the cell growth, thanks to which cells double their size, need a dramatic increase of lipids and cholesterol production. Moreover, the upregulation of glucose transporter GLUT1 provide an increased uptake of glucose. IL-2 is a pivotal growth factor for T cells survival and proliferation. The IL-2 receptor is composed of 3 chains, namely α (CD25), β (CD122) and common γ ($\gamma_c$, CD132), of which β and γ chains are constitutively expressed to form an IL-2R complex with intermediate affinity. The concomitant stimulation of TCR and CD28 promote the transcription of IL2 and IL2RA (coding for CD25) genes through NF-κB, NFAT and AP-1 transcription factors. This autocrine and paracrine loop is fueled by STAT5 who, phosphorylated in proximity of the cytoplasmic tail of IL-2Rβ, translocate to the nucleus to further induce IL2RA transcription [75].

Another molecule early expressed (~1h) after TCR engagement is CD69 [76]. CD69 is a transmembrane type II C-lectin receptor rapidly expressed upon T lymphocytes activation through the activity of NF-κB and AP-1 transcription factors. CD69 interacts with soluble galectin 1 (gal-1) and with the sphingosine 1-phosphate receptor 1 (S1P1) [76]. S1P1 interacts with the sphingosine-1 phosphate (S1P), a lipid mediator present in the bloodstream and less abundant in the tissues' interstitial fluid. The in cis interaction between CD69 and S1P1 impedes the interaction of the latter with S1P and results in tissue retention [77]. Thus, CD69 is a typical marker of tissue resident memory cells ($T_{RM}$), along with CD103 (integrin protein, binding integrin β7 in epitelia).

After the clonal amplification of the specific T cell clones and differentiation in effector and memory cells, T cells migrate to tissues through the blood stream guided by chemokine gradients. Here T helper cells (Th) $CD4^+$ will sustain the cytotoxic T cells $CD8^+$ and macrophages through the release of IFN-γ. After the resolution of the immune response, memory T cells will undergo a quiescent state and will promptly re-activate upon recognition of the specific antigen [78]. Once the threat is eliminated, in order to defuse the immune response, T cells upregulate inhibitory immune checkpoints, which will contribute to decrease of effector functions and contribute to reach an exhausted and unresponsive state.

T cells exhaustion is a differentiation state induced by a chronic stimulation of the TCR, first observed in T cell responses to chronic viral infections. It describes a distinct transcriptional, metabolic and epigenetic state to which T lymphocytes undergo in order to regulate chronic responses and avoid autoimmune pathologies. The exhaustion state is often described as a hypo functional (or dysfunctional) state in which T cells show reduced effector functions, loss of proliferation, reduced cytokine production, high expression of inhibitory immune checkpoints [79] and alterations in the transcription factor programming (TOX, TCF1, NFAT, IRF4, BLIMP1) [80]. Nonetheless, the expression of inhibitory checkpoint receptors is not a unique feature of T cell exhaustion since functional effector T cells can express as well these markers. Thus, an exhausted phenotype expressing inhibitory immune checkpoints does not axiomatically overlap with a dysfunctional state. Singer and colleagues observed that transcriptional

signatures for dysfunctional and activated $CD8^+$ T cells are intertwined. Using a metallothionein (cysteine-rich protein regulating metal homeostasis and protecting from heavy metal toxicity, DNA damage, and oxidative stress) deficient mouse model they uncoupled the correlation between PD1 and TIM-3 expression with reduced effector functions on T cells, inversely observed in WT mice. Moreover, they described a subpopulation of $TIM\text{-}3^+$ TILs expressing the transcription factor GATA3 and showing a dysfunctional state, with reduced IFN-γ and IL-2 production upon stimulation [81].

Up to date, it is still unknown how a T lymphocyte becomes a terminally differentiated exhausted T cell and whether this status could be reversible. As exhaustion seem to be a multistep differentiation process, exhausted CD8+ TIL are a heterogeneous population. Thus, it is unclear if ICI elicit tumor control thanks to the ensemble of $CD8^+$ TIL heterogeneous exhausted populations or if it acts preferentially on some subpopulations [82].

Studies conducted on chronic viral infections identified a cell population with memory-like properties that could represent the progenitor exhausted T cell in conditions of chronic antigen stimulation ($TCF1^+$ $PD\text{-}1^+$), thanks to their self-renewal characteristics [83].

As illustrated Figure 5 this recently described population, defined as "progenitor exhausted cells", can differentiate in both effector CTLs and $TCF1^-$ fully differentiated exhausted cells [84]. Figure from [85]. Miller and colleagues identified in advanced melanoma patients a correlation between a higher fraction of progenitor exhausted CD8+ TILs population (TCF1+ PD-1+ CD8+ SOX10- cells) and longer duration of responses to immunotherapies (nivolumab+ipilimumab) [82].

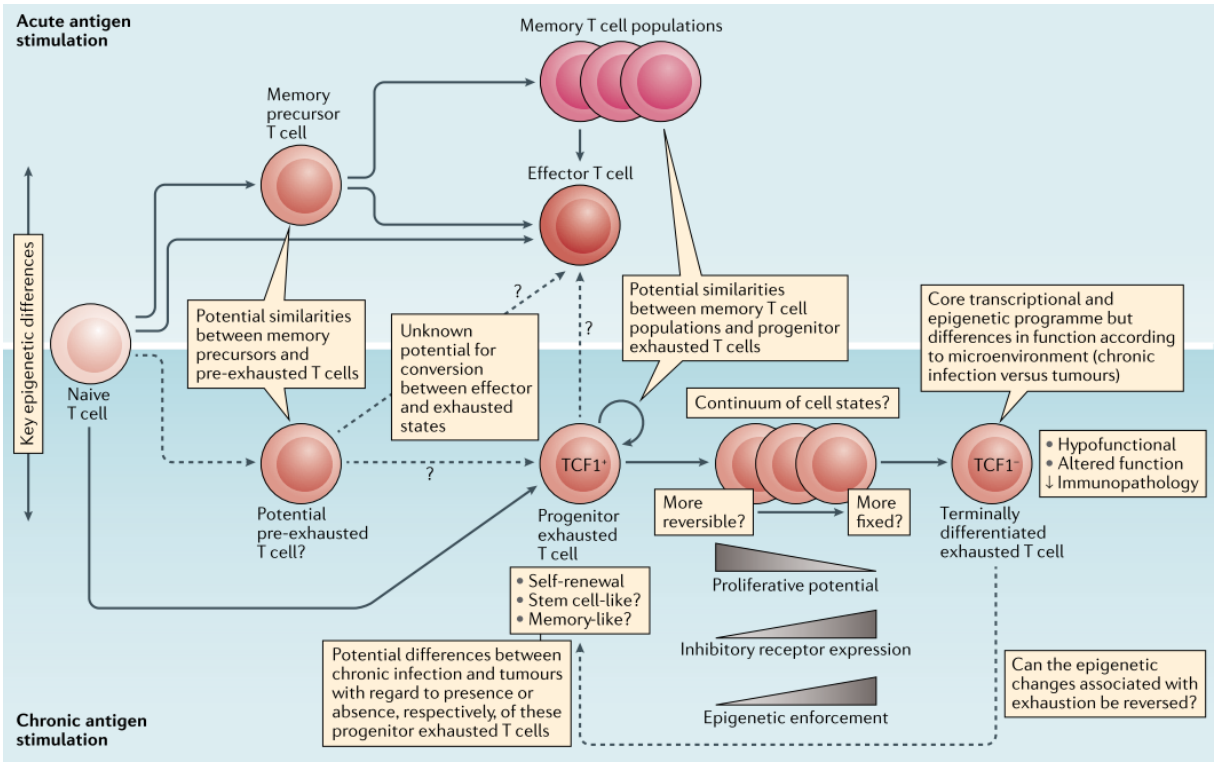


*Figure 5 : T cell exhaustion.*

*Potential differentiation statuses and features of functional effector T cells and memory T cells in acute antigen stimulation compared to exhausted phenotypes in chronic antigen stimulations.*

Furthermore, studies on the epigenetic state of exhausted T cells revealed a unique chromatin landscape influencing the transcriptional state and limit effector functions. Interestingly, specific chromatin states determined if exhausted T cell status could be reversed after therapy, avoiding a terminal non responsive exhaustion [86].

A better understanding of the T cell exhaustion process and its relationship with immune checkpoints will allow, while targeting subpopulations of exhausted T cells, to uncover the potential and the limitations of ICI treatments. Moreover, unraveling epigenetic and functional changes in dysfunctional exhausted cells could lead to the development of therapeutic strategies that could revert dysfunctional states and re-sensitize T cells to immune checkpoint blockade.

### 1.2.3 Immune checkpoints

Immune checkpoints are a set of receptors expressed by immune cells, which tightly regulate the immune response. Their function is either to increase the effector functions or to contain

excessive or sustained immune activation that could lead to tissue damage and autoimmune reactions [87] [88]. Accordingly, patients presenting autoimmunity due to common variable immunodeficiency disorders, were harboring heterozygous mutations in the regulatory immune checkpoint CTLA-4 [89].

Immune checkpoints can be distinguished in co-stimulatory receptors, which are induced by the engagement of the TCR against foreign epitopes, and co-inhibitory receptors who instead dampen the immune response. The engagement of inhibitory immune receptors by cancer cells to escape anti-tumor immunity is a hallmark of cancer. The discovery of PD-1 and CTLA-4 inhibitory immune checkpoints and the idea to block their function with antagonist antibodies were worth, in 2018, a Nobel Prize in medicine to Tasuku Honjo and James Allison [90]. The revolutionary approach to "unleash the breaks of the immune system" brought attention to other targetable inhibitory checkpoints and to the development of new antibodies, including agonist antibodies targeting co-stimulatory immune receptors.

Initially identified in NK cells, inhibitory receptors were shown to contain ITIM (Immunoreceptor Tyrosine-based Inhibition Motif), inhibitory domains that would block the activatory signal coming from ITAM domains (Immunoreceptor Tyrosine-based Activation Motif) present on the cytoplasmic tail of activatory receptors [91]. The inhibitory activity of these classical inhibitory receptors is classically perpetrated by the recruitment of the phosphatases SHP1 and SHP2 (containing SH2 -Src homology region 2) which de-phosphorylate the molecules downstream activatory receptors, such as the TCR ζ chain and ZAP-70 [92]. Nevertheless, it was later observed that other inhibitory immune checkpoints, such as LAG-3, TIM-3 and CTLA-4, did not have any ITIM domain or did not act through ITIM domains. Nowadays these receptors are rather defined by their function.

#### 1.2.3.i PD-1

PD-1 (CD279) is an inhibitory receptor, which plays a pivotal role in the containment of the adaptive response and maintenance of peripheral tolerance. Its expression is induced by activatory signals originated by the TCR engagement and cytokine receptors [93], via NFAT transcription factor but also by Notch and IRF9. Oppositely, T-bet was shown to repress PD-

1 expression in chronic infections [94]. This transmembrane protein, belonging to the CD28 family, consists of an extracellular domain, containing an IgV-like domain, a transmembrane domain and an intracellular tail, containing ITIM and ITSM domains (Immunoreceptor Tyrosine-based Switch Motif). In the N-terminal of its cytoplasmic tail, PD-1 contains an ITIM domain, known to recruit SH2-containing phosphatases [95], and in its C-terminal domain an ITSM domain. Studies conducted with mass spectrometry [96] and a chimeric construct CD28 (murine)-PD-1(human) [97] reported that in PD-1 the ITSM domain contains (at the Y248) the docking site for SHP2 and SHP1. Those phosphatases attenuate the phosphorylation of ZAP-70 (mediated by Lck) downstream the TCR, reducing the activatory signals coming from TCR engagement [98]. Moreover, the recruitment of SHP-2 by PD-1 blocks the activation of PI3K-Akt as well as Ras, affecting cell survival and proliferation. Another inhibitory effect of PD-1 is the upregulation of BATF transcription factor, a negative regulator of AP-1 (involved in T cell activation and proliferation). PD-1 signaling negatively affects T cells metabolism, decreasing glucose and amino acids uptake and metabolism; in addition to that, PD-1 impairs the glycolysis and glutaminolysis necessary to activated T cells and promotes fatty acids β-oxydation [99]. Interestingly, the effects of PD-1 inhibitory signals is related to the intensity of PD-1 signal transduction pathway, where the more PD-1 is expressed and bound, the more T cell activity is inhibited (from inhibition of TNF-α and IL-2 to T cell proliferation and survival) [100]. PD-1 ligands include PD-L1 (CD274) and PD-L2 (CD273), which are expressed by a wide number of cell types. Constitutively expressed by APCs at low levels, PD-L1, can be found on vascular endothelial cells and in immune privileged organs (placenta, testis, eye) and in cancer. Interferons, VEGF and tumor necrosis factor α (TNF- α) can induce PD-L1 and PD-L2 expression on fibroblasts, macrophages, MDSCs and endothelial cells in the TME. Butte and colleagues showed that PD-L1 can alternatively inhibit T cells interacting with the co-stimulatory molecule B7-1 (CD80 ligand of CD28) on T cells [101].

#### 1.2.3.ii CTLA-4

Cytotoxic T-lymphocyte antigen 4 (CTLA-4, CD152) is a transmembrane receptor of the IgG superfamily, that contributes to the regulation of immune homeostasis. Temporarily expressed on T cells after TCR and CD28 engagement, CTLA-4 is constitutively expressed by

$T_{reg}$ cells and contributes to their regulatory functions. CTLA-4 shares its ligands, B7-1 (CD80) and B7-2 (CD86), with CD28 except that binding affinity of the first is much higher. Thus, the first cell-extrinsic inhibition mechanism of CTLA-4 is the competition for the "co-stimulatory signal" (B7-1/2) on APCs; a second extrinsic mechanism of action is the trans-endocytosis of CTLA-4 ligands, depleting them from the APCs [102]. An intrinsic mechanism of immune modulation of CTLA-4- is represented by the interaction in its cytoplasmic tail with SHP2 and PP2A phosphatases [103]. Due to its constant clathrin-mediated endocytosis, the majority of CTLA-4 (about 80%) results stored in the cytoplasm. Then, CTLA-4 can be rapidly shuttled from the trans Golgi to the plasma membrane by a molecular complex composed of TRIM, LAX and Rab8 [104]. CTLA-4 was, along with PD-1, the first inhibitory receptor to be targeted in clinics with antagonistic antibodies and ipilimumab (anti-CTLA-4) was the first ICI approved in clinics.

### 1.2.3.iii LAG-3

LAG-3 (lymphocyte activation gene-3, CD223) is a co-inhibitory receptor expressed by T cells after their stimulation in order contain activation. LAG-3 can also be expressed by activated B cells, NK cells and plasmacytoid DCs [105] [106]. This transmembrane protein is a homolog of CD4 and binds as well the major histocompatibility complex II (MHC-II).The extracellular portion of LAG-3 is composed of four immunoglobulin superfamily-like domains (D1-D4). Moreover, an additional proline rich loop on the D1 domain confers the ability of binding to the MHC-II with higher affinity than CD4 [107] [108]; the competition with CD4 for the MHC-II binding contributes to the inhibitory activity of LAG-3. However, its mode of action, especially intracellular, has not been fully clarified yet. In its cytoplasmic portion, LAG-3 does not present any domain devoted to the recruitment of phosphatases. Instead, it contains a highly conserved KIEELE motif and an EP motif (repeated glutamic acid and proline motif). Workman and colleagues showed that the negative regulatory function of LAG-3 requires the KIEELE motif present in the cytoplasmic tail and that is CD4-dependent [109]. Besides, the downstream effects of the binding of LAP protein (LAG-3-associated protein) to the EP domain are still unclear [110].

Additional ligands of LAG-3 are galectin-3, LSECtin (liver sinusoidal endothelial cell lectin) and FGL-1 (fibrinogen-related protein 1). Whether galectin-3 is a lectin expressed on tumor stromal cells, LSECtin is a lectin expressed by tumor cells. The blockade of the interaction of LAG-3 with both galectin-3 and LSECtin increases IFN-γ production by T cells $CD8^+$ [111], [112]. FGL-1 is a newly identified functional ligand of LAG-3 [113]. This liver-secreted protein binds the D1 and D2 domains of LAG-3 with high affinity, independently from MHC-II. Normally secreted at low levels by the liver,FGL-1 can be highly expressed in solid tumors, including lung cancer, prostate cancer, melanoma and colorectal cancer. MC38 colon cancer cells inoculated in FGL-1 KO mice grew significantly slower than in WT mice. In conclusion, LAG-3-FGL-1 interaction could inspire new therapeutic strategies in cancer treatment.

The aberrant expression of MHC-II in tumors, induced also by the exposure to IFN-γ in the TME, was shown to dampen the cytolytic activity of $CD8^+$ T cells in melanoma through the engagement of LAG-3 [114]. Encouraging results in mice suggest that anti-LAG-3 antibodies elicit anti-tumor responses in combination with anti-PD-1 antibodies [115].

#### 1.2.3.iv TIM-3

T cell immunoglobulin and mucin-domain containing protein- 3 (TIM-3, CD366, HAVCR2) is a type 1 cell surface glycoprotein. Member of the TIM family, including TIM-1 and TIM-4, TIM-3 contains in the extracellular portion a conserved IgV domain with N-linked glycosylation sites and a mucin domain. The cytoplasmic tail contains five conserved tyrosines and can be phosphorylated and participate to its inhibitory function.

Discovered in 2002 on the surface of $CD4^+$ T helper 1 (Th1) and cytotoxic T cells $CD8^+$ [116], TIM-3 is also expressed by $T_{reg}$ cells, mature NK cells and by members of the innate immunity (DCs, macrophages, mast cells) [117]. TIM-3 is associated with an exhausted and dysfunctional phenotype of $CD8^+$ T cells in cancer [118] and linked to cancer progression in NSCLC [119].

The IgV domain of the extracellular portion of TIM-3 is the specific binding site for galectin-9 [120]. Other known ligands are Ceacam-1 (carcinoembryonic antigen–related cell- adhesion molecule 1) phosphatidylserine (PtdSer) and high-mobility group box 1 (HMGB-1). The

binding of galectin-9 induces apoptosis in Th1 cells, therefore contributing to the disruption of anti-tumor immunity [121]. More in detail, the binding of both Galectin-9 and Ceacam-1 to TIM-3 leads to the phosphorylation of two conserved tyrosines (Y256 and Y263) in the cytoplasmic domain, which detaches Bat-3 and allows the recruitment of Src kinases (containing SH2 domains) and consequent negative regulation of TCR signaling [122]. Other intracellular signaling proteins that interact with TIM-3 include PI3K, PLC-γ, ZAP-70 and Lck [123].

Huang and colleagues suggest that Ceacam-1, co-expressed on T cells, forms heterodimers with TIM-3 acting as a self-ligand and that this interaction is necessary for the induction of TIM-3 inhibitory functions (tolerance and exhaustion) [124]. Moreover, the co-expression of Ceacam-1 and TIM-3 on TILs was shown to be correlated with a lower release of IFN-γ by $CD8^+$ T cells in colorectal cancer [125]. The interaction of TIM-3 with PtdSer is 4-5 fold weaker compared to other members of the TIM family and its interaction drives the clearance of apoptotic bodies and cross-presentation of antigens by DCs [126]. However, the role on PtdSer-TIM-3 interaction on TILs is not clear yet. Lastly, HMGB1 is a damage-associated molecular pattern, which binds to the TIM-3 present on tumor-infiltrating DCs. This interaction suppresses innate immune response to nucleic acids, mediated by Toll-like receptors; Chiba and colleagues showed that DC-specific TIM-3 perturbs the antitumor efficacy of DNA [127].

New studies report that monoclonal antibodies blocking TIM-3 improves T cell anticancer responses either alone or in combination with anti-PD-1 [128].

#### 1.2.3.v TIGIT

TIGIT (T cell immunoreceptor with Ig and ITIM domains) is a co-inhibitory receptor expressed on the surface of immune cells. Initially characterized in NK cells, TIGIT is expressed on activated T cells, memory T cells, $T_{reg}$ and follicular T helper cells [129]. TIGIT presents an extracellular Ig variable domain, a transmembrane domain and a cytoplasmic tail. The cytoplasmic portion of TIGIT contains an ITIM motif and an Ig Tail-Tyrosine-like motif (ITT); the phosphorylation on Y231 in the ITIM motif or of Y225 in the ITT domain mediate the activation of the downstream pathway [130].

The engagement of TIGIT through the binding with its ligands, CD155 (PVR) or CD112 (PVRL2), causes the phosphorylation on ITIM and ITT domains and mediate an intrinsic inhibitory activity. The recruitment of SHP1 to the cytoplasmic tail of TIGIT blocks PI3K, MAPK and NF-κB pathways. Moreover, TIGIT induces the downmodulation of TCRα and CD3ε, essential components of the T cell receptor, as well as PLCγ, a component of the TCR pathway [131]. Essentially, TIGIT inhibitory functions hinder T cell activation, acquisition of effector functions and proliferation.

TIGIT shares its ligands with CD226 and CD96, an activatory receptor and an inhibitory receptor respectively, co-expressed by T cells at the surface. In vitro activation increases the expression of both CD226 and TIGIT, but TIGIT second was associated to a subset of exhausted PD-1+ CD8+ T cells in NSCLC [132].

Figure 6 illustrates the multiple interactions of LAG-3, TIM-3 and TIGIT co-inhibitory immune receptors. Figure from [133].

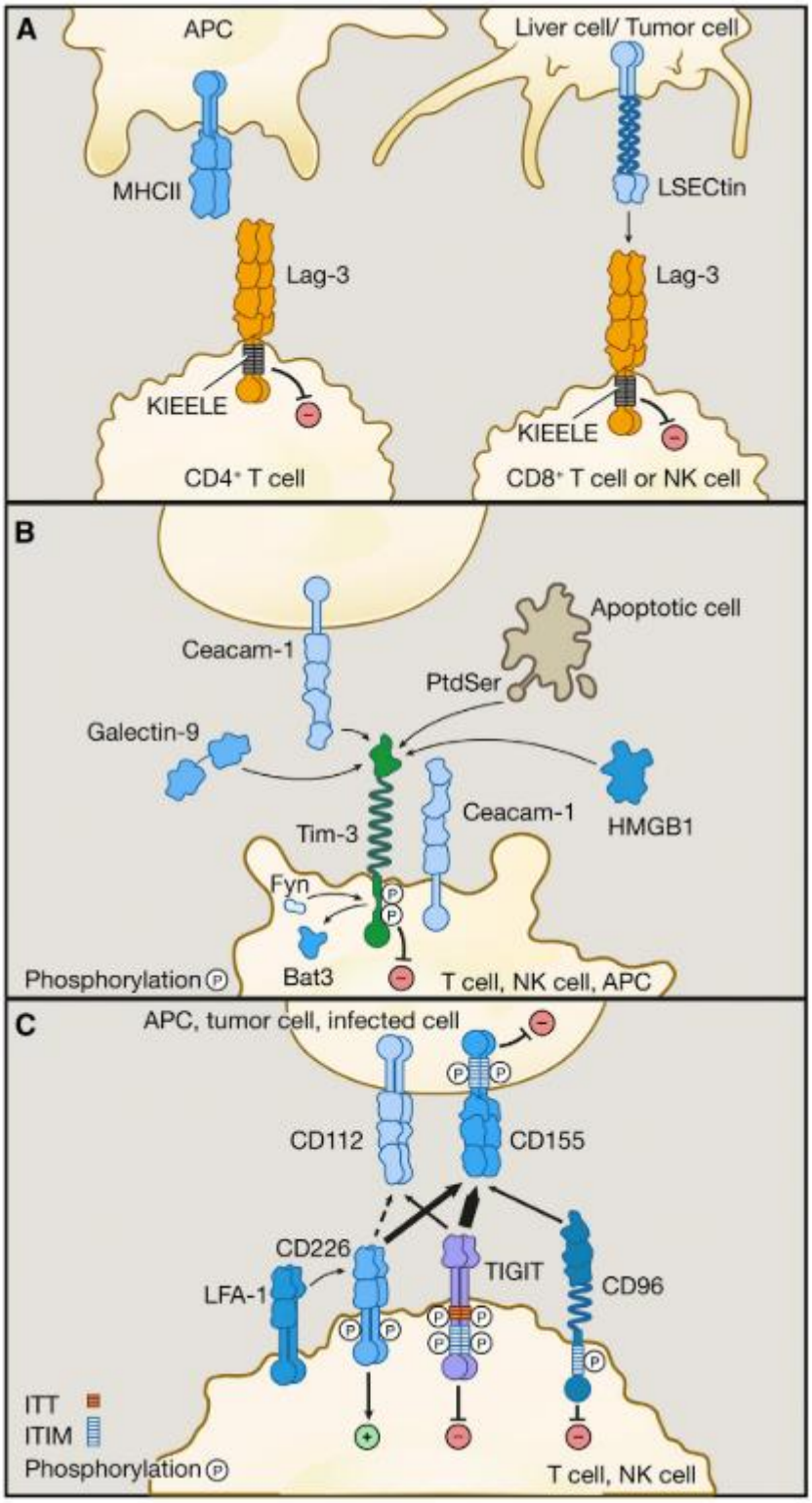
A
APC
Liver cell/ Tumor cell
MHCII
LSECtin
Lag-3
Lag-3
KIEELE
KIEELE
CD4+ T cell
CD8+ T cell or NK cell
B
Apoptotic cell
Ceacam-1
PtdSer
Galectin-9
Tim-3
Ceacam-1
HMGB1
Fyn
Phosphorylation
Bat3
T cell, NK cell, APC
C
APC, tumor cell, infected cell
CD112
CD155
CD226
LFA-1
TIGIT
CD96
ITT
ITIM
Phosphorylation
T cell, NK cell

*Figure 6 Inhibitory receptor pathways*

*A) LAG-3 pathway. Left: Lag-3, expressed on T cells and NK cells, either binds to MHC class II on antigen-presenting cells (left) or binds to L-SECtin on tumor cells (right). The KIEELE motif in the cytoplasmic tail of Lag-3 mediates the inhibitory function. B) TIM-3 pathway. TIM-3 is expressed on the surface of T cells, NK cells, and some APCs. TIM-3 ligands include galectin-9 and HMGB1 (soluble) and Ceacam-1 and PtdSer (cell surface ligands). The engagement of TIM-3 receptor causes the dissociation of Bat-3 Bat-3 from the cytoplasmic tail of Tim-3; this allows Fyn binding and the induction of inhibitory functions. C) TIGIT pathway. TIGIT is expressed on on T cells and NK cells and shares its ligands CD112 and CD155 with the CD226, and CD96 which are co-expressed at the T cell surface. CD155 and CD112 can be found on APCs and tumor cells. TIGIT, CD96, and CD155 deliver inhibitory signals through their ITIM motifs in their cytoplasmic tails. Contrarily, CD226 interacts with the integrin LFA-1 and delivers a positive signal.*

## Immunotherapies

Immunotherapies are a class of treatments able to activate or suppress some components of the immune system, in order to help the patient to overcome the disease. Immunotherapies find application in the treatment of various diseases, from autoimmune diseases to infectious diseases to a set of malignancies.

The immunotherapies used in anticancer treatment can be defined as active or passive, depending on the mode of action. For instance, adoptive cell transfer (for instance the adoption of T cells with modified TCR, CAR-T cells), monoclonal antibodies (mAbs) targeting tumor cells and oncolytic viruses have intrinsic antitumor activity, therefore are defined passive. Inversely, active immunotherapies engage the immune system of the host against the cancer. Active immunotherapies include DC-based immunotherapies, peptide and DNA-based anticancer vaccines, immunomodulatory mAbs, immunostimulatory cytokines, inhibitors of immunosuppressive metabolism, PRR (pattern recognition receptors, necessary for the activation of the innate immune system) agonists and immunogenic cell death (type of cell death able to elicit an immune response, differently from apoptosis) inducers [134].

For the purpose of my project, I will only focus on the immune checkpoint inhibitors.

### 1.3.1 Immune checkpoint inhibitors

In lung cancer treatment, monoclonal antibodies (mAbs) targeting immune checkpoints have proven in the past decade to induce effective and durable responses [135].

The first ICI approved for clinical use was ipilmumab, a mAb anti-CTLA-4 produced by Bristol-Myers Squibb, in metastatic melanoma. It was later observed that mAbs targeting PD-1, such as nivolumab or pembrolizumab, attended a better objective response with the advantage of less immune-related adverse events (irAEs) [136]. In fact, severe irAEs occur in 15-30% of patients receiving anti-CTLA-4 ICI and ~33% in NSCLC patients treated with a combination of nivolumab plus ipilimumab. It is possible that the anti-PD-1 ICIs act more specifically in the context of the TME, therefore are associated with less irAEs. Anyhow, it is still unknown why patients differentially develop irAEs. Immune-related adverse events include a variety of diseases mediated by inflammation or autoimmune responses due to the important contribution of immune checkpoint in the maintenance of immunologic homeostasis. IrAEs could appear as dermatologic rashes, vasculitis, myocarditis, entero-colitis, arthritis, encephalitis, uveitis and anemia [137]. Intriguingly, it was found a positive correlation between the development of irAEs and the overall survival of patients in NSCLC patients treated with nivolumab [138].

An increasing number of immune receptors can now be targeted and several clinical trials are now assessing the efficacy of these novel treatments. Moreover, in order to overcome resistance to the treatment with ICI, the combination of multiple ICIs is now under investigation in a number of clinical trials. Table 2 resumes monoclonal antibodies blocking inhibitory immune receptors and agonist antibodies targeting co-stimulatory immune receptors approved by the European Medicines Agency (EMA) or currently tested in clinical trials for lung cancer treatment [139] [31], [140], [141].

*Table 2 Relevant immune checkpoint inhibitors*

| Target | Drug (commercial use name) | Manufacturer | Description | Status | Therapeutic combination |
|---|---|---|---|---|---|
| PD-1 | Nivolumab (opdivo) | Bristol-Myers Squibb | mAb to human PD-1 (IgG4) | First-line treatment of non mutated NSCLC | Ipiimumab/ platinum based chemotherapy |
| PD-1 | Pembrolizumab (keytruda) | Merck | mAb to human PD-1 (IgG4) | First-line treatment metastatic NSCLC | Ipiimumab/ platinum based chemotherapy |
| PD-L1 | Atezolizumab (tecentriq) | Roche | mAb to human PD-L1 (IgG1) | First-line treatment metastatic NSCLC | Bevacizumab, taxol and carboplatin |
| CTLA-4 | Ipilimumab (yervoy) | Bristol-Myers Squibb | mAb to human CTLA-4 (human IgG1) | First-line treatment of non mutated NSCLC | Nivolumab |
| LAG-3 | Relatlimab (BMS-986016) | Bristol-Myers Squibb | mAb to human LAG-3 (IgG4) | Phase II: NSCLC. | Nivolumab |
| TIM-3 | BMS-986258 | Bristol-Myers Squibb | mAb to human TIM-3 | Phase I–II: advanced malignant tumors. | Nivolumab |
| TIM-3 | RO7121661 | Roche | Bispecific anti-TIM-3–anti-PD-1 | Phase I: NSCLC. | Monotherapeutic arm only |
| TIGIT | Tiragolumab (MTIG7192A) | Genentech | mAb to human TIGIT (IgG1) | Phase II: NSCLC. | Atezolizumab |
| OX-40 | BMS-986178 | Bristol-Myers Squibb | Agonist mAb to human OX-40 (IgG1) | Phase I/II: intratumoral injection in solid tumors. | SD-101 (TLR9 agonist) |
| CD137 (4-1BB) | Utomilumab (PF-05082566) | Pfizer | Agonist mAb to human CD137 (IgG2) | Phase I: advanced solid tumors | Pembrolizumab |
| GITR | BMS-986156 | Bristol-Myers Squibb | Agonist mAb to human GITR | Phase I/II: metastatic NSCLC | Nivolumab/ Ipilimumab |

### 1.3.2 Predictive factors of the response to ICI

The exploration of biomarkers in the TME for prognosis, diagnosis or predictability of the response to treatments is an area of active research. Particularly in the use of ICI, where only a small percentage (20-30%) of patients effectively respond [142], finding patterns associated to the response would help to unravel their mechanisms of action within the complexity of the TME.

Up to date, a univocal biomarker to predict the efficacy of ICI treatments has not been identified yet. Clinical trials in NSCLC testing PD-1 or PD-L1 inhibitors used the level of expression of PD-L1 on cancer cells (using different cut-offs, from PD-L1≥1% to PD-L1≥50%) as a predictive biomarker [143] [144]. These studies revealed a partial predictability of PD-L1 as biomarker, since many patients PD-L1$^{+}$ did not respond to treatments and yet in some PD-L1$^{-}$ there was a response to treatment. The lack of reliability on PD-L1 expression as biomarker could be partly accounted on a lack of standardization in its detection and interpretation. In fact, PD-L1 expression is very heterogeneous within NSCLC tumors, with 90% of heterogeneity appears within the same tissue slide, while positively the variance between different regions of the tumor is not substantial [145]. Moreover, institutions the use of different antibodies (their intensity impacts on the evaluation of the immunohistochemistry scores assigned by the pathologists) and choose different cut-offs [146] [147]. Anyway, the lack of better markers makes the expression of PD-L1 in the tumor the cut-off baseline for the administration of anti-PD-1 drugs in first line treatments [31].

The tumor mutational burden (TMB) is a second possible biomarker evaluated for ICI responses. Govindan and colleagues observed that in the NSCLC genomic landscape of smokers, the average mutation frequency was more than 10-fold higher than in never smokers [148] . Next, Ritzvi and colleagues associated in NSCLC treated with pembrolizumab (anti-PD-1) high nonsynonymous mutation rates with better objective responses, progression-free survival and durable clinical benefit [149]. This correlation was observed in in other studies on NSCLC using different ICIs, particularly in response of nivolumab (anti-PD-1) in combination with ipilumumab (anti-CTLA-4) [150]. However, the lack of standardization in the

determination of TMB and the difficulty to assess its levels, prevented the development of routine tests based on TMB so far.

Other studies focused on the characterization of the immune composition to find predictive signatures or cell populations that imply a response to ICIs.The presence of T lymphocytes was first observed to be correlated with good prognosis in NSCLC; more precisely, the Th1 and memory $CD8^+$ T cells were linked to the absence of methastatic invasion [151]. Moreover, it was found that the presence of $T_{RM}$ $CD103^+$ cells in lung cancer is positively associated to a response to ICI [152]. Interestingly, in fresh biopsies of melanoma, Ribas and colleagues observed that in patients responding to treatment with anti-PD-1, CD8+ effector memory subsets were the most amplified [153]. Taken together, these findings highlight the importance of memory T cells, which could be accountable for the durability of ICI responses.

As previously decribed, the presence of tertiary lymphoid structures (TLS) is associated with good prognosis in NSCLC patients. Interestingly, in melanoma and in sarcoma TLS were positively correlated to a response to immune checkpoint blockade [154] [155]. Ongoing researches, reported in the 2020 AACR annual meeting, are studying if TLS and the secretion of CXCL13 (B lymphocytes chemoattractant) could be a predictive factor for ICI responses.

In the recent years the gut microbiome was surprisingly found involved in the response to immune checkpoint blockade. In NSCLC patients who were treated with antibiotics prior receiving anti-PD-1/PD-L1 was observed that progression-free survival (PFS) and overall survival (OS) were significantly shorter [156]. Following studies in mice and humans helped to identify which gut microbiome strains are associated to the response or resistance to ICI. This surprising link between microbiome and ICI responses is opening new therapeutic avenues. For example, Dr Gal Markel is performing in the Ella Lemelbaum Institute of Immuno-Oncology (in Israel) a phase I single-center study of fecal microbiota transplant (FMT) in melanoma patients who failed at least one line of PD-1 blockade [157].

More studies are now trying to define which mechanisms could favor the response to immune checkpoint blockade by the microbiome [158].

### 1.3.3 Resistance to ICI

Despite the encouraging results obtained with immunotherapies in cancer treatment, the occurrence of resistance challenges the field to study the mechanisms eliciting resistance and find new combinations of therapies to overcome it. Resistance can be defined by the time of manifestation: primary resistance occurs in patients never-responders to treatment, adaptive immune resistance implies the adaptation and evasion of cancer cells from the immune response, and the acquired immune resistace emerges after a first time of response. Resistance to immunotherapies can be driven by tumor cell-intrinsic or extrinsic mechanisms. Intrinsic resistance occurs when cancer cells interfere with some pathways related to immune recognition and function. Contrarily, extrinsic resistance is due to the tampering of the immune response in the TME induced by other cell types and not by cancer cells.

#### 1.3.3.i Tumor-intrinsic resistance

Intrinsic mechanisms of primary and adaptive resistance include poor immunogenicity (low mutational burden or lack of antigenic mutations), impairment in the presentation of tumor antigens and the constitutive expression of PD-L1 [159].

In NSCLC, Rizvi and colleagues showed that the neoantigen load is correlated to a response to anti-PD-1 treatment [149] [160]. Accordingly, poorly immunogenic tumors, such as pancreatic and prostate, are less responsive to immunotherapy treatments [161]. An ineffective antigen presentation is an evading strategy to resist immune surveillance. Tumor cells can diminish the presentation at the surface of self antigens to escape the immune cytolytic activity [162] by downregulating the MHC-I [163], TAP (Transporter associated with Antigen Processing) or through the selection of cells harboring mutations in HLA-A, -B and -C genes or in beta-2-microglobulin (B2M). Indeed, β2-microglobulin loss-of-function disrupts MHC-I folding and transport at the plasma membrane [164].

IFN-γ is a pro-inflammatory cytokine that stimulates immune responses via the JAK/STAT pathway in immune cells and contributes to an efficient antigen presentation through the

upregulation of the expression of MHC-I in cancer cells. However, Garcia-Diaz and colleagues observed a double-faced role of IFN-γ in melanoma, where it contributes to adaptive resistance through the upregulation of the expression of PD-L1 on cancer cells [165].

### 1.3.3.ii Tumor-extrinsic resistance

Extrinsic resistance can be caused by T cells absence (like in immune desert tumors), the lack of tumor antigen-specific T effector cells, the impairment of T cells activation, the upregulation of several immune checkpoint on T cells and the action of immunosuppressive cells ($T_{reg}$ cells, immunosuppressive phagocytes, CAFs, endothelial cells) [166]. Extrinsic mechanisms of resistance include,

Immune desert tumors are indeed unable to mount an antitumor response, due to the inability of T cells to reach the tumor bed. Alternatively, T cells that are present but not recognize the tumor neoantigens would not respond to ICI. In melanoma it has been reported that the recruitment of suppressed dendritic cells (DCs) impairs the priming of naïve T cells causing a lack of TILs in the TME and unresponsiveness to ICI [167].

A further cause of extrinsic adaptive resistance is the expression of alternative immune checkpoints in T cells, which would compensate the PD-1 or CTLA-4 inhibition. Thommen and colleagues observed in TILs of patients with NSCLC the co-expression of several immune checkpoints, namely PD-1, CTLA-4, TIM-3, LAG-3, and BTLA; interestingly, they found that PD-1 and TIM-3 expression increases with the tumor stage [168]. Moreover, in patients with lung adenocarcinoma, Koyama and colleagues observed an increased expression of TIM-$3^+$ in both $CD8^+$ and $CD4^+$cells in patients resistant to previous anti-PD-1 treatment. Studies conducted on other cancer types, the first one in a mouse model of ovarian cancer [169] and the second one in an *in vitro* treatment with anti-PD-1 of TILs from head and neck cancer [170], showed as well an increase of alternate immune checkpoints after PD-1 blockade as an adaptive mechanism of resistance [171].

Lastly, other cells within the TME can dampen the immune response. CAFs isolated from NSCLC patients were shown to express PD-L1 and PD-L2 coregulatory molecules [41]. PD-L1 can also be expressed on blood endothelial cells (BEC), when stimulated by inflammatory

signals. Moreover, the release of immunosuppressive cytokines and metabolites participate in immunosuppression.

Figure 7 illustrates various stromal cells-released factors able to inhibit T cells, thus representing an additional putative cause of extrinsic resistance. Figure from [172].

The presence in the lung tumor microenvironment of IDO, NO, $PGE_2$ and IL-6 and IL-10 inhibit the cytotoxic activity of T cells. Moreover, TGF-β inhibits the differentiation of $CD4^+$ T cells in the IFN-γ releasing Th1 cells (correlated with good prognosis). IL-10 and $PGE_2$ may contribute to the impairment of T cells activation by impeding DCs maturation. Similarly, CAFs secrete pro-inflammatory cytokines and chemokines, including CXCL8, IL-4 and IL-6 which sustain suppressive M2 macrophages [172].

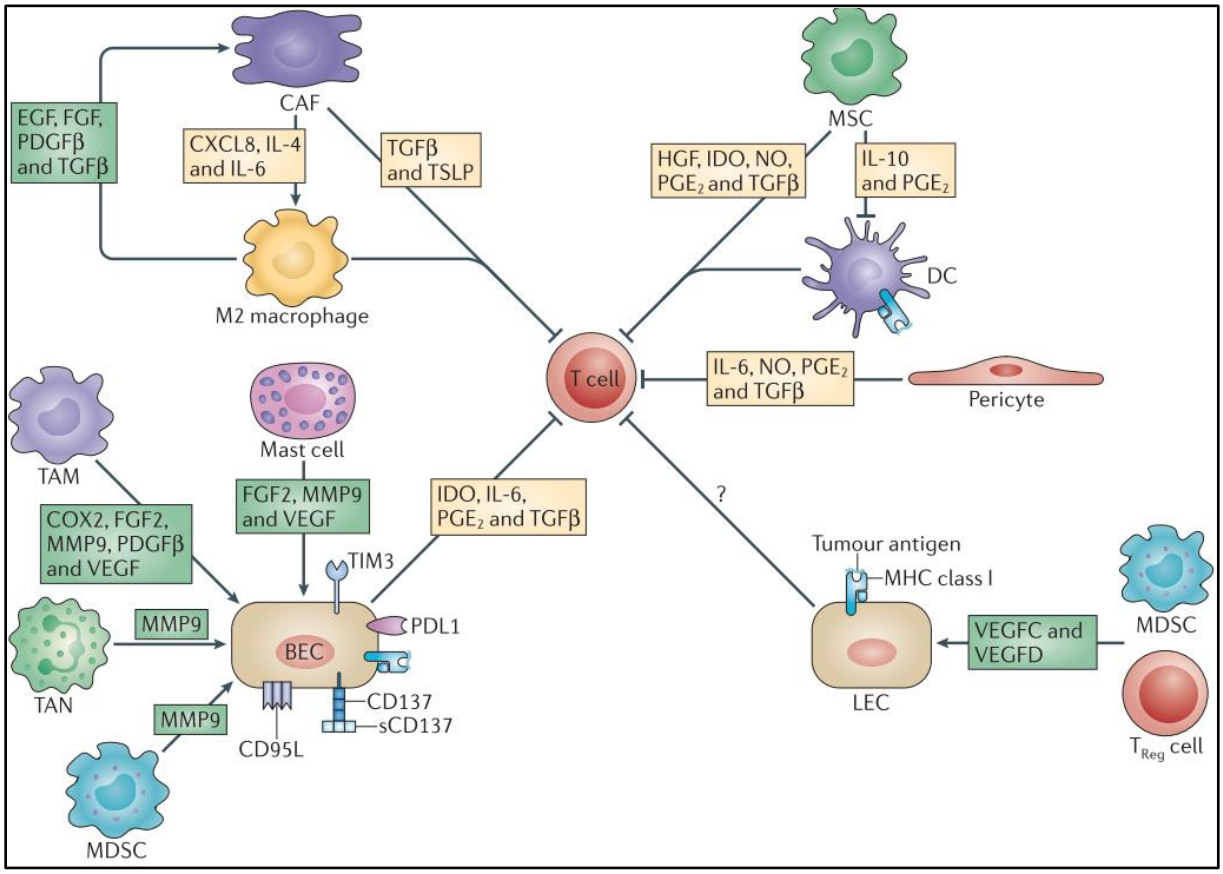


*Figure 7 : Stromal surface and secreted factors in the TME contribute to immune cells inhibition*

*Blood endothelial cells (BECs) express immunomodulatory receptor at their surface, such as PD-L1, TIM-3 and CD95L (FASL). In additon, BECs secrete IDO, IL-6, $PGE_2$, TGF-β and a soluble form of CD137, that impedes the engagement of the co-stimulatory receptor CD137 of T cells. TGF-β and thymic stromal lymphopoietin (TSLP) inhibit T cells and promote the differentiation in Th2. CAFs also support M2 macrophages secreting theinflammatory cytokines and chemokines CXCL8, IL-4 and IL-6. Also pericytes secrete various immunosuppressive factors, including IL-6, NO, PGE2 and TGFβ.*

*Of note, in the crosstalk within the TME innate immune cells can stimulate stromal cells. M2 macrophages secrete epidermal growth factor (EGF), fibroblast growth factor (FGF), platelet-derived growth factor-β (PDGFβ) and TGFβ, which activate CAFs and promote their survival. TAMs, TANs and MDSCs can secrete matrix metalloproteinase 9 (MMP9) to release growth factors trapped in the ECM and VEGF promoting BEC survival and angiogenesis.*

## 1.4 Ex-vivo cancer models

In the past decade, a rising number of studies targeted the development and the exploitation of 3D *ex vivo* cultures, in order to investigate organ physiology and perform disease modeling, including cancer.

Particularly in cancer biology, where the heterogeneity of the cells and of the interactions occurring in the TME play a strong role in cancer progression, 2D *in vitro* cultures have strong limitations: the lack of spatial organization of the different cell types present in tissues, the non-physiological mechanical environment, the dilution and diffusion of paracrine signals in the culture medium. *In vivo* cancer models are conventionally used in pre-clinical studies, but fail to accurately predict drug responses in humans, as shown by the low success rate of clinical trials (all supported by preliminary tests *in vivo*), with a drug approval lower than 5% [173].

*3D ex vivo* cancer models aim to reproduce as much as possible the physiological conditions present in the TME. Spheroids, tissue slides, organoids and tumors-on-chip are different approaches, which aim to recapitulate the complex features of human cancers. Certainly, each of those approaches has its advantages, compared to 2D culture, but also some drawbacks, as discussed below.

A major strength of the *ex vivo* 3D cancer models is the possibility to generate complex co-cultures using primary cells isolated from fresh patient samples, with the potential to perform personalized preclinical drug testing. Additionally, these culture techniques circumvent some biological and ethical limitations associated to animal studies, in the line with the principle of the 3Rs (Replacement, Reduction and Refinement).

3D cultures first started in early years of the XX century, when Harrison developed the hanging drop tissue culture technique [174]. Later studies showed that these 3D aggregates of cells, named spheroids, can be embedded in a matrix, potentially include other cell types, and recapitulate the 3D structure of a tumor with proliferative gradients and a necrotic center. Indeed, spheroids allowed to study several cell processes in a 3D setting, including: cancer cell proliferation, cancer cell migration, angiogenesis, hypoxia, immune cell responses,

and to perform drug screenings in 3D [175]. Nonetheless, spheroids lack of the tissue-specific spatial distribution of cell types and can be difficult to live-image.

More relevant 3D cancer models, from a technological and informative point of view, include organoids, organotypic cultures and tumors-on-chip (ToC).

### 1.4.1 Organoids

Organoids constitute a very quickly expanding approach, within the 3D *ex-vivo* culture field. Organoids have the great capacity to recapitulate complex events, by using organ-specific progenitors that can self-organize to form roundish 3D structures with properties and functionalities similar to those present in the tissue of origin.

The first pioneering studies in regenerative medicine aimed at the reconstitution of 3D structures *in vitro* from the culture of human stem cells. These studies succeeded for example in the generation of a stratified skin from freshly isolated keratinocytes [176] or in the reconstitution of the cornea *in vitro* [177], with direct applications in the treatment of highly-grade burned patients or of ones suffering of corneal blindness.

Later in time, organoids were exploited in developmental biology studies, where organogenesis was recapitulated starting from tissue cells or pluripotent embryonic stem cells (ES) or induced pluripotent stem (iPS) cells. Specific cocktails of growth factors and complex protocols were optimized to recapitulate *ex vivo* some steps of organogenesis. This generated organoids reproducing some basics features of gut (including stomach and intestine), liver, brain, retinal, bone, mammary gland, skeletal muscle, kidney and lung [178]. Interestingly, some of these organoids were obtained from adult stem cells (aSCs) opening the possibility of reproducing self-organized organoids, also called tumoroids, for cancer biology studies.

Patient-derived organoids (PDOs) are a novel tool to recapitulate, from fresh biopsies, the TME of solid tumors, with the advantage of conserving the immune and stromal components of the patient. PDOs recently emerged as potential *ex vivo* cancer models for therapeutic screening, as they reproduce and maintain many of the original tumor's characteristics. In a breakthrough paper, Vlachogiannis and colleagues reported the reproduction of organoids

from metastatic gastrointestinal cancers, which showed high histopathological and molecular similarities when compared to the original patient tumors. Strikingly, these PDOs reproduced the clinical responses observed intra-(responding lesion versus progressive lesions) and inter-patients treated with multiple anticancer treatments [179]. In another work, the same approach was exploited to constitute a biobank of more than a hundred breast cancer organoids, used as well for therapeutic screening [180]. Interestingly, Sachs and colleagues generated human lung organoids from iPS cells and obtained functional lung epithelium with multiciliated cells in the lumen and mucus-secreting cells. Moreover, using cells collected from resected primary lung cancers or from broncho-alveolar lavages of cystic fibrosis patients, they recapitulated the respective disease features [181]. PDOs from different lung cancer histological subtypes were reproduced and validated successfully also by Kim et al [182].

The ability of organoids to preserve many of the original tumor characteristics makes them excellent candidates for personalized drug screening. Nonetheless, as indicated in the above cited articles, it takes weeks (2 or more) to grow PDOs and an additional week to perform the drug testing. For some patients the decision process for therapy must be faster than that.

A second limitation resulting from the long-time culture needed to obtain PDOs, is the difficulty in the use of autologous immune cells that may be extracted from the initial tumor specimen. Immune cells are more sensible than cancer cells and in a 3 weeks-time period they would hardly survive or preserve their phenotype. A solution could be to isolate and freeze the immune cells at the beginning of the procedure.

An additional limit of the use of organoids as cancer model, is the difficulty of performing live imaging to study cell dynamics. In average PDOs measure 400µm diameters and the current imaging strategies include only end-point analysis, such as fixation and hematoxylin-eosin staining, IHCs or confocal imaging.

### 1.4.2 Organotypic cultures (tissue slices)

A different method to study the complexity of the TME is the use of tissue slices.

Tumor tissue slices are exploited to perform functional assays and to measure drug responses. Thin slices of 300 µm-1 mm thickness are cut from the original tumor and placed on a cell culture insert, which serves as scaffold, and submerged with culture medium. This way, tumor slices survive in culture up to 10 days [183]. An advantage of this strategy is the possibility to preserve the original topology of the tumor, leaving unaltered the spatial interactions between the tumor and the surrounding stroma. Importantly, tissue preserves as well the composition of the matrix, therefore maintaining the physico-mechanical properties of the TME.

Thanks to confocal and bi-photon microscopy on lung tumor slices, Salmon and colleagues showed that T cells motility is high in loose collagen regions. Oppositely, dense matrix areas drastically reduce the motility of T cells, which resulted constrained in the stroma [184]. Later, Peranzoni and colleagues pointed out the role of macrophages in the retention of T cells in the stroma, impeding them to reach the tumor islets in lung squamous-cell carcinoma slices [185].

Similarly to organoids, tissue slices are exploited to measure drug-responses. Martin and colleagues succeeded in establishing tissue slices from hepatic metastasis from colorectal cancer and tested the effects of clinically relevant drugs, such as Oxaliplatin, Cetuximab and Pembrolizumab. They assessed cancer cells proliferation and apoptosis, respectively measuring Ki-67 and caspase-3 activity and observed a dosage dependent susceptibility to Oxaliplatin treatment, whereas for the other drugs they observed a response only in a fraction of the patients [186]. Similarly, van de Merbel et al used *ex vivo* cultured patient-derived tumor tissues from prostate and bladder cancer and observed a dose-dependent apoptosis after treatment, respectively, with docetaxel and gemcitabine [187].

Karekla et al. performed *ex vivo* explants from NSCLC specimens, treated the tissue slices with cisplatin; accordingly, they observed a better overall survival in patients whose explants showed sensitivity to cisplatin [188]. These studies show that tissue slices can be used as preclinical-profiling platforms and to conduct functional studies through confocal imaging.

The limits of this 3D cancer model include the lack of control on the experimental conditions and the need of relatively big specimens. Moreover, for the live confocal imaging it is necessary to stain the cells. Albeit it is possible to stain the cells to perform live confocal imaging, phototoxicity would not allow to image for a long time (days) the cell responses to treatment.

### 1.4.3 Tumors-on-chip

Empowered by the advancements in microfluidics and in microengineering, organs-on-chip (OoC) aim to reproduce 3D physiological microenvironments that mimic the structures and the functionalities of a specific organ. Practically, custom microfluidic devices are designed and fabricated in a way to spatially organize the different cell populations with an in-vivo-like geometry; specific microstructures (e.g. pillars and membranes) allow the confinement of the cells in specific compartments. Here, the cells interact, physically and chemically, in a controlled 3D structure and reproduce organ-like functions.

In 2010, Huh and colleagues were the first to develop a lung-on-chip, establishing a functional alveolar-capillary interface in stretchable microsystems. To reproduce the air-liquid interface, a porous membrane to separated an upper air-containing chamber from a lower chamber filled with medium; epithelial cells were seeded on the air side of the membrane whether endothelial cells adhered to the lower side of the membrane. In order to replicate the continuous stretching movements of the lung, the authors applied vacuum in hollow lateral chambers causing a cyclic stretching of the structure containing the air-liquid interface [189]. This lung OoC was exploited in later studies, in which they set up models of human asthma inflammation, COPD [190] and intravascular thrombosis [191] for therapeutic response assessment, as well as a a drug-toxicity-induced pulmonary edema [192].

The features reproduced in OoC opened the way for the promising application of these culture systems in cancer research. The pioneers of the tumors-on-chip deserving of mention are David J. Beebe, Roger Kamm and Donald E. Ingber, who first implemented OoC models to study cancer biology. These authors used ToCs for modeling cancer-immune interactions [193], study cancer cell intravasation [194], cancer cell extravasation [195], angiogenesis [196]

and orthotopic breast [197] and lung cancers. Using the latest lung ToC model, an interesting observation was the negative influence of mechanical breathing on cancer growth and invasion and a decreased sensitivity to TKI drug, possibly linked to a mechanical regulation of EGFR expression [198].

ToC ex-vivo cancer models offer several advantages. First, the control of the geometry and physico-chemical properties of the chip allow to simplify and evaluate different facets of the complexity of TMEs. For example, the compartmentalization and the implementation of laminar flow provide features such as a biochemical gradients (to study cell motility), and gradients of stiffness and porosity (to investigate the impact the mechanical properties of the ECM [199]. Second, the microfluidic settings allow the integration of perfused microvascular structures in ToCs [200]. Third, the miniaturization of the ToCs allows to culture very small amounts of cell lines or human primary cells, making them suitable to work with small patient-derived samples. Fourth, microfluidic devices are transparent, therefore compatible with real-time recording of cellular dynamics. Live-imaging is a great asset for the description of immune-cancer interactions [201], [202].

In a previous work of our laboratory, Nguyen et al. reconstituted an immunocompetent tumor ecosystem (comprehensive of breast cancer cells, immune cells, CAFs and endothelial cells) which responded to both chemotherapy and targeted therapy (trastuzumab) recapitulating ex-vivo a ADCC effect (antibody-dependent cell-mediated cytotoxicity) [203]. Choi and colleagues developed a model simulating an early-stage breast cancer, including spheroids embedded on a layer of mammary epithelial cells and a lower stromal compartment, to evaluate the response to anticancer treatments [197].

Concerning the ToC limitations, the addition of more cell types and microstructures complicates the experimental setup and the manipulation of these devices. This translates so far in the privileged use, by researchers, of more resistant cellular models such as cell lines, over patient-derived samples. Nonetheless, Aref and colleagues succeeded in culturing organoids in microfluidic devices to characterize the response to anti-PD-1 treatment. In an end-point

analysis, they evaluated cancer cells viability, cytokine secreted and transcriptome profiling (by RNA-seq)[204].

Another limit of ToCs is the paucity of image analysis tools that can help users to extract the rich biological information contained in the ToCs. In fact, the evolving and original culture conditions of ToCs limit the standardization of the image analysis process.

# 2 Objectives

The tumors-on-chip is a new and expanding field of research exploiting miniaturized 3D structures in culture devices to reproduce specific *ex vivo* tumor features. My thesis project started shortly before the first publication of my hosting laboratory in this research field. In a paper published in Cell Reports, Nguyen and colleagues succeeded in treating with Trastuzumab (a monoclonal antibody targeting the HER2 receptor) a $HER2^+$ breast cancer cell line in presence of Peripheral Blood Mononuclear Cells (PBMCs) from healthy donors. In this culture settings they visualized and measured the antibody-dependent cellular cytotoxicity (ADCC) on-chip.

The aim of my thesis project is to study the response to immunotherapies in lung cancers-on-chip, with the long-term goal of exploiting ToC cultures for patients preclinical profiling. In this view, we needed to reconstitute an immunocompetent tumor microenvironment with an autologous cellular model and primary cells. The latter would be a key element to exclude any allogenic reactions of the immune system (misleading for our aim) and to move a step forward towards the application of ToC cultures with patient samples.

My thesis project was conceived with 3 main objectives:

1) The first objective is the development of tumors-on-chip technology, including the fine settings of on-chip co-cultures with primary cells and the implementation of the microfluidic system. Firstly, to setup co-cultures in biomimetic hydrogels of controlled composition and properties, under highly-controlled conditions, to generate tumors-on-chip with various primary cell populations (cancer, immune, endothelial cells and fibroblasts), reconstituting *ex vivo* the tumor microenvironment of lung cancers. Secondly, to build an adapted microfluidic circuit in order to connect the microfluidic devices under the microscope with the pressure controller and medium reservoirs. For instance, even though the microfluidic devices are purchased by AIM Biotech, the connectors commercially available (used to join the tubing with the inlets of the chip) do not fit in the microscope chamber. Therefore the connectors need to be custom designed and 3D-printed.

2) The second objective includes the high-content quantitative description of the tumor ecosystem dynamics, particularly regarding the cancer cells death and the cell-cell physical interactions with the immune cells. This goal includes the visualization and quantification of the anti-tumor cytotoxic activity of T cells from 2-3 day videos. Over the course of the thesis, this objective evolved into different deliverables. Shortly after the setup of the imaging strategy, we realized that a manual quantification was extremely time-consuming. Consequently, we realized that we would need to develop an informatic tool to quantify automatically the death of the cancer cells. In addition, it turned out that the study of cell mophodynamics and cell-cell interactions is extremely complex and requires more powerful image analysis approaches. We now think that the use of artificial intelligence could be a way to accomplish this task, in particular to find morphodynamics differences of T cells treated with ICI within lung ToCs.
3) The third objective involves the evaluation of the exploitation of such tumors-on-chip for pharmacology studies (characterization of drug alone or in combinations in meaningful *in-vivo* like contexts) and for translational research. We aim to use immunocompetent lung tumors-on-chip as drug testing platforms in which investigate the response to immunotherapies. This goal includes *in primis* the reproduction of the anti-tumor T-cell-dependent response on-chip and its stimulation with ICI treatment (anti-PD-1). Then, we aim to study the T cell plasticity in response to immunotherapy, measuring activation and exhaustion markers of the T cells. This should allow us to evaluate if the treatment with immunotherapy affects the expression of alternative immune checkpoints, that are potential therapeutic targets. The long-term goal will be to exploit tumors on-chip for patients pre-clinical profiling and exploit them to predict the personal response to drug treatments.

# 3 Materials and Methods

## 3.1 Cell cultures

The IGR-Pub lung adenocarcinoma cells, IGR-Heu large cell carcinoma cells, and their autologous TILs, the clone P62 and the T cell bulk of $CD8^+$ H5B respectively, were generated from fresh patient samples by the laboratory of Fathia Mami-Chouaib in Gustave Roussy. After thawing, TILs were amplified as reported [205]. The IGR-Pub and IGR-Heu cells were cultured in DMEM F12 (GIBCO) supplemented with 10% fetal bovine serum (Biosera), 1% of Ultroser G (Pall), 1% of Sodium Pyruvate (Gibco) and 1% Penicillin/Streptomycin (GIBCO). P62 and H5B T cells were cultured in RPMI-1640 (GE Healthcare) supplemented with 10% human AB serum (Institut Jacques Boy, Reims, France), rIL-2 (20 U/ml, Gibco), 1% of Sodium Pyruvate (Gibco) and 0,1% Penicillin/Streptomycin (Gibco). Primary human lung cancer-associated fibroblasts were purchased from Neuromics (CAF07-AD). All cell lines were periodically tested to exclude mycoplasma contamination using a qPCR-based method (VenorGem Classic, BioValley, #11-1250). Nivolumab (anti-PD-1) was purchased from Selleckchem (#A2002) and used at manufacturer's recommended concentration.

## 3.2 Cell staining

Before being seeded in the gel, cancer cells were labeled with CellTrace Yellow (#C34567, Thermofisher). First, cells were trypsinized and incubated at 37°C for 25 min at $1x10^6$ cells/ml density in PBS with 5 µM CellTraceYellow. Next, following a short incubation in warm cell medium for 5 min at 37°C, cells were centrifuged at 300g for 5 min, and resuspended in PBS.

## 3.3 Tumor-on-chip preparation

Cells were seeded in the central chamber of microfluidic devices purchased from AIM-Biotech (#DAX-1). Cells were embedded in a matrix composed of type I rat tail collagen (Thermofisher, #A1048301) at the final concentration of 2,3 mg/ml. Cancer cells were resuspended in the 4°C collagen solution at a final density of $2x10^6$ cells/ml. Autologous T cells were added at final densities at $1x10^6$ cells/ml or $2x10^6$ cells/ml, obtaining an effector to target (T cells/cancer cells ratio) of 1:1 or 1:2. Primary CAFs were embedded in the gel with a cancer

to CAF ratio of 5:1. After gel seeding, the microfluidic devices were incubated for 30 min at 37°C in a humidified chamber to allow the polymerization of the collagen solution. Next, 120 µl of T cells culture medium were added in each lateral chamber by pipetting. CellEvent Caspase-3/7 Green Detection Reagent (#C10423, Thermofisher) was added to the lateral chamber medium at 2µM final concentration. ICI drugs and isotype control were added either by addition to the lateral chamber medium or by microfluidic perfusion.

## 3.4 Drug perfusion

After the gel polymerization, custom 3D-printed connectors were sealed to the inlets with the help of epoxy resin (Araldite 2011, Huntsman). After medium injection, the microfluidic devices were kept for 2 hrs in the incubator before being transferred to the incubating chamber of the microscope for imaging. Here, each chip was connected with PTFE tubing (0.012" ID x 0.030" OD, Cole-Parmer) to the medium reservoir. The software AiO (all-in-one, Fluigent) allows to select the pressure applied on the medium in the reservoir by the pressure controller (MFSC-EZ, Fluigent). Located downstream the reservoir, a flow-unit (M, Fluigent) detects the flow rate (µl/min) and gives a feedback to the AiO software.

## 3.5 Live cell imaging

Time-lapse images were acquired with a 5X objective on an inverted Leica DMi8, equipped with a Retina R6 camera, Lumencor SOLA SE 365 light engine, motorized stage for multi-positioning acquisition, CO2 pressure controller and temperature-controlled (37°C) incubator chamber. AIM-Biotech devices were uplifted with magnets (1 mm thick) in order to expose the gas-permeable membrane, sealing the bottom of the devices, to the CO2%-controlled pressure of the microscope chamber. In order to achieve an optimal cell viability, with the aim to reach a saturating humidity in the chamber, we introduced humidified sponges in the microscope chamber and we filled with dd$H_2O$ the empty plastic inserts of the microfluidic device. The acquisition of images in transmission and fluorescent channels was performed every hour for a total duration of 48 hours.

## 3.6 Cells harvesting from the chip for flow cytometry analysis

For T cell profiling, ToCs were kept for 3 days in standard incubator, without perfusion. Then, culture medium was removed from the inlets reservoirs and the chip washed with PBS. Next, collagenase (4mg/ml, Sigma) was added in medium channels and incubated for 30min at 37°C. Cell suspensions were harvested from the chip and the collagenase inactivated with T cell medium.

## 3.7 Antibodies and flow cytometry analysis

Cancer cells were stained with anti-MHC-I (#740982, BD), anti-MHC-II (#, BD) and viability assessed through DAPI staining. For cancer-associated fibroblasts characterization, we followed the staining protocol described in previous publication of the laboratory [44].

T cells suspensions were transferred in 96-well plates v-bottom. In order to determine cell viability, cells were incubated for 20 min covered from light in PBS with Zombie NIR™ (Biolegend, #423105) at manufacturer recommended dilution. Directly conjugated anti-human antibodies were resuspended in PBS+ buffer (PBS 1% human serum, 2mM EDTA) and used to detect surface molecules on T cells by incubating them for 30 min covered from life. The following antibodies were purchased by BD: anti-CD4 (#566804), anti-CD8 (#563919), anti-CD69 (#747520), anti-CD25 (#741365), anti-PD1 (#562516), anti-CTLA-4 (562742), anti-LAG-3 (565616) and anti-CD137 (#745737). Anti-GITR (#15588146) was purchased by eBiosciences; anti-OX-40 (#350012) is a Biolegend product. Compensation controls were established using single color control compensation beads (#A10497, Termofisher) mixed with monostained T cells (H5B or P62).

Flow cytometry data were generated on a ZE5 flow cytometer (Biorad). The generated data were analyzed with FlowJo software (v10.6). The specific MFI (mean fluorescence intensity) was calculated as the ratio of the MFI detected in cells stained with antibodies over the MFI of cells incubated with the corresponding isotypes controls.

## 3.8 Image analysis

We used the STAMP method described in the submitted paper manuscript to quantify the death of cancer cells.

## 3.9 Statistical analysis

Statistical analysis and graphs were made with GraphPad Prism software (v8). Statistical threshold for significance was set for p-values inferior to 0.05 after applying paired t-test.

# 4 Results

## 4.1 Overview of the manuscript: "Apoptosis mapping in space and time of 3D tumor ecosystems reveals transmissibility of cytotoxic cancer death"

The tumor microenvironment (TME) is a cellular ecosystem in which complex interactions occur between cancer cells (carrying the disease-causing genetic alterations), infiltrated immune cells and other stromal cells (such as fibroblasts, pericytes and endothelial cells), which contribute to disease progression and drug responses. The emerging tumor-on-chip (ToC) approach allows to reconstitute in a very controlled manner *ex vivo* co-cultures in biomimetic 3D hydrogels embedded in microfluidic devices.

We reasoned that in order to measure in ToCs the efficacy of anti-cancer drug treatments, we needed to count the dying cancer cells, specifically among the other cell types. In order to distinguish cancer cells from other cell types present in the ToC, our imaging strategy consisted in selectively pre-staining the cancer cells with a fluorescent dye (red). By adding a live fluorescent reporter for caspase activity (green), we monitored apoptotic cell death during the ToC co-culture.

We realized that the bottleneck of this approach was the analysis of the generated videos. The first year of my PhD, I was counting manually the red cells turning green at each time point (every hour) in 48-hour videos, with an average of 12 positions imaged per each experiment. This process was not sustainable, being extremely time-consuming. For this reason, in order to automatize the counting process, we asked for help to our collaborators Eugenio Martinelli and Arianna Mencattini from the University of Rome "Tor Vergata". Having a background as electronic engineers, their research work in the past years focused on the advanced image analysis of biological phenomena.

The exchange of ideas and the discussions that followed translated in a very enriching experience. We faced the differences in our way of thinking, due to our diverse backgrounds, and on both sides we made efforts to adapt our scientific language in order to translate the biological requests in a mathematical output. In December 2018 I spent a month in Rome,

where Arianna Mencattini introduced me to MatLab language and to the practical usage of the novel algorithm, named STAMP (SpatioTemporal Apoptosis MaPper). This new computational method extracts the temporal kinetics of cancer death, by localizing and tracking cancer cells in the red channel and by counting the red to green transition signals over 2-3 days. Thanks to STAMP, we can now automatically quantify apoptotic events of cancer cells occurring in the ToCs co-cultures.

The application of the method to different cell models and co-culture combinations demonstrated its robustness and versatility. In this paper manuscript we quantify the cytotoxic effects induced either by doxorubicin (a chemotherapeutic agent) treatment on human breast cancer cells MDA-MB231, in presence or absence of CAFs, or by tumor-infiltrating T lymphocytes on autologous lung cancer cells (coming from the same patient). Noteworthy, this approach reveals the contribution of primary cancer-associated fibroblasts (CAFs) to breast cancer chemo-resistance, proving to be a powerful strategy to investigate intercellular cross-talks and drug resistance mechanisms. STAMP has different outputs. First, it calculates the apoptotic rate, which is the percentage of cancer cells dying within a certain time interval (4 to 10 h); this rate is calculated respect the living cells at the beginning of each time interval. Second, it calculates the overall survival as the percentage of cancer cells alive over time, using the number of cells at the beginning of the experiment as starting reference; therefore this parameter takes into account both cell death and proliferation and can be graphed as a “survival curve” of the cancer cells.

Intrigued by the observation that the apoptosis rate increased with the time of co-culture, we defined a new parameter: the potential of death induction. This parameter quantifies the impact of dying cells on neighbor cells. In order to compute the potential of death induction, we created maps of death integrating space and time information. From these spatio-temporal maps of cancer death, we uncovered unsuspected relations between death events. We found that, contrarily to natural death, cancer death induced by chemotherapy or by CTL is transmissible, meaning that it promotes the death of nearby cancer cells in close time points. These surprising results suggest that the release of diffusible factors may amplify the initial cytotoxic stimulus and enriched of original biological implications our methodological

study, initially conceived to simply automate the counting of dying cells.

Finally, when our paper manuscript was ready for submission, the office of intellectual property in Roche and Hamasseh Shirvani, my thesis co-director, pointed out that the method was worth being the subject of a patent and introduced us to the patent filing process, which is now concluded.

This project is an example of how research can be versatile and lead us to unexpected results and applications.

## 4.2 Paper manuscript in review

**Submitted to:** Plos Computational Biology

**Title:** Apoptosis mapping in space and time of 3D tumor ecosystems reveals transmissibility of cytotoxic cancer death

**Short title:** Automated cytotoxicity quantifications in tumor-on-chip

Irina Veith[1,2,§], Arianna Mencattini[3,§], Valentin Picant[2], Marco Serra[4], Marine Leclerc[5], Maria Colomba Comes[3], Fathia Mami-Chouaib[5], Jacques Camonis[2], Stéphanie Descroix[4], Hamasseh Shirvani[1], Fatima Mechta-Grigoriou[2], Gérard Zalcman[2,6], Maria Carla Parrini[2,*], Eugenio Martinelli[3,*]

[1] Institut Roche, 4 Cours de l'Île Seguin, 92100 Boulogne-Billancourt, France.

[2] Institut Curie, Inserm U830, Stress and Cancer Laboratory, PSL Research University, 26 rue d'Ulm, 75005 Paris, France.

[3] Department of Electronic Engineering, University of Rome Tor Vergata, Rome, Italy

[4] Institut Curie, CNRS UMR168, Laboratoire Physico Chimie Curie, Institut Pierre-Gilles de Gennes, PSL Research University, Paris, France

[5] INSERM UMR 1186, Integrative Tumor Immunology and Immunotherapy, Gustave Roussy, Fac. de Médecine - Univ. Paris-Sud, Université Paris-Saclay, 94805, Villejuif, France

[6] CIC Inserm1425, Thoracic Oncology Department, University Hospital Bichat-Claude Bernard, University of Paris

[§] Equal first author contributions

* Equal last author contributions

Correspondence: martinelli@ing.uniroma2.it, maria-carla.parrini@curie.fr

**ABSTRACT**

The emerging tumor-on-chip (ToC) approaches allow to address biomedical questions out of reach with classical cell culture techniques, by partially reconstituting *ex vivo* in biomimetic 3D hydrogels the complexity of the tumor microenvironment and the cellular dynamics involving multiple cell types (cancer cells, immune cells, fibroblasts, *etc.*). However, a clear bottleneck is the extraction and interpretation of the rich biological information contained, sometime hidden, in the cell co-culture videos.

In this work, we develop and apply novel video analysis algorithms to automatically measure the cytotoxic effects on human cancer cells (lung and breast) induced either by doxorubicin chemotherapy drug or by autologous tumor-infiltrating cytotoxic T lymphocytes (CTL). A live fluorescent dye (red) is used to selectively pre-stain the cancer cells before co-cultures and a live fluorescent reporter for caspase activity (green) is used to monitor apoptotic cell death. The here described computational method, named STAMP (Spatiotemporal apoptosis mapper), extracts the temporal kinetics and the spatial maps of cancer death, by localizing and tracking cancer cells in the red channel, and by counting the red to green transition signals, over 2-3 days. The robustness and versatility of the method is demonstrated by its application to different cell models and co-culture combinations. Noteworthy, this approach reveals the strong contribution of primary cancer-associated fibroblasts (CAFs) to breast cancer chemo-resistance, proving to be a powerful strategy to investigate intercellular cross-talks and drug resistance mechanisms. Moreover, we defined a new parameter, the 'potential of death induction', which is computed in time and in space to quantify the impact of dying cells on neighbor cells. We found that, contrary to natural death, cancer death induced by chemotherapy or by CTL is transmissible, in that it promotes the death of nearby cancer cells, suggesting the release of diffusible factors which amplify the initial cytotoxic stimulus.

**AUTHOR SUMMARY**

The tumor microenvironment (TME) is a very complex cellular ecosystem, composed of the cancer cells (carrying the disease-causing genetic alterations), immune cells and other stroma cells (such as fibroblasts), which contribute to disease progression and drug

responses. Here, we investigated these complex cellular dynamics by reconstituting the tumor ecosystems in a very controlled manner within microfluidic devices, with multiple cell populations, generating the so-called 'tumors-on-chip', which can be visualized by video-microscopy and treated with anti-cancer drugs. The resulting videos contain a huge amount of information that requires advanced computational approaches to be extracted. In this work, we developed a novel method, named STAMP, that precisely measures the kinetics and the spatial maps of cancer cell deaths within tumor-on-chip. Two case studies are presented: breast cancer cells upon chemotherapy treatment (doxorubicin) and lung cancer cells upon killing by specific immune cells (tumor-infiltrating cytotoxic T lymphocytes). We generated spatio-temporal maps on cancer death uncovering unsuspected relations between death events. This indicates that dying cancer cells might release soluble factors that induce death of neighbor cancer cells. The STAMP method was suitable to study the capacity of fibroblasts to promote resistance of cancer cells to chemotherapy.

## INTRODUCTION

Recent advances in microfluidics and microfabrication inspired new solutions to reproduce *ex vivo* 3D microarchitectures on chip imitating characteristics of organ functional units and of tumor microenvironments (TME). This established the basis for the technology of organ-on-chip (OoC) [1–3] and tumor-on-chip (ToC) [4–6]. The OoC/ToC technology offers numerous advantages, such as tight control of biological and physicochemical conditions (cell types, 3D biomimetic hydrogel, biochemical environment), real-time observation of cellular dynamics, miniaturization (few cells and little reagent are needed), fast results, and lower costs. Despite this huge potential, so far, the ToC use has been restrained to specialized laboratories and has not reached the broad community of cancer researchers. Several promising applications in basic and translational research, as well as in clinics, have been proposed, but their implementation clearly requires further developments. In particular, a major bottleneck of ToC technology is the lack of standardized user-friendly computer tools to process, analyze, and fully exploit the rich information generated by ToC imaging. The integration of advanced image analysis tools and deep learning methods is expected to

foster new powerful solutions to this problem.

Our previous works demonstrated the feasibility of reconstituting on-chip various tumor ecosystems, composed of up to four cell types (cancer cells, immune cells, cancer-associated fibroblasts [CAF], and endothelial cells), which can be treated with various anti-cancer drugs, including standard chemotherapies and targeted therapies (*e.g.*, trastuzumab) [7–9]. The videos faithfully monitor the cancer death, in time and space, upon these various treatments. In this work we develop, validate and apply a novel computational method, named STAMP, to automatically extract the temporal kinetics and the spatial maps of cancer death in ToC cultures.

Because of their capacity to capture the cell death kinetics, image analysis approaches are progressively replacing the historical end-point cytotoxic assays, such as the luminescent detection of ATP [10] or the $^{51}$Cr-release assay [11]. For example, a recent work combines live/dead cell markers and mathematical modeling to achieve a high-throughput analysis of cell death kinetics with over 1800 bioactive compounds [12]. Similarly, image analysis algorithms to measure cytotoxic or apoptotic index are commercially available (*e.g.*, IncuCyte-Essen BioScience or NanoLive). A real-time bio-imaging cytotoxic assay has been proposed for 96-well microplate [13]. All these software tools have been conceived to work in 2D settings, with focus on temporal information. Recently, an ingenious 96-well microfluidic platform was developed to perform bio-imaging cytotoxic assay in 3D gels [14]. Since 3D microfluidic devices allow to keep confined the cells as well as their released soluble factors, they are appropriate to investigate the consequences of each death event on surrounding cells. For this purpose, we focused on analysis strategies to extract not only the temporal information, but also the spatial information of cancer death events. STAMP introduces the new concept of 'potential of death induction', by calculating the induction that each death region (defined as 'object') produces on the surrounding regions, with respect to their mutual distances and to their temporal relationships. The combination of measures both in time and in space allowed us to conduct an original apoptosis analysis that accounts not only for the number of death events and their kinetics, but most shrewdly for their spatial distribution in the 3D confined environments of ToC cultures.

## RESULTS

### Imaging strategy to monitor cancer death in tumor-on-chip (ToC) co-cultures

In order to generate 3D tumor-on-chip (ToC) co-cultures, we used commercially available microfluidic devices in plastic (AIM-Biotech), that were imaged under an inverted video-microscope with controlled $CO_2$ (5%) and temperature (37°C) for 2-3 days. Cells were embedded in a 3D biomimetic collagen gel and injected in the 3.41 $mm^3$ chamber of the microfluidic device.

For this work we generated mono-cultures (cancer cells only) and two kinds of bi-cultures (cancer cells with immune cells, cancer cells with CAFs). For all experiments, a live fluorescent dye (CellTrace, red) was used to selectively pre-stain the cancer cells before cultures on-chip, and a live fluorescent reporter for caspase activity (CellEvent Caspase-3/7, green) was added to on-chip culture medium to monitor apoptotic death. No matter the degree of co-culture complexity, the cancer death detection was achieved by monitoring the red to green signal transitions.

### Description of the STAMP method

A computational strategy was developed to automatically and objectively monitor, in time and in space, the events of apoptotic cancer cell deaths, *i.e.* the red to green signal transitions (Figure 1, see Materials & Methods for details). The software was named STAMP, from Spatiotemporal apoptosis mapper.

Briefly, from multi-channel videos of ToC co-cultures, the cancer cells are localized and tracked in the red channel. The dying cancer cells are identified in the green channel, after signal normalization and thresholding. The death signal is modeled to vanish during T time frames. Then, the spatiotemporal features of all death signals are integrated in a unique map, from which a novel parameter, named potential of death induction ($P_{death}$), is computed over time.

Several output measurements were extracted and used for the following analysis. First, the apoptotic rate, *i.e.* the percentage of cancer cells dying within a certain $T_{LAG}$ time interval (4

to 10 h, in this study), calculated using the number of cells at the beginning of each time interval as starting reference. Second, the overall survival, *i.e.* the percentage of cancer cells alive over time, which is calculated using the number of cells at the beginning of the experiment as starting reference and therefore takes into account both cell death and proliferation. Third, the spatiotemporal map of death events, integrating the information of when and where all deaths occur. Fourth, the potential of death induction ($P_{death}$) within a $\tilde{T}$ time over the entire field of view and experimental time, measuring the capacity of dying cells to promote the death of nearby living cells in the 3D experimental setting.

**Application to quantify chemotherapy-mediated cytotoxicity in breast-cancer-on-chip cultures**

First, we applied the STAMP method to analyze the response of a standard cell model, the triple-negative breast cancer MDA-MB-231 cells, to a standard chemotherapy drug, doxorubicin (Figure 2, Video 1 and 2). To achieve a moderate killing, we chose a doxorubicin concentration of 1 μM, which is slightly lower than the IC50 of doxorubicin for MDA-MB-231 cells (2.8 μM), that we previously measured in standard 2D dishes.

In order to benchmark the accuracy of the automated method, we compared the values obtained by the algorithm with those obtained by manual counting. The values closely matched for all the time points and conditions (Figure 2C); we never found statistically significant differences between automated and manual counting, indicating that the algorithm is validated with respect to a standard human-controlled quantification method.

In control MDA-MB-231 cells without drug, the basal apoptosis rate in 10 h-time-intervals ($T_{LAG}$ = 10 h) fluctuated around 5% during the experiment time (72 h), meaning that roughly 5% of the cells died every 10 h (Figure 2C, left). In doxorubicin-treated cells, the death rate remained at basal level during the first 20 h of treatment, then after 20 h of doxorubicin exposure the death rate increased up to more than 10% (Figure 2C, right). Therefore, the time-resolved STAMP analysis revealed that the speed of cytotoxic response to doxorubicin increases with the time in this 3D on-chip setting.

**Application to quantify T-cell mediated cytotoxicity in lung-cancer-on-chip cultures**

Next, we challenged the STAMP method with a more complex situation in which a non-small cell lung cancer (NSCLC) cell line (IGR-Pub) was co-cultured with an autologous CTL clone (P62) that was generated from tumor-infiltrating lymphocytes (TIL) and selected to recognize and kill the cognate target [15] (Figure 3, Video 3 and 4). To achieve a moderate killing, we chose a 1:1 effector (CTL) to target (cancer) cell (E:T) ratio.

The algorithm could accurately distinguish the prestained cancer cells from the unstained T cells, and again all the values obtained by the algorithm were not statistically different from the values obtained by manual counting (Figure 3C).

The basal apoptosis rate of IGR-Pub cells in 10 h-time-intervals ($T_{LAG}$ = 10 h) was very low (around 2%) during the experiment time (48 h). The presence of the T cells immediately induced a significant death rate (around 10%); after 30 h of co-cultures the apoptosis rate dramatically increased (up to 30%). Interestingly, similarly to what observed for cytotoxic response to doxorubicin (Figure 2C, right), the speed of cytotoxic response to CTL appears to increase with the time as well (Figure 3C, right).

We further characterized the real-time dependency of T-cell mediated cytotoxicity on T-cell density by using different E:T ratios with a better time resolution ($T_{LAG}$ = 4 h) (Figure 4). At low T-cell density, 1:10 E:T ratio, the apoptosis rate was not different from the control without T cells. A mild killing started to appear at 1:2 E:T ratio, but only at 1:1 ratio, an efficient killing could be detected (Figure 4A). Interestingly, there was not a linear proportionality between density and killing capacity of T cells, suggesting threshold effects. Again, the death rate increased with the time of co-cultures, despite the fact that after 2 days on chip the T cell viability was reduced (around 90 %).

Consistently, the overall survival curves of cancer cells, which takes into account the balance between cell death and cell proliferation (the on-chip IGR-Pub doubling time being approximately 5 days), showed a detectable T-cell mediated killing only for the 1:2 and 1:1 ratios (Figure 4B), with a near 80% and 40% overall survival respectively, after 48-h co-cultures.

**Cancer-associated fibroblasts promote chemo-resistance in breast-cancer-on-chip**

Having established that STAMP is accurate to monitor cancer death within co-cultures of cancer and T cells, we moved to bi-cultures of cancer cells and CAFs. CAFs are a major component of the stroma which is crucial for tumor progression; in NSCLC tumor-stroma ratio could be used as prognostic factor for survival [16]. Since it is well established that CAFs contribute to chemo-resistance in various cancer types [17–22], we assessed the capacity of ToC to recapitulate *ex vivo* the CAF impact on doxorubicin resistance by co-culturing primary breast CAFs [8,23] with the breast cancer MDA-MB-231 cells (Video 5 and 6). Although the addition of CAFs (1:6 CAF:cancer cell ratio) does not substantially alter the basal MDA-MB-231 apoptosis rate, it completely impairs doxorubicin-dependent apoptosis (Figure 5). These results indicate that ToC technology and STAMP quantifications will be very valuable to study the mechanisms underlying stroma contribution to cancer progression and to drug resistance.

**Spatiotemporal analysis of cytotoxicity death reveals the release of pro-apoptotic signals**

In addition to the temporal kinetics, the STAMP method allows to extract the localization of dying cells, to build cumulative spatial maps of time-integrated death events, and to compute a potential of death induction ($P_{death}$) that quantifies the capability of dying cells to promote the death of nearby cells (see Material and Methods for mathematical details and Video 7 for a representative STAMP output video).

The $P_{death}$ (see Eq. (11)) combines in a unique parameter both spatial and temporal death induction effects. On one hand, the spatial distribution of regions with death events (dense or sparse) contributes to the final value of $P_{death}$ thanks to the dependency on the inverse of the mutual distances. On the other hand, the average value of the cumulative map MC, that takes into account the effect of the death wake in the temporal window $\tilde{T}$, contributes to $P_{death}$ thanks to the direct dependence on MC calculated for all paired death regions. In Supplementary Figure 1, we provide a simulated example for the $P_{death}$ calculation, to qualitatively explain how this parameter integrates both spatial and temporal properties.

We computed $P_{death}$ for the videos of both breast MDA-MB-231 and lung IGR-Pub cells (Figure 6, Supplementary Figure 2). In basal conditions, without drug or T cells, $P_{death}$ is low for both cell types (< 0.1-0.2 x$10^{-3}$) and globally stable over the experimental time (2-3 days), meaning that naturally dying cancer cells do not have an impact on viability of nearby cells. When cytotoxic death of MDA-MB-231 cells is induced with doxorubicin, $P_{death}$ gradually increases up to 3-4 folds during the first 2 days, and remains high during the 3$^{rd}$ day, meaning that doxorubicin-dependent cytotoxic death actually promotes the death of nearby cells. Similarly, when death of IGR-Pub cells was induced by autologous CTL, $P_{death}$ is higher than the control without T cells from the start of co-cultures, and further increases during the 2-day experimental time, suggesting that T-cell-dependent cytotoxic death promotes the death of nearby cells as well.

$P_{death}$ increase does not simply result from the increase of death numbers over time, but it depends also on the death positions, as shown by the simulations reported in Supplementary Figure 3. Indeed, an artificial video, with the same rate of death events as a real video (in this case, MDA-MB-231 cells treated with 1 µM doxorubicin), but with a spatially random distribution which maintains approximatively the relative death object distances as the real video, displays a computed $P_{death}$ increase much lower than the one measured for the real video. Moreover, when artificial videos with the same rate of death events but different spatial distribution (random versus clustered) are compared, the computed $P_{death}$ is much higher for the clustered deaths than for the random deaths, but in both cases it does not increase over time.

Therefore, the real $P_{death}$ kinetics depend on both temporal and spatial features, and suggest the possibility that, contrary to naturally dying cancer cells, the cells that enter into apoptosis triggered by chemotherapy or T cells, send pro-apoptotic signals to neighbor cells, initiating a chain of death that amplifies the initial cytotoxic effect.

## DISCUSSION

### The STAMP method

We report here a new method, STAMP, which extracts the temporal kinetics and the spatial

maps of cancer death events within ToC co-cultures. The robustness and versatility of the method is demonstrated by its successful application to different cell models (breast and lung cancers), co-culture combinations (cancer cell alone, or together with T cells or CAFs), and experimental time-lapse acquisitions (frequency and duration). The STAMP image analysis method might be useful for many other cellular contexts and biological questions, beyond the ToC technology. This adaptability to multiple experimental conditions is possible thanks to the integration within the STAMP software of three modular parameters.

First, the $T_{LAG}$ mentioned in step 6-iii and used in Eq. (4) (see Material & Methods). $T_{LAG}$ is the temporal window used to measure the average number of apoptotic events $N_{ap}(t, T_{LAG})$ and the average number of living cells $N_{avg}(t, T_{LAG})$, allowing to compute the percentage of apoptosis events. $T_{LAG}$ should be set depending on the time frame image acquisition frequency and on the desired time resolution of the investigated phenomenon. For example, the acquisition frequency being every 1 h in this study, the choice of $T_{LAG}$ value is bounded below. However, $T_{LAG}$ values larger than acquisition frequencies were more appropriate to avoid spurious fluctuations due to uncontrollable changes affecting the measurements (*e.g.*, abrupt change in illumination). Conversely, $T_{LAG}$ is also bounded above by the necessity to avoid flattening dynamic phenomena. We set $T_{LAG}$ to 10 h for Figures 2 and 3 whose purpose was the compare global accuracies, and to 4 h for Figure 4 whose purpose was to compare kinetics.

Second, the parameter *r*, included in the morphological operator $\Psi_{\mathrm{E}}^{\mathrm{B}}$ (Eq. (7)). The dimension of *r* impacts on the death wake construction. In particular, starting from a circular object of radius $r_{tc}$ the effect of the application of the operator in Eq. (7) is to restrict the object radius of a quantity equal to *r*. Hence, by indicating with $t_0$ the time at which the cell *tc* dies and with t a generic time frame such that $t > t_0$, the radius vanishes according to the formula

$$r_{tc}(t) = \max(0, r_{tc}(t_0) - r \cdot (t - t_0))$$

By setting *r* as one third of $r_{tc}$ the equation can be re-written as

$$r_{tc}(t) = \max(0, r_{tc}(t_0) - \frac{1}{3} r_{tc}(t_0) \cdot (t - t_0) =$$

$$= \max\left(0, r_{tc}(t_0)\left(1 - \tfrac{1}{3}(t - t_0)\right)\right) = \max(0, r_{tc}(t_0)(1 - \tfrac{1}{3}\Delta t)$$

where it can be noted that for at least three hours ($\Delta t$=3) the wake exists.

Third, the parameter $\tilde{T}$, in computation of MC (Eq. (9)) and of $P_{death}$ (Eq. (11)). $\tilde{T}$ is the time window over which the aggregation of deaths and their wake were computed by means of the definition of the cumulative map *MC* (Eq. (9)). Then, for each $t \in \{1, .. T - \tilde{T}\}$, the potential of death induction $P_{death}(t, \tilde{T})$ simultaneously measured the spatial and temporal death induction effects at time $t$. The value of $\tilde{T}$ has a key role in the quantification of death induction: a too small $\tilde{T}$ value results in the under-detection of genuine death induction effects, while a too large $\tilde{T}$ value causes a miss-leading flattening effect.

In this study, we set $\tilde{T} = 16$ h for both breast and lung cancer cells, based on the mathematical investigation of an *induction interval* that was associated to each cell and computed as follows. Let us consider a tumor cell $tc$ centered in $(x_{tc}(t), y_{tc}(t))$ with radius $r_{tc}(t)$ at the time of its death, $t = T_{tc}^{death}$. We assume that from its beginning at $t = T_{tc}^{death}$, the apoptosis of the cell $tc$ induces some deaths and these deaths cause others and so on, by creating a *chain of death* started from the cell $tc$. We constructed this chain by involving deaths that occurred in a circular zone of radius equals to $10 \cdot r_{tc}(t)$, centered in $(x_{tc}(t), y_{tc}(t))$, at a temporal distance from each other equals to $T_{LAG}$. The total duration of the *chain of death* defines the *induction interval* related to the cell $tc$. The distributions of the duration of the induction intervals of cells from 16 videos from 2 experiments (Supplementary Figure 4), show that vast majority of induction intervals is below 16 h, meaning that $\tilde{T} = 16$ permits to capture the vast majority of chain of death events.

**The biological implications**

Among the various types of cell death [24], this work specifically investigates the programmed apoptosis which involves the activation of the cascade of caspase enzymes. Both cytotoxic stimuli we used are known to promote apoptosis of cancer cells. Doxorubicin,

which acts by causing irremediable DNA damages in dividing cells, has been shown to induce apoptosis on breast cancer cell lines in vitro [25], as well in breast cancer patients *in vivo* [26]. The CTL clone (P62) used is this work kills autologous cells (IGR-Pub) at least in part via Apo2L/TRAIL-dependent pathway [15].

By using novel mathematical (potential of death) and computational (STAMP software) strategies, we achieved an original spatiotemporal analysis of apoptotic cancer death in the 3D confined environments of ToC cultures. Surprisingly, contrary to natural death, both doxorubicin-dependent and T-cell-dependent cytotoxicity toward target cells promoted the death of nearby cancer cells, indicating that dying cancer cells might release soluble pro-apoptotic signaling factors and trigger a chain of death that amplifies the initial cytotoxic stimulus.

Apoptotic cells do not passively empty their cellular content but they actively release various signals, named as damage-associated molecular-pattern (DAMP) molecules [27]. First, they release 'find-me' and 'eat-me' signals (such ATP and UTP nucleotides, the CX3CL1 chemokine, and the bioactive lipid metabolites lysophosphatidylcholine (LysoPC) and sphingosine-1-phosphate (S1P)), which enhance the attraction of phagocytes to dying cells and their consequent phagocytic clearance (a process called efferocytosis) [28]. Second, they send metabolite 'good-bye' signals with biological functions (such as AMP, GMP, creatine, spermidine, glycerol-3-phosphate (G3P), ATP), which act as tissue messengers altering gene expression of healthy nearby cells, for example suppressing inflammation [29]. Third, in the case of apoptotic cancer cells, they secrete cytokines/chemokines (such as IL-8, CCL2, CXCL1, CXCL2, CXCL5) that act as 'immunomodulatory' signals, promoting for example the polarization of monocytes to M2-like cells with consequent establishment of a tumor-supportive immune microenvironment [30]. Fourth, our findings indicate that apoptotic cancer cells release unknown 'pro-apoptotic' signals that directly induce death of neighboring cells, without intervention of phagocytic macrophages, absent in our co-culture models. Identification of these compounds warrants more work. We estimated that the diffusion times of potential signaling molecules of various sizes (*e.g.*, 100-500 Da for nucleotides, lipid metabolites, organic compounds or 10-20 kDa for cytokines), between cells

with a distance in the 20-100 micron range, within the collagen gel (2.3 mg/mL), are very low, less than 10 minutes. Therefore, these diffusion times are fully compatible with the hypothesis of release of pro-apoptotic compounds from dying cells, triggering chains of deaths that last for 2-14 hours (Supplementary Figure 4). Importantly, the biology of development teaches us that many secreted factors control apoptotic death events, spatially and temporally, to build multicellular organisms [31]. Pro-apoptotic compound candidates might be searched among these already known killers. However, at this stage we cannot exclude the implication of other processes in shaping the cytotoxic spatiotemporal behaviors. For example, the 20 h latency in the response to doxorubicin (Figure 2C, right) might be caused by the necessity for cancer cells to enter DNA replication phase or by the time-dependent intracellular accumulation of this drug [32]. In lung cancer-T cell co-cultures, the late burst of death after 30 h of co-culture (Figure 3C, right) might be due at least in part to a further activation of T cells upon co-culture with the target cells.

The phenomenon of 'death transmissibility' or 'death contagiousness' we unveiled in our *ex vivo* experimental setting might be linked to the well-known bystander effects observed in clinics [33]. Radiation-induced or chemotherapy-induced or immunotherapy-induced bystander effects refer to the induction of biological effects in cells that are not directly treated by radiation or chemotherapy or immunotherapy, but are in close proximity to cells that are. In our specific cases, all cancer cells are treated with doxorubicin or co-cultured with CTL, but the cells for which the treatments are effective have an indirect, unexpected, effect on the nearby cells.

In conclusion, this interdisciplinary work, by combining cancer biology, microfluidic engineering, mathematical modeling and computational analysis, created an innovative and needed image analysis method (STAMP), confirmed the power of ToC technology and shed a new light on the complexity of tumor ecosystem, emphasizing the intricacy of its non-autonomous cell behaviors.

## MATERIALS AND METHODS

### Cell cultures

The MDA-MB-231 cell line, from triple negative breast cancer, was cultured in high-glucose DMEM (GE Healthcare, #SH30081.01) supplemented with 10% fetal bovine serum (Biosera), 1% Penicillin/Streptomycin (Gibco), 1% glutamine (Gibco). The IGR-Pub lung adenocarcinoma cells and the autologous T cells P62 were generated from the same patient in one of our laboratories at Institut Gustave Roussy [15]. The IGR-Pub cells were cultured in DMEM F12 (GIBCO) supplemented with 10% fetal bovine serum (Biosera), 1% of Ultroser G (Pall), 1% of Sodium Pyruvate (Gibco) and 1% Penicillin/Streptomycin (GIBCO). P62 T cells were cultured in RPMI-1640 (GE Healthcare) supplemented with 10% human AB serum (Institut Jacques Boy, Reims, France), rIL-2 (20 U/ml, Gibco), 1% of Sodium Pyruvate (Gibco) and 0,1% Penicillin/Streptomycin (Gibco). Primary cancer-associated fibroblasts (CAFs) were isolated and cultured as previously reported [8,23]. All cell lines were periodically tested to exclude mycoplasma contamination using a qPCR-based method (VenorGem Classic, BioValley, #11-1250). The MDA-MB-231 cell line was authenticated by SRT profiling (GenePrint 10 system, Promega, #B9510). Doxorubicin was purchased from Teva pharmaceuticals (200 mg/100 ml).

**Tumor-on-chip preparation**

The microfluidic devices were purchased from AIM-Biotech (#DAX-1). Cells were seeded in the central chamber of the DAX-1 chips embedded in a matrix composed of type I rat tail collagen (Thermofisher, #A1048301) at the final concentration of 2.3 mg/ml. Cancer cells were seeded in the gel at a final density of $2x10^6$ cells/ml. Autologous T cells were added at final densities of $0.2x10^6$ to $2x10^6$ cells/ml in order to obtain different ratios (from 10:1 to 1:1) between cancer and T cells. Primary CAFs were added at CAF:cancer 1:6 ratio. The microfluidic devices were incubated for 30 min at 37°C in a humidified chamber to allow the polymerization of the collagen solution; afterwards, 120 µl of culture medium were added in each lateral chamber. MDA-MB-231 cells in chip were cultured in the same medium used for dish 2D culture, whereas the IGR-Pub/P62 co-cultures were in T-cell medium, supplemented with rIL-2 (10 U/ml, GIBCO, #PHC0027). After the addition of the medium, the microfluidic devices were kept for 1 h in the incubator before transfer to the incubating chamber of the

microscope for imaging.

**Cell staining**

Cancer cells were labeled with CellTrace Yellow before seeding in the gel (Thermofisher, #C34567), for the detection in the so-called "red channel" of fluorescence: cells were trypsinized, and then resuspended at $1x10^6$ cells/ml density in PBS with 5 µM CellTraceYellow; after incubation in cell medium for 5 min at 37°C, cells were centrifuged at 300g for 5 min, resuspended in PBS and added to the rat-tail collagen solution.

CellEvent Caspase-3/7 Green Detection Reagent (Thermofisher, #C10423) was added to the medium in the lateral chamber of the chip in order to visualize in the "green channel" the cells undergoing apoptosis.

**Live cell imaging**

Time-lapse images were acquired with an inverted Leica DMi8 equipped with a Retiga R6 camera and Lumencor SOLA SE 365 light engine, using a 5X objective. The video-microscope was equipped with a motorized stage for multi-positioning acquisition, a $CO_2$ and temperature-controlled (37°C) incubator chamber. Since in the AIM-Biotech devices the gas-permeability is provided by the underside sealing layer, before inserting them on the microscope stage, we placed them on a standard microscope glass slides and we lifted them using magnet holders (1 mm thick), in order to create an air circulating space underneath the devices, for $CO_2$ and temperature control. The presence of a saturating humidity in the microscope chamber was crucial for optimal cell viability, therefore distilled water was added in the plastic wells of the DAX-1 chips and humidified small sponges were added in the chip surroundings. The acquisition of images in transmission and fluorescent channels was performed every hour for a total duration of 48 h to 72 h.

**The STAMP method**

A STAMP software was developed under MATLAB environment. The STAMP method was applied on each video $V$, with spatial dimensions $D_1$ (number of row) and $D_2$ (number of

columns) and with a total duration of $T$ frames (from 48 to 72 depending on experiments, with a frame rate of 1 h).

Let us consider $(x, y, t) \in \{1, .., D_1\} \times \{1, .. D_2\} \times \{1, .. T\}$ the tuple indicating the position of the coordinates $(x, y)$ occupied by an arbitrary pixel on the video frame of $V$ acquired at time $t$, where $t = 1, \ldots, T$. Then, $V(x, y, t)$ indicates the video sequence with the specific coordinates $(x, y)$ at time $t$. We can refer to the video under examination indistinctly with $V$ or $V(x, y, t)$ to vary of $(x, y, t) \in \{1, .., D_1\} \times \{1, .. D_2\} \times \{1, .. T\}$.

**1. Cell localization and tracking.** Tumor cells (stained in red) were located and tracked in the red channel video of $V$ by adapting Cell-Hunter software to the frame rate of 1 h [7,34,35]. Localization was performed by preliminary binarizing the red channel video of $V$ by Otsu approach [36]. Then, Cell-Hunter was applied. Shortly, in each binarized video frame, the software implements the Circular Hough Transform (CHT) [37] which automatically locates tumor cells, assumed as circular-shaped objects of radius imposed, providing an accurate estimate of individual cell radii. Then cell trajectories/tracks were constructed by linking positions between consecutive frames according to an optimized procedure based on the concept of cell proximity and optimal assignment problem [38].

**2. ROI extraction around each tumor cell.** After tracking all the tumor cells along the video $V$, we isolated a square region of interest (ROI) 31 pixels x 31 pixels (about 20µm), centered around each tumor cell position along each track. In this way, we constructed a square section tube around each track. This procedure allowed us to confine the next analysis in the neighborhood of the tumor cells and to limit confounding factors in apoptosis analysis due to surrounding cells.

3. **Background and foreground identification.** Each ROI visualizes the cell (the foreground) and the background culture environment. To separate them, we segmented the tumor cells in the ROI by CHT approach and determined a neighborhood circular region around the cell by a given radius, here set to double the average radius of tumor cells.

4. **Time-dependent green emission signal extraction.** In order to extract the green emission signals of tumor cells (*i.e.* tumor apoptosis events), we transposed from the red to the green channel video the tracked positions of tumor cells (*i.e.* the centers of the cell regions automatically detected by Cell-Hunter software).

Let us denote as $(x_{tc}(t), y_{tc}(t)) \in \{1,..,D_1\} \times \{1,..D_2\}$ the pixel representing the position of the arbitrary tumor cell $tc$ at time-frame $t$ in the red and then green channel of video $V$, with $t \in F \subseteq \{1,\dots,T\}$, where $F = \{t_{tc}^{start},\dots,t_{tc}^{end}\}$ is the set of time-frames for which the cell track constructed by Cell-Hunter exists. We can define:

- $I_{GREEN}(x,y,t)$, the intensity value of the green emission signal referred to the pixel in position $(x,y)$ on the video frame acquired at time $t$ in the green channel, *i.e.*, the green channel video sequence of $V(x,y,t)$, with $(x,y,t) \in \{1,..,D_1\} \times \{1,..D_2\} \times \{1,\dots,T\}$,
- $R(x_{tc}(t), y_{tc}(t))$, the squared ROI centered on the position $(x_{tc}(t), y_{tc}(t))$ of the tumor cell $tc$ at time $t$, $t \in F$,
- $R_B(x_{tc}(t), y_{tc}(t))$ and $R_F(x_{tc}(t), y_{tc}(t))$, the circular background and the circular foreground regions within the ROI $R$, respectively, both centered on the position of the same tumor cell $tc$ at the same time $t$, $t \in F$.

Moreover, if $\bar{R}(x_{tc}(t), y_{tc}(t))$ is a generic ROI centered on $(x_{tc}(t), y_{tc}(t))$, *i.e.*, $\bar{R} = R \vee R_B \vee R_F$ for $t \in F$, and $(x,y)$ is a pixel on the video frame acquired at time $t$ in the green channel belonging to the ROI $\bar{R}(x_{tc}(t), y_{tc}(t))$, we can write $(x,y) \epsilon\ \bar{R}(x_{tc}(t), y_{tc}(t))$.

Then, in order to capture the information content of the green emission in the tumor cell $tc$ at a time $t \in F$, we proceed as follows

**4-i** Compute the average green emission signal in the foreground region $R_F(x_{tc}(t), y_{tc}(t))$, expressed by

$$\mu_{tc}^{R_F}(t) = \frac{1}{Area(R_F(x_{tc}(t), y_{tc}(t)))} \sum_{(x,y)\epsilon\ R_F(x_{tc}(t), y_{tc}(t))} I_{GREEN}(x,y,t). \quad (1)$$

**4-ii** Compute the average green emission signal in the local background $R_B(x_{tc}(t), y_{tc}(t))$, that is

$$\mu_{tc}^{R_B}(t) = \frac{1}{Area(R_B(x_{tc}(t), y_{tc}(t)))} \sum_{(x,y)\in R_B(x_{tc}(t), y_{tc}(t))} I_{GREEN}(x, y, t). \quad (2)$$

**4-iii** Perform background subtraction and normalization correction in order to avoid misleading surrounding green emission, thus obtaining $\mu_{tc}(t)$ as follows

$$\mu_{tc}(t) = \frac{\mu_{tc}^{R_F}(t) - \mu_{tc}^{R_B}(t)}{\mu_{tc}^{R_B}(t)} - \min_{\hat{t}\in F}\left(\frac{\mu_{tc}^{R_F}(\hat{t}) - \mu_{tc}^{R_B}(\hat{t})}{\mu_{tc}^{R_B}(\hat{t})}\right). \quad (3)$$

By computing $\mu_{tc}(t)$ for each $t \in F$, the time-depending signal $\mu_{tc}$ referred to the track of the tumor cell $tc$ is produced. The higher the signal is the higher is the green emission of the cell region and the probability to have an apoptosis event.

**5. Detection of the beginning of the apoptosis events.** Let assume $N$, the total number of detected tumor cells along the entire duration of the video $V$. From the previous step, $N$ time-dependent signals $\mu_{tc}$ were computed, one for each of tumor cells denoted as $tc$. We estimated a threshold value $th$ as the optimal inter-variance separation value of all the $N$ signals $\mu_{tc}$ (Otsu approach) [36]. For each tumor cell $tc$, we considered that the death by apoptosis occurs if $\mu_{tc} > th$ and that apoptosis begins at the time-frame at which the $\mu_C$ exceeds the value $th$ for the first time, $T_{tc}^{death} = \min_t\{t \in F |\ \mu_{tc}(t) > th\}$.

**6. Counting the apoptotic events.** In order to count the apoptotic events, we have to move from a tumor cell-centric view, used in depicting Steps 2-5, to a time-centric view. So, for each $t \in \{1, \dots, T\}$, we followed the approach below:

**6-i** Compute the number of apoptosis at time-frame $t$, $N_{ap}(t, T_{LAG})$, which sum up the number of apoptosis events found in the range $[t - T_{LAG}, \mathrm{t}]$ as the cumulative number of

tracks of tumor cells $tc$ whose signal $\mu_{tc}$ satisfies the condition $\mu_{tc}(t) > th$, for all $t \in [t - T_{LAG}, t]$ .

**6-ii** Compute the number of tracks of living cells at time-frame $t$, $N_{track}(t)$, as the number of tracks at time $t$ that did not yet go into apoptosis, *i.e.* the number of tracks whose $\mu_{tc}$ at time $t$ satisfies the condition $\mu_{tc}(t) < th$.

**6-iii** Compute the average number of tracks found in a temporal lag of $T_{LAG}$ frames, $N_{avg}(t, T_{LAG})$, as the average of $N_{track}(t)$ in the range $[t - T_{LAG}, t]$. The value of $T_{LAG}$ was defined in the order of a few hours (2-10 h) according to the desired temporal resolution and heuristic investigation (see Discussion).

**6-iv** Compute the percentage of apoptotic events in $T_{LAG}$ frames, $O(t, T_{LAG})$, as

$$O(t, T_{LAG}) = \frac{N_{ap}(t, T_{LAG})}{N_{avg}(t, T_{LAG})} \cdot 100\% \quad (4)$$

**6-v** Compute the average of surviving cells in each time point $N_{avg2}(t, t_{\pm 1})$, between 3 time points centered on t, as the average of $N_{track}(t)$ in the range $t_{\pm 1} = [t_{-1} - t_{+1}]$.

**6-vi** Compute the percentage of surviving cells, $OS(t, t_{\pm 1})$ (also referred as "overall survival"), as

$$OS(t, t_{\pm 1}) = \frac{N_{avg2}(t, t_{\pm 1})}{N_{avg2}(t, t_1 - t_3)} \cdot 100\% \quad (5)$$

Where $t_1$ and $t_3$ are the first and third time points.

**7. Construction of spatiotemporal maps of apoptotic events.** By using the information of death of the single tumor cell $tc$ (namely, position, $(x_{tc}(t), y_{tc}(t))$ for each $t \in F$ and timing of the apoptotic event, $T_{tc}^{death}$), we constructed a spatiotemporal map of death by the following procedure:

**7-i** An artificial video with the same spatial and temporal dimensions of video $V$, ($D_1, D_2, T$, respectively), was generated such that, for each tumor cell $tc$, at frame $t = T_{tc}^{death}$, the cell region, assumed as a circle and centered in the position $(x_{tc}(T_{tc}^{death}), y_{tc}(T_{tc}^{death}))$, was labelled with a white pixels, *i.e.*, with pixel intensity values equal to 1. It allowed to artificially reproduce the cell region of each tumor cell $tc$ at its time of death, $T_{tc}^{death}$.

Let us indicate with $MD(x, y, t)$ the artificial video sequence, with $(x, y, t) \in \{1, .., D_1\} \times \{1, .. D_2\} \times \{1, .. T\}$.

**7-ii** By assuming a spatiotemporal signaling of death produced by cells going into apoptosis, we constructed a new artificial video, $M(x, y, t)$, according to an iterative approach, expressed by:

$$M(x, y, t) = \Psi_E^B\big(M(x, y, t-1)\big) + MD(x, y, t), \qquad (6)$$

with $(x, y, t) \in \{1, .., D_1\} \times \{1, .. D_2\} \times \{2, .. T\}$, and $M(x, y, 1) = MD(x, y, 1)$.
The operator $\Psi_E^B$ denotes the gray-scale morphological erosion operator [35], with structure element $B$, defined as:

$$\Psi_E^B((M(x, y, t)) \triangleq \min_{(x', y') \in B} \{M(x + x', y + y', t)\}. \qquad (7)$$

It is the extended binary erosion operator defined on gray-scale intensity matrices. The global effect of the $\Psi_E^B$ operator is to reduce the area occupied by each white objects in the processed frame thus implementing a vanishing signaling that we called a *death wake* (see death signaling modeling step in Figure 1).
To apply the operator $\Psi_E^B$, in the present work, we used a circular structure element with radius *r*, *i.e.*, $B_r$ defined as:

$$B_r \triangleq \{(x, y) |\, x^2 + y^2 \leq r\} \qquad (8)$$

where the parameter $r$ is defined as one third of the estimated average cell radius in the experiment. The choice of $r$ depends on the need to simulate a wake with a reasonable duration with respect to the timing of the experiments (see Discussion).
The constructed artificial video $M(x, y, t)$ takes into account the death wakes of cells enabling to cumulate the death signaling in a given region.

7-**iii** We combined in a unique index both spatial and temporal death influence. First, given a temporal windowing of size $\tilde{T}$, we designed the cumulative map *MC* defined as:

$$MC(x, y, t, \tilde{T}) = \sqrt{\sum_{t'=t}^{t+\tilde{T}} (M(x, y, t'))^2}, \quad (9)$$

with $(x, y, t) \in \{1, .., D_1\} \times \{1, .. D_2\} \times \{1, .. T - \tilde{T}\}$. The cumulative map allows to aggregate the death events and their wakes over a given temporal interval equal to $\tilde{T}$, whose value needs to be optimized (see Discussion). Then, to account for spatial influence (*i.e.*, to discriminate randomly versus deterministically spatially distributed deaths) we defined a *potential of death induction* (Supplementary Figure 1).
Let us consider the temporal map $(x, y, t, \tilde{T})$ . Since cell death is a sparse phenomenon, most part of the map $MC$ is null. Hence, we can define a generic object $s(t)$ at frame $t$ as a region of the map $MC$ at time $t$ that is not connected with other non-null region, and indicate with $S(t)$ the set of not connected objects,

$$S(t) \triangleq \{s_i(t) | \, s_i(t) \cap s_j(t) = \varnothing, i \neq j\}. \quad (10)$$

Connection is defined under the 8-connectivity criterion [35]. Under these assumptions, for each $t \in \{1, .. T - \tilde{T}\}$, we defined the potential of death induction as follow:

$$P_{death}(t,\tilde{T}) \triangleq \frac{1}{2|S(t)|}\sum_{i=1}^{|S(t)|}\sum_{j=i+1}^{|S(t)|}\frac{\underset{(x,y)\in s_i(t)}{\text{mean}} MC(x,y,t,\tilde{T}) + \underset{(x,y)\in s_j(t)}{\text{mean}} MC(x,y,t,\tilde{T})}{\bar{d}(s_i(t),s_j(t))}, \quad i \neq j \quad (11)$$

where $|S(t)|$ denotes the number of elements in $S$ and $\bar{d}(s_i(t), s_j(t))$ denotes any distance operator between objects $s_i(t)$ and $s_j(t)$, normalized by the maximum dimension of the video frame. In this work, we chose the Euclidean distance between the geometrical center of the two objects, *i.e.*, the average coordinates of their boundary.

### Statistical analysis

Statistical analysis and graphs were made with GraphPad Prism software (v7). Statistical threshold for significance was set for p-values inferior to 0.05 after applying Mann-Whitney-Wilcoxon nonparametric test.

## AUTHOR CONTRIBUTIONS

Conceptualization, IV, AM, JC, HS, GZ, FMG, MCP, EM; Formal Analysis, IV, AM; Funding acquisition, FMG, MCP, EM; Methodology MS, SD; Investigation, IV, AM, VP, MCC; Resources FMC; Software invention and development, AM, EM; Supervision, HS, MCP, EM; Writing – original draft, IV, AM, MCP, EM; Writing—review and editing, IV, AM, VP, MS, MCC, FMC, JC, SD, HS, GZ, FMG, MCP, EM.

## AKNOWLEDGMENTS

We are grateful to Ariel Savina for inspiring discussions at the beginning of the project, and to Elodie Voilin and Jamila Kacher (U1186, IGR) for T-cell clone amplification. This work was supported by Fondation ARC (PGA1 RF20180206991). Irina Veith is supported by a CIFRE fellowship founded in part by National Association for Research and Technology (ANRT) on the behalf of the French Ministry of Higher Education and Research, and in part by Institut Roche.

## REFERENCES

1. Huh D, Kim HJ, Fraser JP, Shea DE, Khan M, Bahinski A, et al. Microfabrication of human organs-on-chips. Nat Protoc. 2013;8: 2135–2157. doi:10.1038/nprot.2013.137

2. van Duinen V, Trietsch SJ, Joore J, Vulto P, Hankemeier T. Microfluidic 3D cell culture: from tools to tissue models. Curr Opin Biotechnol. 2015;35: 118–126. doi:10.1016/j.copbio.2015.05.002

3. Osaki T, Sivathanu V, Kamm RD. Vascularized microfluidic organ-chips for drug screening, disease models and tissue engineering. Curr Opin Biotechnol. 2018;52: 116–123. doi:10.1016/j.copbio.2018.03.011

4. Sung KE, Beebe DJ. Microfluidic 3D models of cancer. Adv Drug Deliv Rev. 2014;79–80: 68–78. doi:10.1016/j.addr.2014.07.002

5. Boussommier-Calleja A, Li R, Chen MB, Wong SC, Kamm RD. Microfluidics: A new tool for modeling cancer-immune interactions. Trends Cancer. 2016;2: 6–19. doi:10.1016/j.trecan.2015.12.003

6. Sontheimer-Phelps A, Hassell BA, Ingber DE. Modelling cancer in microfluidic human organs-on-chips. Nat Rev Cancer. 2019;19: 65–81. doi:10.1038/s41568-018-0104-6

7. Nguyen M, De Ninno A, Mencattini A, Mermet-Meillon F, Fornabaio G, Evans SS, et al. Dissecting Effects of Anti-cancer Drugs and Cancer-Associated Fibroblasts by On-Chip Reconstitution of Immunocompetent Tumor Microenvironments. Cell Rep. 2018;25: 3884-3893.e3. doi:10.1016/j.celrep.2018.12.015

8. Pelon F, Bourachot B, Kieffer Y, Magagna I, Mermet-Meillon F, Bonnet I, et al. Cancer-associated fibroblast heterogeneity in axillary lymph nodes drives metastases in breast cancer through complementary mechanisms. Nat Commun. 2020;11: 404. doi:10.1038/s41467-019-14134-w

9. Mencattini A, Di Giuseppe D, Comes MC, Casti P, Corsi F, Bertani FR, et al. Discovering the hidden messages within cell trajectories using a deep learning approach for in vitro evaluation of cancer drug treatments. Sci Rep. 2020;10: 7653. doi:10.1038/s41598-020-64246-3

10. Crouch SP, Kozlowski R, Slater KJ, Fletcher J. The use of ATP bioluminescence as a measure of cell proliferation and cytotoxicity. J Immunol Methods. 1993;160: 81–88. doi:10.1016/0022-1759(93)90011-u

11. Thorn RM, Palmer JC, Manson LA. A simplified 51Cr-release assay for killer cells. J Immunol Methods. 1974;4: 301–315. doi:10.1016/0022-1759(74)90073-8

12. Forcina GC, Conlon M, Wells A, Cao JY, Dixon SJ. Systematic Quantification of Population Cell Death Kinetics in Mammalian Cells. Cell Syst. 2017;4: 600-610.e6. doi:10.1016/j.cels.2017.05.002

13. Fassy J, Tsalkitzi K, Goncalves-Maia M, Braud VM. A Real-Time Cytotoxicity Assay as an Alternative to the Standard Chromium-51 Release Assay for Measurement of Human NK and T Cell Cytotoxic Activity. Curr Protoc Immunol. 2017;118: 7.42.1-7.42.12. doi:10.1002/cpim.28

14. Park D, Son K, Hwang Y, Ko J, Lee Y, Doh J, et al. High-Throughput Microfluidic 3D Cytotoxicity Assay for Cancer Immunotherapy (CACI-IMPACT Platform). Front Immunol. 2019;10: 1133. doi:10.3389/fimmu.2019.01133

15. Dorothée G, Vergnon I, Menez J, Echchakir H, Grunenwald D, Kubin M, et al. Tumor-infiltrating CD4+ T lymphocytes express APO2 ligand (APO2L)/TRAIL upon specific stimulation with autologous lung carcinoma cells: role of IFN-alpha on APO2L/TRAIL expression and -mediated cytotoxicity. J Immunol Baltim Md 1950. 2002;169: 809–817.

16. Xi K-X, Wen Y-S, Zhu C-M, Yu X-Y, Qin R-Q, Zhang X-W, et al. Tumor-stroma ratio (TSR) in non-small cell lung cancer (NSCLC) patients after lung resection is a prognostic factor for survival. J Thorac Dis. 2017;9: 4017–4026. doi:10.21037/jtd.2017.09.29

17. Su S, Chen J, Yao H, Liu J, Yu S, Lao L, et al. CD10+GPR77+ Cancer-Associated Fibroblasts Promote Cancer Formation and Chemoresistance by Sustaining Cancer Stemness. Cell. 2018;172: 841-856.e16. doi:10.1016/j.cell.2018.01.009

18. Zhang D, Li L, Jiang H, Li Q, Wang-Gillam A, Yu J, et al. Tumor–Stroma IL1β-IRAK4 Feedforward Circuitry Drives Tumor Fibrosis, Chemoresistance, and Poor Prognosis in Pancreatic Cancer. Cancer Res. 2018;78: 1700–1712. doi:10.1158/0008-5472.CAN-17-1366

19. Cho J, Lee H-J, Hwang SJ, Min H-Y, Kang HN, Park A-Y, et al. The interplay between slow-cycling, chemoresistant cancer cells and fibroblasts creates a proinflammatory niche for tumor progression. Cancer Res. 2020 [cited 28 Mar 2020]. doi:10.1158/0008-5472.CAN-19-0631

20. Duluc C, Moatassim-Billah S, Chalabi-Dchar M, Perraud A, Samain R, Breibach F, et al. Pharmacological targeting of the protein synthesis mTOR/4E-BP1 pathway in cancer-associated fibroblasts abrogates pancreatic tumour chemoresistance. EMBO Mol Med. 2015;7: 735–753. doi:10.15252/emmm.201404346

21. Leung CS, Yeung T-L, Yip K-P, Wong K-K, Ho SY, Mangala LS, et al. Cancer-associated fibroblasts regulate endothelial adhesion protein LPP to promote ovarian cancer chemoresistance. J Clin Invest. 128: 589–606. doi:10.1172/JCI95200

22. Ying L, Zhu Z, Xu Z, He T, Li E, Guo Z, et al. Cancer Associated Fibroblast-Derived Hepatocyte Growth Factor Inhibits the Paclitaxel-Induced Apoptosis of Lung Cancer A549 Cells by Up-Regulating the PI3K/Akt and GRP78 Signaling on a Microfluidic Platform. PLOS ONE. 2015;10: e0129593. doi:10.1371/journal.pone.0129593

23. Costa A, Kieffer Y, Scholer-Dahirel A, Pelon F, Bourachot B, Cardon M, et al. Fibroblast Heterogeneity and Immunosuppressive Environment in Human Breast Cancer. Cancer Cell. 2018;33: 463-479.e10. doi:10.1016/j.ccell.2018.01.011

24. Galluzzi L, Vitale I, Aaronson SA, Abrams JM, Adam D, Agostinis P, et al. Molecular mechanisms of cell death: recommendations of the Nomenclature Committee on Cell Death 2018. Cell Death Differ. 2018;25: 486–541. doi:10.1038/s41418-017-0012-4

25. Pilco-Ferreto N, Calaf GM. Influence of doxorubicin on apoptosis and oxidative stress in breast cancer cell lines. Int J Oncol. 2016;49: 753–762. doi:10.3892/ijo.2016.3558

26. Buchholz TA, Davis DW, McConkey DJ, Symmans WF, Valero V, Jhingran A, et al. Chemotherapy-induced apoptosis and Bcl-2 levels correlate with breast cancer response to chemotherapy. Cancer J Sudbury Mass. 2003;9: 33–41. doi:10.1097/00130404-200301000-00007

27. Sangiuliano B, Pérez NM, Moreira DF, Belizário JE. Cell Death-Associated Molecular-Pattern Molecules: Inflammatory Signaling and Control. Mediators Inflamm. 2014;2014. doi:10.1155/2014/821043

28. Elliott MR, Ravichandran KS. The Dynamics of Apoptotic Cell Clearance. Dev Cell. 2016;38: 147–160. doi:10.1016/j.devcel.2016.06.029

29. Medina CB, Mehrotra P, Arandjelovic S, Perry JSA, Guo Y, Morioka S, et al. Metabolites released from apoptotic cells act as tissue messengers. Nature. 2020;580: 130–135. doi:10.1038/s41586-020-2121-3

30. Hartwig T, Montinaro A, von Karstedt S, Sevko A, Surinova S, Chakravarthy A, et al. The TRAIL-Induced Cancer Secretome Promotes a Tumor-Supportive Immune Microenvironment via CCR2. Mol Cell. 2017;65: 730-742.e5. doi:10.1016/j.molcel.2017.01.021

31. Eroglu M, Derry WB. Your neighbours matter - non-autonomous control of apoptosis in development and disease. Cell Death Differ. 2016;23: 1110–1118. doi:10.1038/cdd.2016.41

32. Andreoni A, Colasanti A, Kisslinger A, Mastrocinque M, Riccio P, Roberti G. Fluorometric determination of the kinetics of anthracyclines uptake by cells. J Biochem Biophys Methods. 1994;28: 53–68. doi:10.1016/0165-022x(94)90064-7

33. Mothersill C, Rusin A, Fernandez-Palomo C, Seymour C. History of bystander effects research 1905-present; what is in a name? Int J Radiat Biol. 2018;94: 696–707. doi:10.1080/09553002.2017.1398436

34. Parlato S, De Ninno A, Molfetta R, Toschi E, Salerno D, Mencattini A, et al. 3D Microfluidic model for evaluating immunotherapy efficacy by tracking dendritic cell behaviour toward tumor cells. Sci Rep. 2017;7: 1093. doi:10.1038/s41598-017-01013-x

35. Di Giuseppe D, Corsi F, Mencattini A, Comes MC, Casti P, Di Natale C, et al. Learning Cancer-Related Drug Efficacy Exploiting Consensus in Coordinated Motility Within Cell Clusters. IEEE Trans Biomed Eng. 2019;66: 2882–2888. doi:10.1109/TBME.2019.2897825

36. Gonzales RC, Woods RE. Digital image processing. 2nd edition. Prentice Hall; 2002.

37. Davies ER. Machine Vision: Theory, Algorithms, Practicalities. 3rd Edition. Morgan Kauffman Publishers; 2005.

38. Munkres J. Algorithms for the assignment and transportation problems. J Soc Ind Appl Math. 1957;5: 32–38.

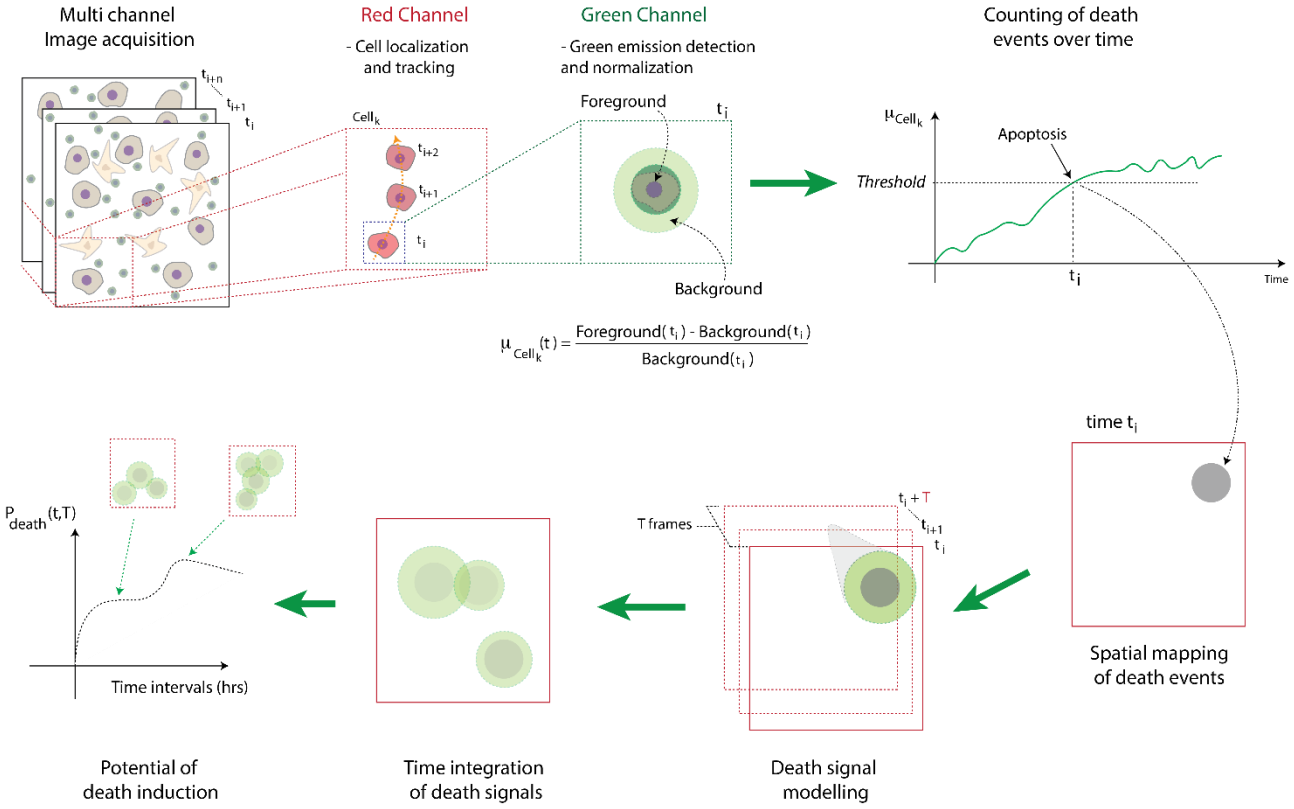


**Figure 1. Description of the STAMP method.**

From multi-channel videos of ToC co-cultures, the cancer cells (pre-stained in red) are localized and tracked in the red channel. The dying cancer cells (becoming green because of the caspase reporter) are identified in the green channel, after signal normalization and thresholding. The method monitors cancer cell deaths both in time and in space. The death signal is modeled to vanish during T time frames. Then, the spatiotemporal features of all death signals are integrated in a unique map, from which a parameter, named potential of death induction ($P_{death}$), is computed over time (see Materials & Methods for details).

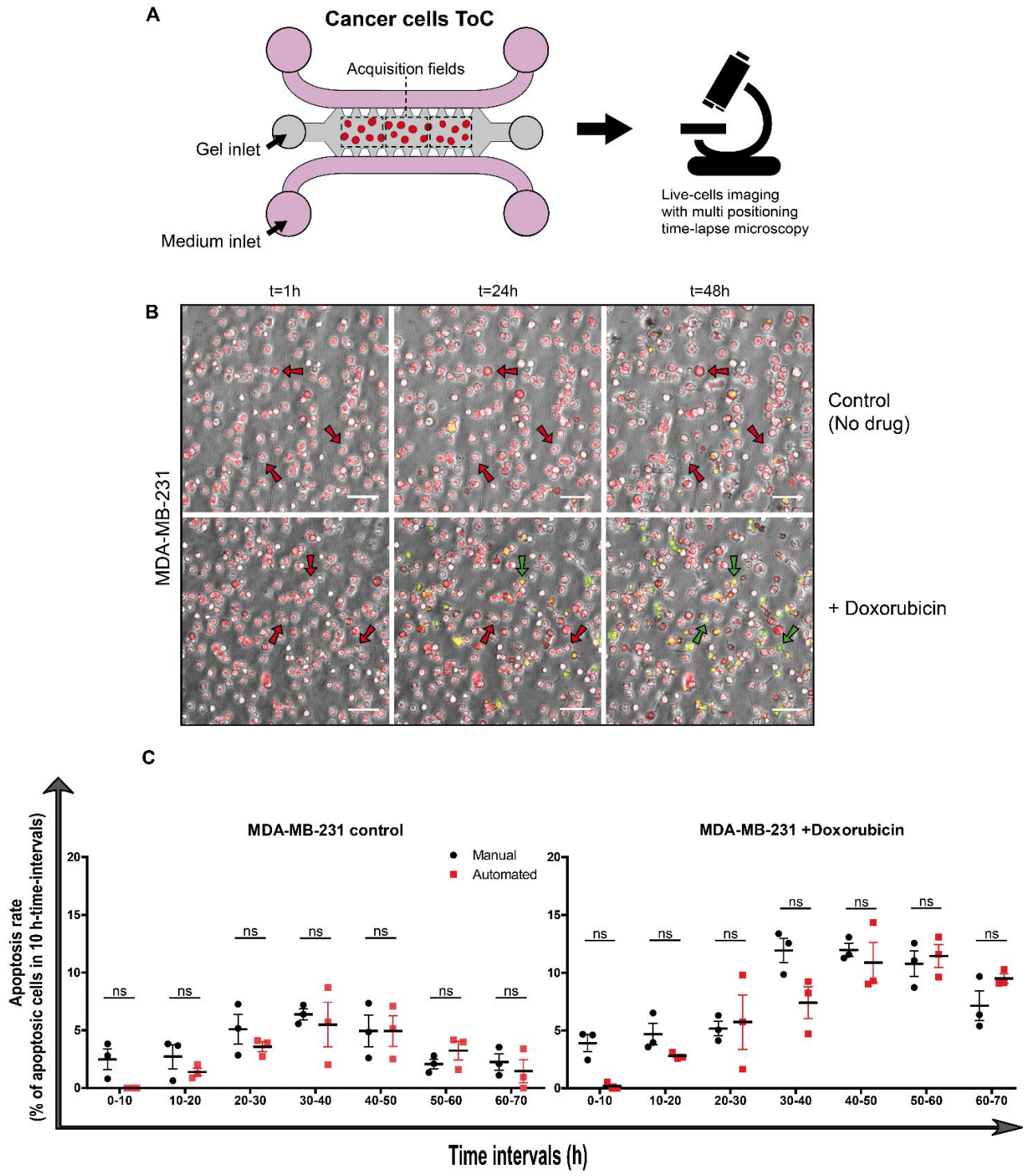


**Figure 2. Chemotherapy-mediated cytotoxicity in breast-cancer-on-chip cultures.**

**A.** Experimental design: breast cancer MDA-MB-231 cells are embedded in a collagen matrix in the central chamber of the chip; cells are live-imaged in transmission channel and fluorescence channels (red and green) every hour for 72 h, without or with doxorubicin (1 µM). **B.** Representative images of MDA-MB-231 cells after 1 h, 24 h and 48 h of culture on-chip, without drug (uppers panels) or with doxorubicin (lowers panels). Red arrows indicate

living cells, whereas green arrows point at apoptotic cells. Scale bar, 100 µm. **C.** Time-course quantifications of the apoptosis rate, calculated in 10 h-time-intervals, showing the comparison between manual counts (red squares) and automatic counts (black rounds, $T_{LAG}$ = 10 h), without (left) or with (right) doxorubicin. Mann-Whitney-Wilcoxon statistical test was used; ns, not significant.

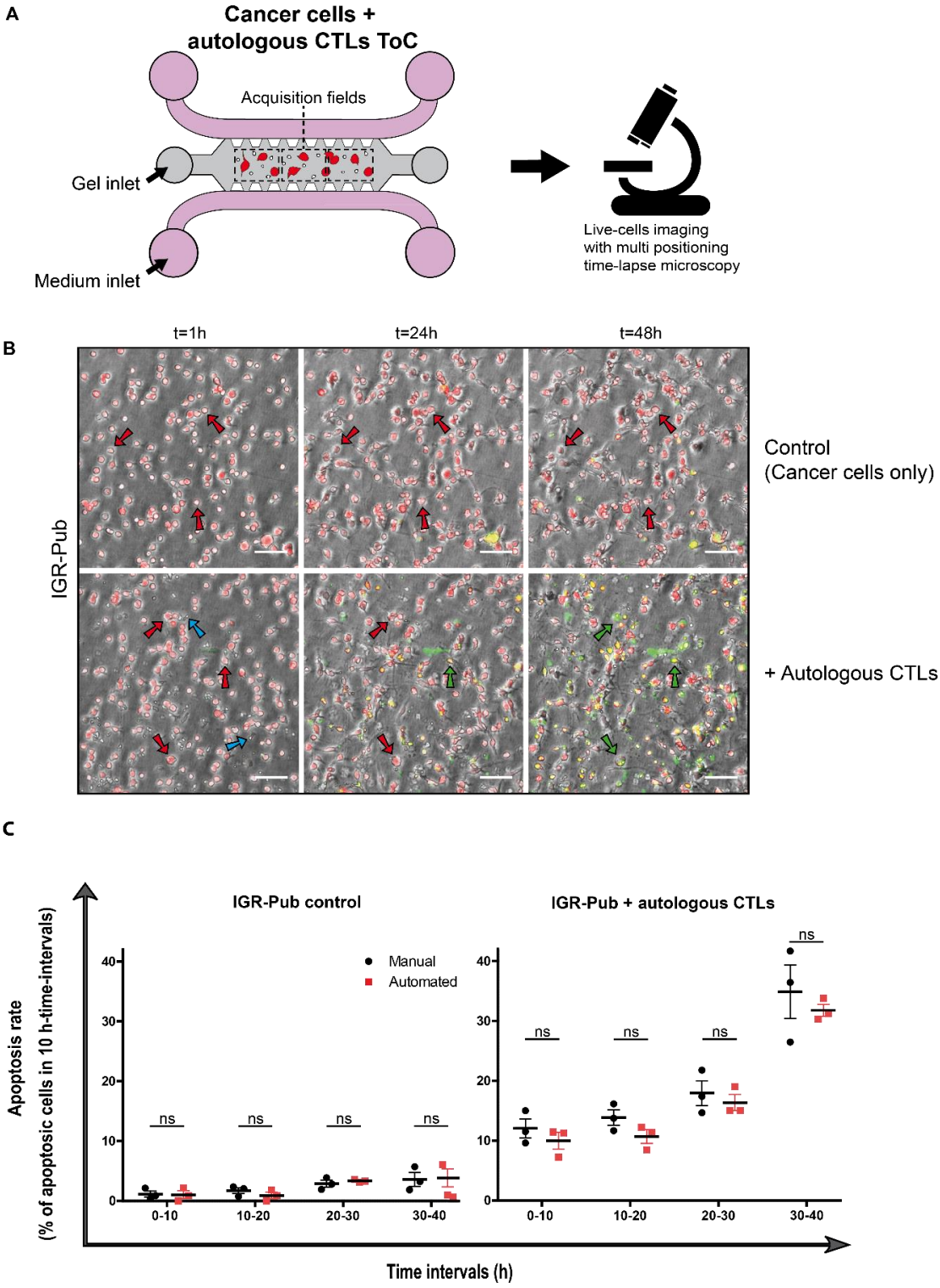

**Figure 3. T-cell mediated cytotoxicity in lung-cancer-on-chip cultures.**

**A.** Experimental design: the lung cancer IGR-Pub cells are embedded in a collagen matrix in the central chamber of the chip, alone or together with autologous CTL (P62 clone) at 1:1 effector to target cell (E:T) ratio; cells are live-imaged in transmission channel and fluorescence channels (red and green) every hour for 48 h. **B.** Representative images of IGR-Pub cells after 1 h, 24 h and 48 h of culture on-chip, alone (uppers panels) or with autologous T cells (lowers panels). Red arrows indicate living cells, whereas green arrows point at apoptotic cells. Scale bar, 100 µm. **C.** Time-course quantifications of the apoptosis rate, calculated in 10 h-time-intervals, showing the comparison between manual counts (red squares) and automatic counts (black rounds, $T_{LAG}$ = 10 h), without (left) or with (right) T cells. Mann-Whitney-Wilcoxon statistical test was used; ns, not significant.

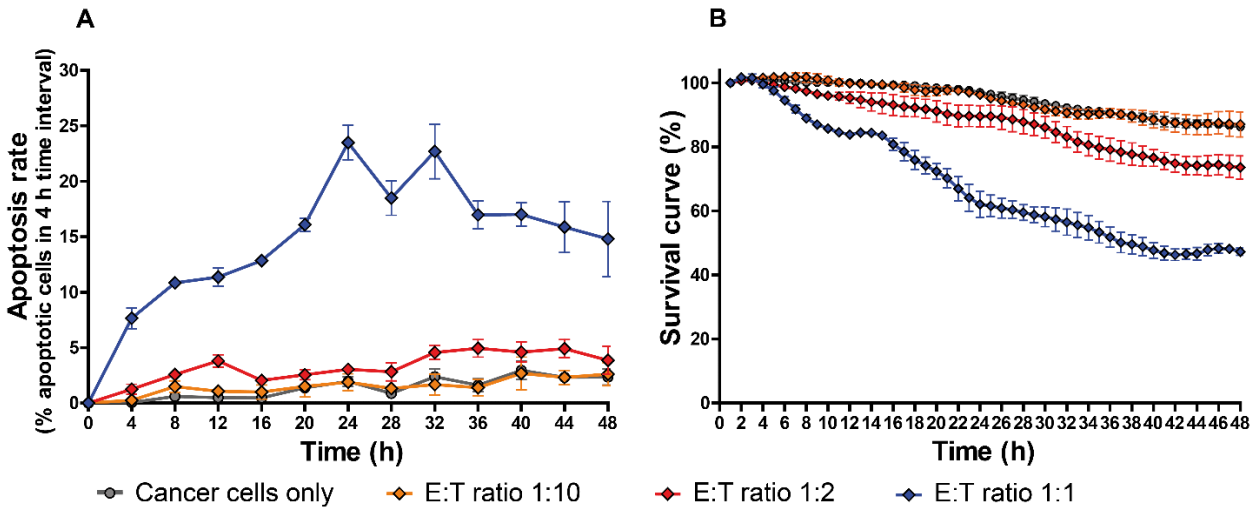


**Figure 4. Real-time dependency of T-cell mediated cytotoxicity on T cell density.**

IGR-Pub lung cancer cells were co-cultured on-chip with autologous T cells at indicated E:T ratios. **A.** Time-course quantifications of the apoptosis rate, calculated in 4 h-time-intervals ($T_{LAG}$ = 4 h), for a total duration of 48 h. **B.** Survival curves of cancer cells within the ToC at 1-hr time resolution. For each $t_i$ the % of surviving cells, calculated with respect to the initial number of living cells, is the average of 3 hours, centered on $t_i$, to smoothen the fluctuations. The graphs show the mean of 3 measurements coming from 3 videos of the same experiment (+/- SEM).

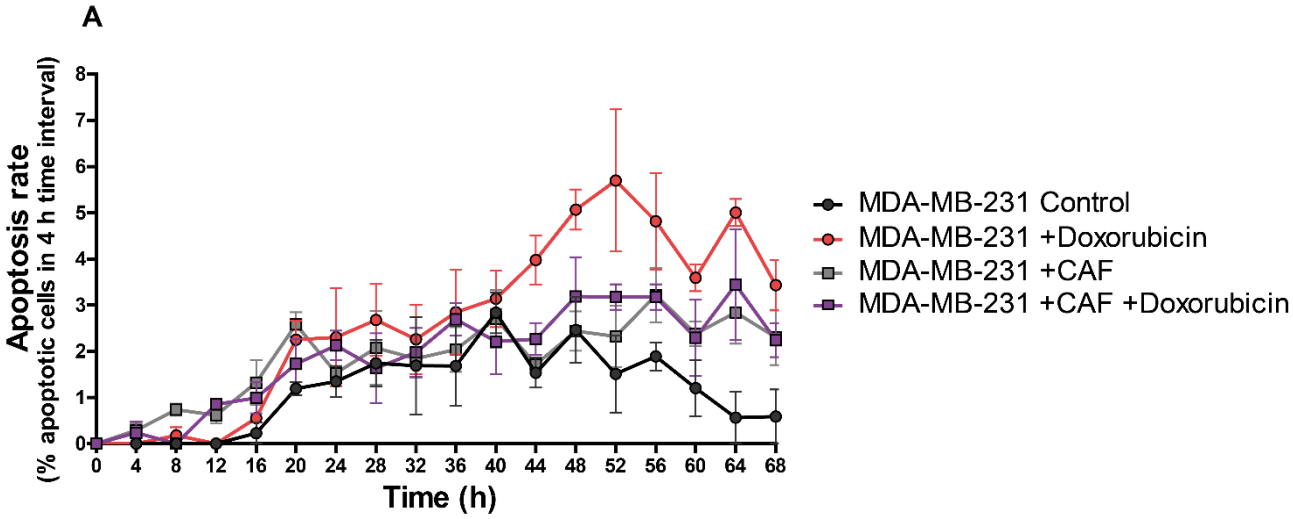


**Figure 5. Cancer-associated fibroblasts promote chemo-resistance in breast-cancer-on-chip.** MDA-MB-231 cancer cells were co-cultured on-chip +/- cancer-associated fibroblasts (CAFs) and +/- doxorubicin (1µM) treatment. Final CAF:cancer ratio was 1:6. The graph shows the time-course quantifications of the apoptosis rate, calculated in 4 h-time-intervals ($T_{LAG}$ = 4 h), for a total duration of 68 h. The data are the means of 3 measurements coming from 3 videos of the same experiment (+/- SEM). The data illustrating the MDA-MB-231 without CAF conditions come from the same videos analyzed for Figure 2 but with different time-interval resolution.

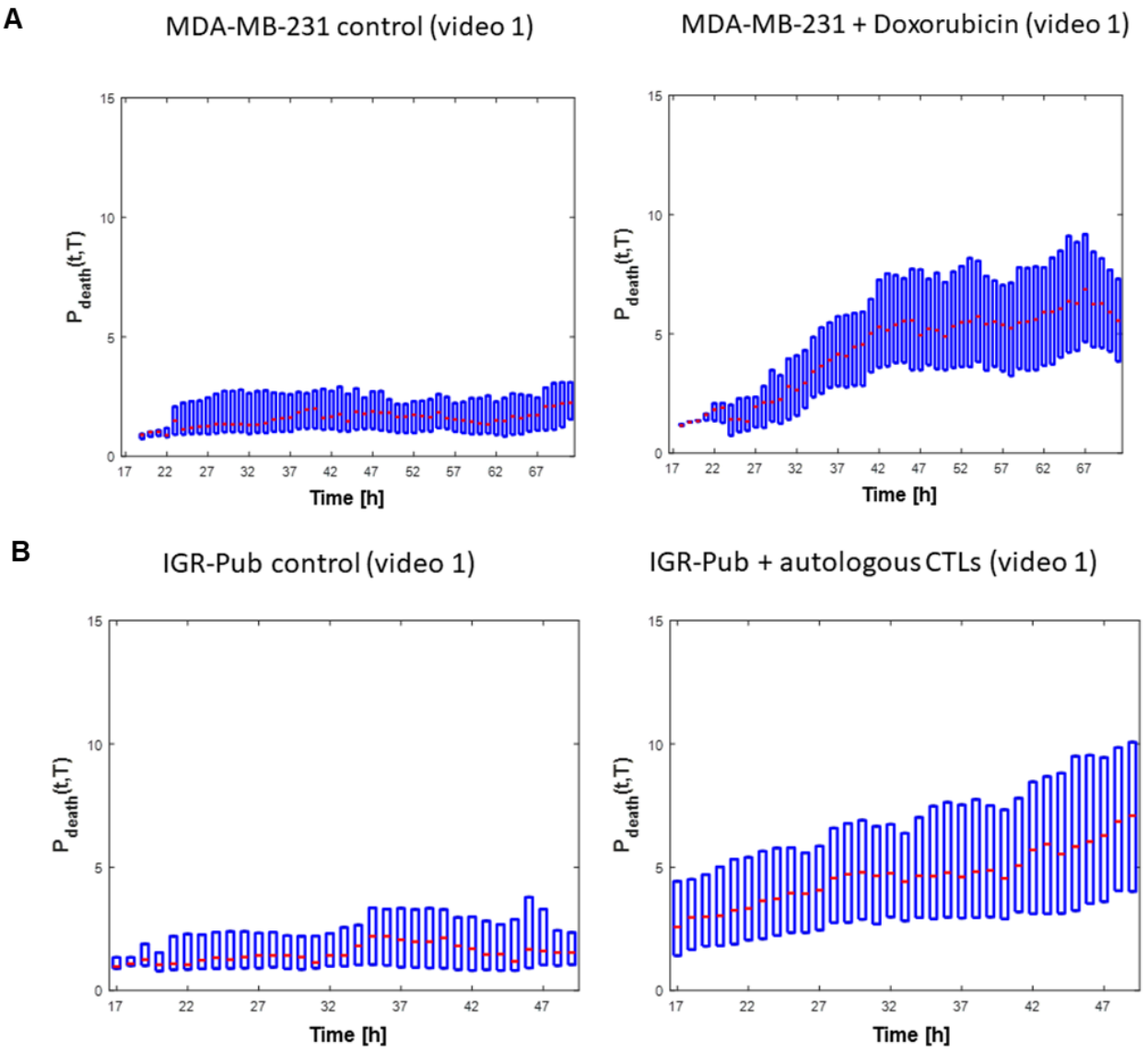


**Figure 6. The Potential of death induction ($P_{death}$) of cancer cells increases over time upon cytotoxic death, but not upon natural death.**

**A.** Representative $P_{death}$ analysis on one video of breast cancer MDA-MB-231 cells cultured within ToC without (left, natural death) or with 1 µM doxorubicin (right, cytotoxic death). More video analyses are shown in Supplementary Figure 2. **B.** Representative $P_{death}$ analysis on one video of NSCLC IGR-Pub cells cultured within ToC alone (left, natural death) or together with autologous CTL (P62 clone) (right, cytotoxic death). More video analyses are shown in Supplementary Figure 2.

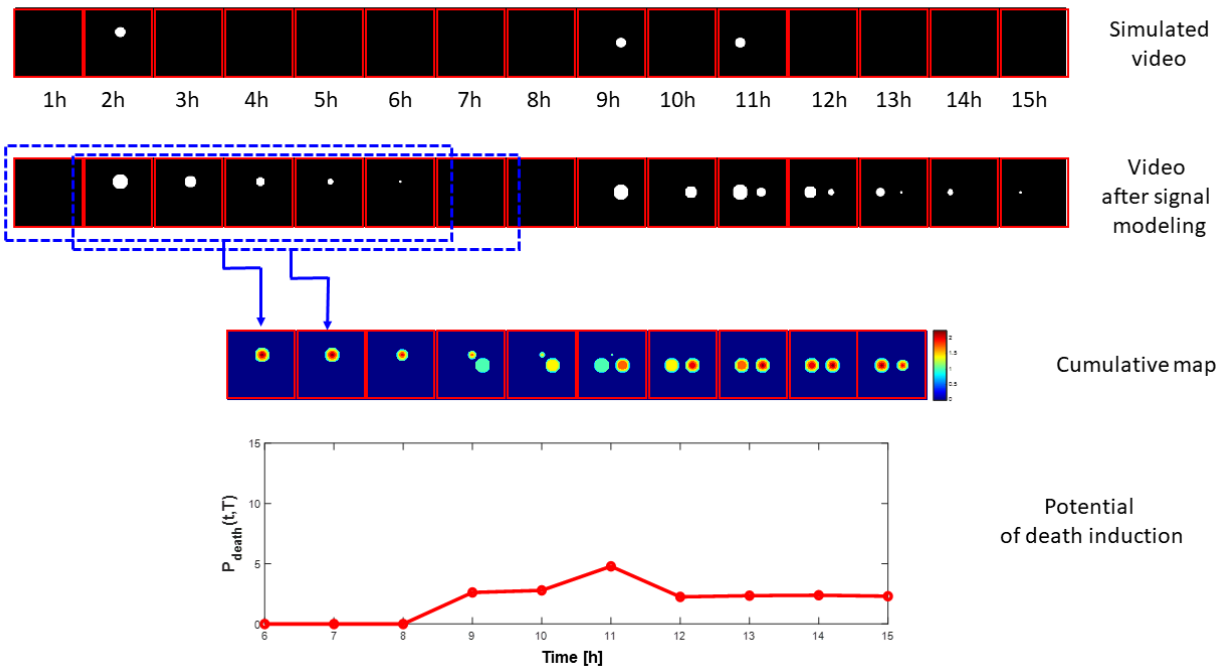


**Supplementary Figure 1. Simulated example for the calculation of the Potential of death induction ($P_{death}$).**

Three simulated deaths occur at 2 h, 9 h, and 11 h (first video sequence). The death signals are modeled by the construction of a signal wake (second video sequence), the duration of which depends on the dimension of the original death region (first video sequence). Then, a cumulative map $MC(x, y, t, \tilde{T})$ is constructed by combining both spatial and temporal death influence (third video sequence) using $\tilde{T} = 6$. Finally, $P_{death}$ is computed over time for the entire image area (bottom graph). Until t = 8 h, there is only one death, so there is no induction phenomenon. An additional death occurs at t = 9 h thus producing an induction phenomenon and an increase in potential. A third death occurs at t = 11 h thus producing a further increase in the potential value. Potential is also influenced by the absolute value of the map *MC* and by the distances of the different zones of death. From t = 12 h there is no more memory of the first death, hence only the last two death zones remain whose distance is larger than that of the two death zones involved in t = 9 h and 11 h, thus causing a decrease in potential.

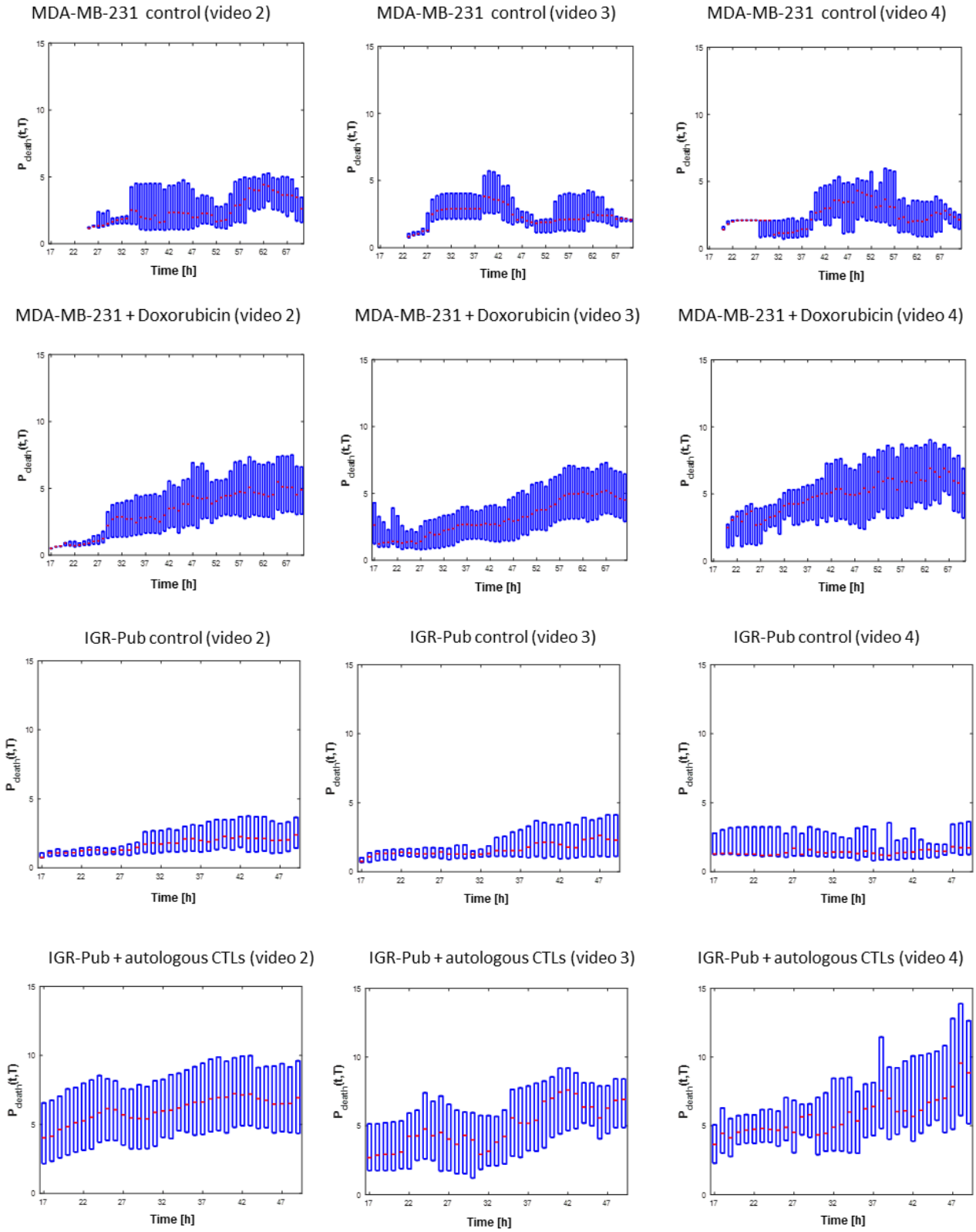


**Supplementary Figure 2. Addition $P_{death}$ analyses supporting Figure 6.**

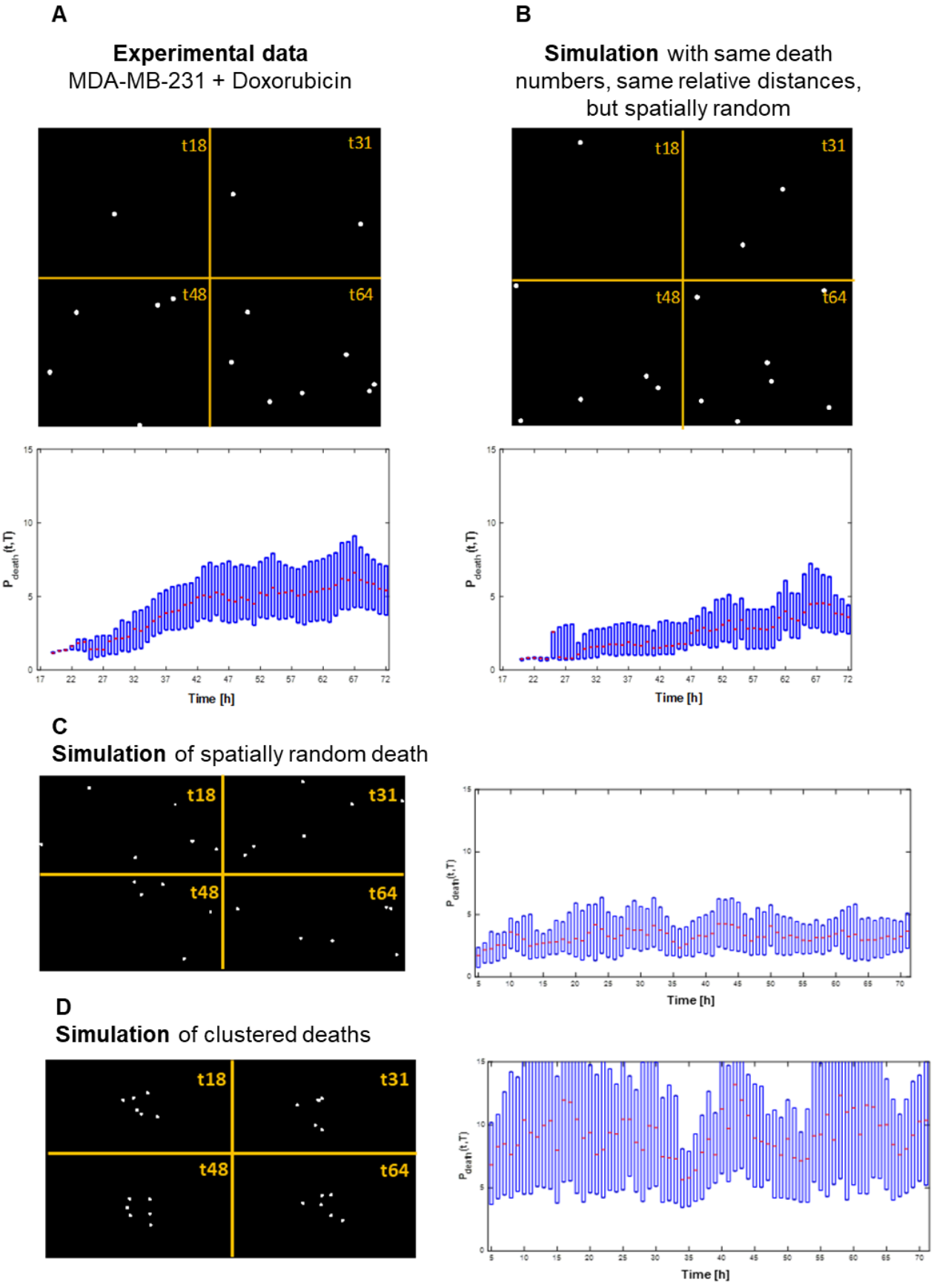


**Supplementary Figure 3. Simulations showing the dependency of the Potential of death induction ($P_{death}$) on temporal and spatial features.**

**Université Paris-Saclay**
Espace Technologique / Immeuble Discovery
Route de l'Orme aux Merisiers RD 128 / 91190 Saint-Aubin, France

**A.** Experimental data showing the spatial localization of death events at different time points (above), and the corresponding $P_{death}$ measurements (below) on a video of MDA-MB-231 cells treated with 1 μM doxorubicin (the same reported in Figure 6A).

**B.** Simulation of a video with the same death events as in A, but with a spatially random distribution, maintaining approximatively the relative object distances. Note that the corresponding $P_{death}$ measurements are increasing much less than in A, indicating that the $P_{death}$ increase does not simply result from the increase of death numbers over time, but it depends also on death positions.

**C.** Simulation of a video with a constant number of death events with a spatially random distribution. Note that the corresponding $P_{death}$ measurements are constant over time.

**D.** Simulation of a video with a constant number of death events with a clustered distribution. Note that the corresponding $P_{death}$ measurements are constant over time, but higher than in C.

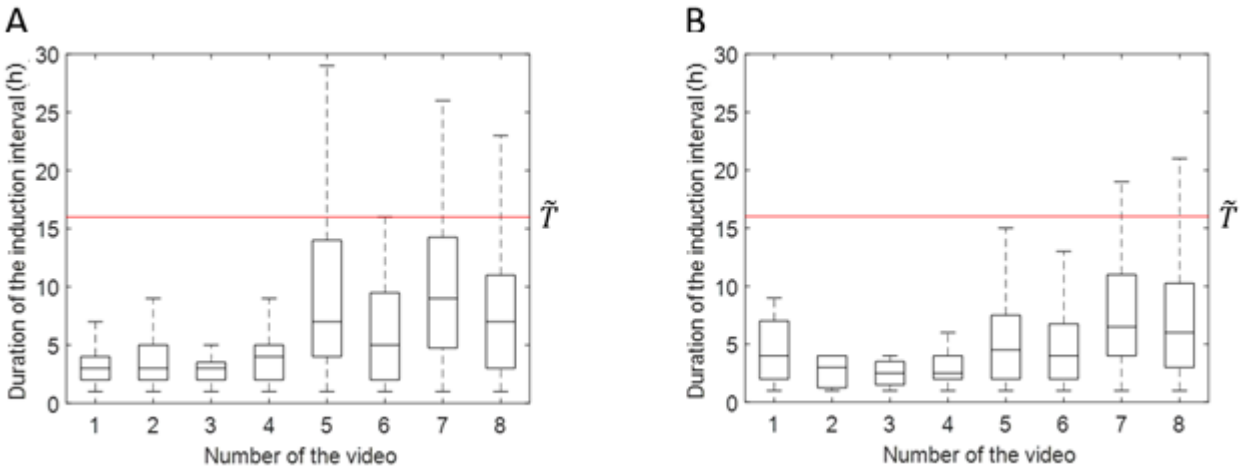


**Supplementary Figure 4. Rationale for the calculation of the optimal $\tilde{T}$.**

$\tilde{T}$ is the time window over which the aggregation of deaths and their wake were computed by means of the definition of the cumulative map *MC* (Eq. (9)). The induction intervals, defined as the duration of the chain of death, were computed for each cell, from 16 videos from 2 experiments, one experiment with the lung cancer cell line IGR-Pub (A) and one experiment with the breast cancer cell line MDA-MB-231 (B). The distributions of induction show that vast majority of induction intervals is below 16 h, meaning that $\tilde{T} = 16$ h is an optimal choice.

**Supplementary Videos**

Video 1. Breast cancer MDA-MB-231 cells alone.

http://xfer.curie.fr/get/QrlOJaBA5z3/Video%201.%20Breast%20cancer%20MDA-MB-231%20cells%20alone.avi

Video 2. Breast cancer MDA-MB-231 cells with doxorubicin.

http://xfer.curie.fr/get/ZolmZMVqkaD/Video%202.%20Breast%20cancer%20MDA-MB-231%20cells%20with%20doxorubicin.avi

Video 3. Lung cancer IGR-Pub cells alone.

http://xfer.curie.fr/get/QFLNUPscZOT/Video%203.%20Lung%20cancer%20IGR-Pub%20cells%20alone.avi

Video 4. Lung cancer IGR-Pub cells with autologous T cells (ratio 1:1).

http://xfer.curie.fr/get/aXvtBG0NOWz/Video%204.%20Lung%20cancer%20IGR-Pub%20cells%20with%20autologous%20T%20cells%20%28ratio%201%20to1%29.avi

Video 5. Breast cancer MDA-MB-231 cells with CAF.

http://xfer.curie.fr/get/sOFfNj3mUPT/Video%205.%20Breast%20cancer%20MDA-MB-231%20cells%20with%20CAFs.avi

Video 6. Breast cancer MDA-MB-231 cells with CAF with doxorubicin.

http://xfer.curie.fr/get/xOrBEAy40uB/Video%206.%20Breast%20cancer%20MDA-MB-231%20cells%20with%20CAFs%20with%20doxorubicin.avi

Video 7. Representative STAMP output video.

http://xfer.curie.fr/get/guuGaX3OBP0/Video%207.%20Representative%20MAPoptosis%20output%20video.avi

## 4.3 Characterization of the lung cancer cell model

In this project, we exploited an autologous cellular model of lung cancer and tumour-infiltrated lymphocytes (TILs). Thanks to the collaboration with Fathia Mami-Chouaib in Institut Gustave Roussy, we were able to exploit two cancer cell lines, isolated from patient Heu, presenting large cell carcinoma and patient Pub, who had lung adenocarcinoma. For each patient, about 20 years ago, the lab of Fathia Mami-Chouaib isolated, amplified and froze the immortalized cancer cells and the autologousTILs. For the experiments of this thesis, with the help of our collaborators, we further amplified the TILs by the "Feeder" co-culture [205]. The procedure consists in culturing the T cells in presence of irradiated autologous cancer cells and irradiated Laz509 (B lymphoma cell line) for 14 days. The irradiation prevents the proliferation of cancer cells, ensuring their killing by T cells and the maintenance of the exposure of epitopes at cell surface. After this time, the CTLs specific for the autologous cells are amplified and ready to be used for experiments. This way, we could access to either the polyclonal population of TILs $CD8^+$, which we will refer from now on as "bulk"; or specific cytotoxic T cell clones, who are reactive against a specific cancer cell epitope. Our collaborators managed to isolate different pairs of cytotoxic T cell clones associated to IGR-Heu or IGR-Pub.

### 4.3.1 Characterization of IGR-Heu and IGR-Pub lung cancer cell lines

First, we performed some preliminary analysis to better characterize our lung cancer model. We determined by flow cytometry the expression of PD-L1, MHC-I and MHC-II on the IGR-Heu and IGR-Pub cancer cells as shown in Figure 8a and b, respectively. In both cell lines at least 40% of the cells were positive for PD-L1. Both cell lines did not show downregulation

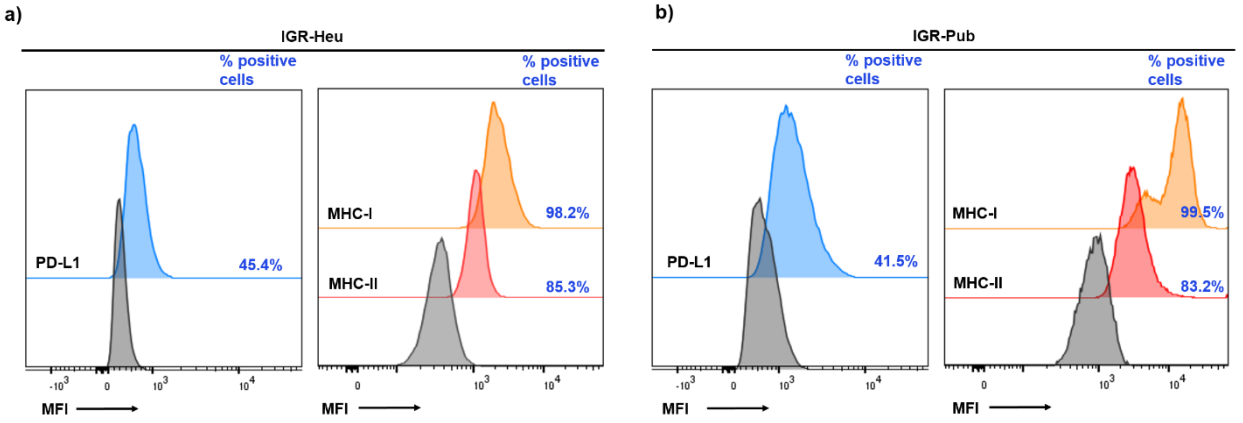


c)

| Gene | Chr | cDNA change | AA change | Coverage | Frequence (%) |
|---|---|---|---|---|---|
| *TP53* | 17 | c.396G>T | p.(Lys132Asn) | 1406 | 99,9 |
| *TP53* | 17 | c.396G>T | p.(Lys132Asn) | 8658 | 99,8 |
| *CTNNB1* | 3 | c.110C>T | p.(Ser37Phe) | 11948 | 48,3 |
| *CTNNB1* | 3 | c.110C>T | p.(Ser37Phe) | 1160 | 45,0 |
| *STK11* | 19 | c.375-10A>G | p.? | 1894 | 99,8 |
| *STK11* | 19 | c.375-10A>G | p.? | 1206 | 100 |

d)

| Gene | Chr | cDNA change | AA change | Coverage | Frequence (%) |
|---|---|---|---|---|---|
| *TP53* | 17 | c.916C>T | p.(Arg306*) | 3039 | 100 |
| *TP53* | 17 | c.916C>T | p.(Arg306*) | 1292 | 100 |
| *KRAS* | 12 | c.34G>A | p.(Gly12Ser) | 2043 | 69,9 |
| *KRAS* | 12 | c.34G>A | p.(Gly12Ser) | 1414 | 70,9 |
| *FGFR1* | 8 | c.1680C>G | p.(Ile560Met) | 427 | 51,3 |
| *FGFR1* | 8 | c.1680C>G | p.(Ile560Met) | 671 | 45,9 |

*Figure 8 Cancer cell model characterization*

*a) Characterization by flow cytometry of the expression of PD-L1, MHC-I and MHC-II in IGR-Heu LCC cells and b) IGR-Pub adenocarcinoma cells. c) Genomic profiling of IGR-Heu cancer cells. d) Genomic profiling of IGR-Pub cancer cells.*

of the MHC-I (almost 100% cells were MHC-I positive) and the majority (> 80%) were expressing MHC-II (HLA-DR).

Lung cancer is a genetically heterogeneous disease and the presence of certain molecular alterations can influence the response to treatment. In order to know the precise genetic background of the IGR-Heu and the IGR-Pub, we extracted the DNA from each cell line and we performed a genetic profiling. Thanks to the help of the genomic platform of Institut Curie, we were able to sequence the DNA extracted from each cell line and to check a panel of 78 frequent mutations routinely tested in clinics.

As illustrated in Figure 8c, IGR-Heu harbor single-nucleotide alterations in TP53 (coding for the tumor suppressor protein p53), CTNNB1 (beta-catenin, a protein involved in coordination of cell-cell adhesion and gene transcription) and STK11 (Serine/threonine kinase 11) genes. Moreover, the analysis of copy number variations indicated that in IGR-Heu cancer cells, the CDKN2A gene (coding for the cyclin-dependent kinase inhibitor 2A, a tumor suppressor) is homozygous deleted (data not shown). The same analysis was performed on the IGR-Pub cancer cells in Figure 8d, where single-nucleotide alterations were detected in TP53, KRAS (small GTPase K-Ras) and FGFR1 (Fibroblast growth factor receptor 1, a receptor tyrosine kinase) genes. In the IGR-Pub no homozygous deletions nor amplifications were identified.

In conclusion, the expression profile of MHC and PD-L1 molecules and the genomic alterations of IGR-Heu LCC and IGR-Pub adenocarcinoma cells confirm that our lung cancer cellular models have molecular properties which are highly consistent with those observed in clinics. Studies report that a big proportion of lung cancer samples express MHC-I (60-70% in NSCLC patients) [206], MHC-II (33% in NSCLC patients) [207], and PD-L1 (43% in NSCLC, using a cutoff of ≥5% positive tumor cells) [208].

Moreover, mutations in TP53, KRAS, STK11, CDKN2A, and FGFR1 genes are in the list of the most frequently mutated genes in lung cancers (Table1), and our cellular models well recapitulate the typical genetic alterations of the corresponding histological types.

### 4.3.2 Characterization of autologous cytotoxic TILs

Next, we characterized by flow cytometry the expression of several T cell markers on the TILs coming from patient Heu and Pub. In Figure 9a are listed the activation markers, inhibitory immune checkpoints and co-stimulatory immune checkpoints, with their respective ligands, that we chose for the immune profiling. More in detail, we used CD69 and CD25 (IL-2Rα) as early activation markers, since they are widely validated by the literature.

a)

| *T cell marker description* | *T cell marker* | *Ligand(s)* |
|---|---|---|
| Activation marker | CD69 | S1P, Galectin-1 |
| Activation marker | CD25, IL2 receptor alpha | IL-2 soluble |
| Inhibitory immune checkpoint | PD-1, Programmed cell death protein 1 (CD279) | PD-L1, PD-L2 |
| Inhibitory immune checkpoint | TIM-3, T-cell immunoglobulin and mucin-domain containing-3 | Galectin 9, CEACAM1 |
| Inhibitory immune checkpoint | TIGIT, T cell immunoreceptor with Ig and ITIM domains | CD155 (PVR), CD112 (PVRL2) |
| Inhibitory immune checkpoint | LAG-3, Lymphocyte-activation gene 3 (CD223) | MHC-II, FGL1 |
| Inhibitory immune checkpoint | CTLA-4, Cytotoxic T-lymphocyte-associated protein 4 (CD152) | CD80, CD86 |
| Inhibitory immune checkpoint | CD244 (2B4) | CD48 |
| Co-stimulatory immune checkpoint | OX-40 (CD134, TNFRSF4) | OX-40L |
| Co-stimulatory immune checkpoint | CD137 (4-1BB, TNFRSF9) | CD137L |
| Co-stimulatory immune checkpoint | GITR (CD357) | GITRL |

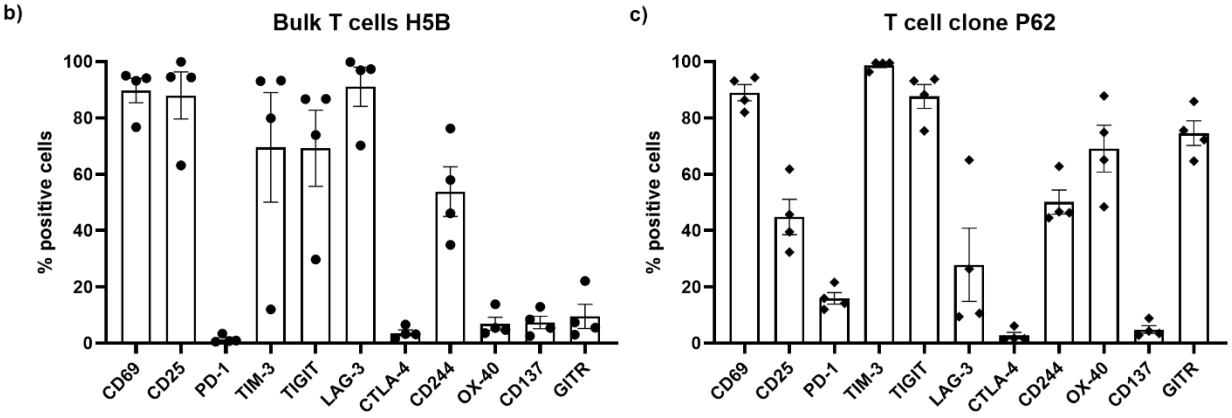


*Figure 9 T cells phenotyping of activation and exhaustion statuses*

*a) Descriptive table of the markers chosen for T cells phenotyping panel and their associated ligands. b) Flow cytometry phenotyping of the bulk T cells H5B assessed by the % of positivity for each marker; graphs show the mean ±SEM from 4 independent experiments. c) Flow cytometry phenotyping of the T cell clone P62 assessed by the % of positivity for each marker; graphs show the mean ±SEM from 4 independent experiments.*

Concerning the immune checkpoints, we selected those that are currently targetable by immunotherapies used in clinics or by new antibodies undergoing clinical trials, with the final aim to assess in ToC the efficacy of combined therapy strategies.

Figure 9b shows the % of positive cells per each marker for the bulk of $CD8^+$ T cells H5B, isolated from patient Heu. In Figure 9c is represented the % of positive cells per each marker for the $CD4^+$ T cell clone P62, isolated from patient Pub.

Both T cells types express high levels of CD69. Previous publications including the T cell clone P62 indicate that these cells are $CD3^+$ $CD4^+$ and $CD103^-$ [209], $TCR\alpha\beta^+$, $CD28^-$, $CCR7^-$, $CD45RA^-$, $CD45RO^+$ [210] suggesting that those are effector memory T cells.

Moreover, the expression of PD-1 is low in both H5B and P62 T cells, whereas TIM-3 and TIGIT are highly expressed by both of them. We observed a differential expression of LAG-3, which is high in H5B bulk T cells and low in the P62 T cell clone, and of OX-40 which is inversely high in P62 and low in H5B. This phenotyping of the autologous TILs gave us the baseline expression of different T cell markers, when the T cells are cultured in dish. H5B are $CD8^+$ clones sorted from patient Heu's TILs. Interestingly, P62 are a T $CD4^+$ clone shown to exert its cytotoxic activity through the interaction of TRAIL/APO2 ligand with TRAIL receptor on cancer cells [210].

### 4.3.3 Characterization of primary lung fibroblasts

Finally, we characterized two primary heterologous human lung fibroblast models that are commercially available: normal human lung fibroblasts (NHLF), purchased by Lonza, and CAF07-AD, isolated from lung adenocarcinoma and purchased by Neuromics. It is well known that "normal" fibroblasts modify their identity when they are cultured in 2D dish because of the rigidity of the plastic substrate and that they acquire some features of the activated cancer-associated fibroblasts [211], [212]. Keeping in mind this limitation, we analysed these two fibroblast models for the expression of several fibroblast markers previously used in the laboratory to characterize CAF identity and heterogeneity [44]–[47].

In Figure 10a the markers used for the characterization are listed along with their respective genes.

We performed the flow cytometry characterization on the two primary human lung fibroblasts, "normal" NHLF and cancer-associated CAF07-AD. We analyzed both the expression

level of the markers (MFI, Mean Fluorescence intensity) (Figure 10b) and the % of positive cells (Figure 10c) (see Materials and Methods)

The analysis reveals that both NHLF and CAF07-AD highly express CD29 and FAP, therefore showing a myofibroblastic CAF-S1 profile (see Introduction The cancer-associated fibroblasts (CAFs)1.1.4.iii). Moreover, the two cell types express other markers used to identify CAF-S1 subset, such as α-SMA, FSP1 and PDGFRβ. Very likely, even though NHLF were isolated from a healthy donor, the stiffness of the dish triggered fibroblast activation. In fact, the fibroblasts show a markedly plasticity and the non-activated subsets S2 and S3 were only observed in fresh tumor biopsies, never after spreading on dish from tumor pieces. In conclusion, the CAF07-AD cells can be used in ToC co-culture experiments as heterologous model for lung CAF (specifically CAF-S1 subtype), however there is no a good control so far for normal fibroblasts.

a)

| Gene | CAF marker |
|---|---|
| *ITGB1* | CD29, integrin subunit beta 1 |
| *FAP* | FAP, fibroblast activation protein alpha |
| *ACTA2* | α-SMA, alpha smooth muscle actin |
| *S100A4* | FSP1, fibroblast-specific protein 1 |
| *PDGFRB* | PDGFR-β, platelet-derived growth factor receptor beta |
| *PDPN* | PDPN, podoplanin |
| *MCAM* | MCAM, melanoma cell adhesion molecule |
| *DPP4* | DPP4, dipeptidyl peptidase |

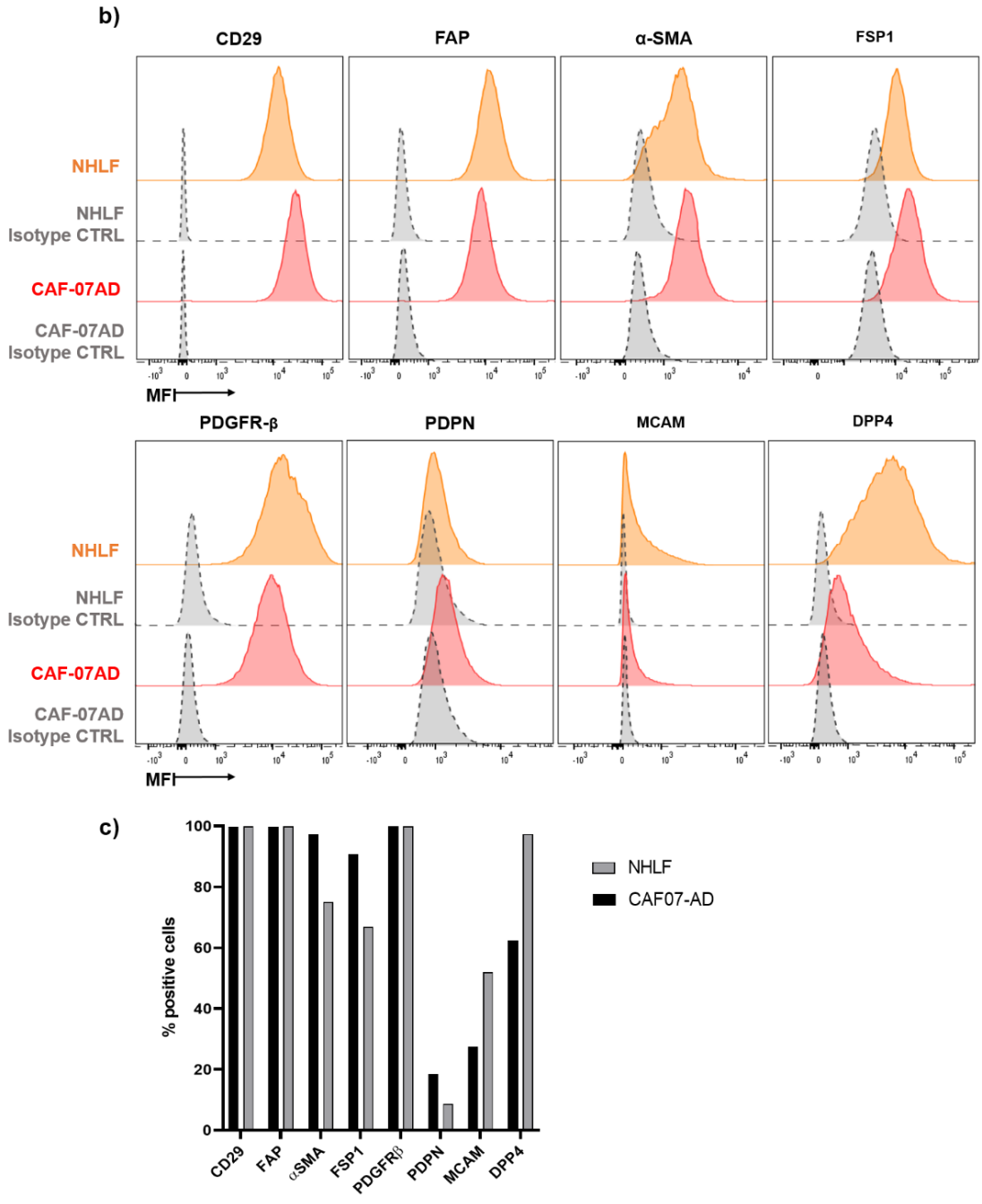


*Figure 10 Fibroblast characterization*

*a) Table describing the markers used for fibroblast characterization. b) Expression of fibroblast markers quantified by MFI (Mean Fluorescence intensity) in NHLF and CAF07-AD*

*cells. c) Quantification of the % of positivity for fibroblast markers in NHLF and CAFO7-AD cells; n=1 experiment*

## 4.4 T cells plasticity after co-cultures on-chip in presence of immunotherapy

We asked the question whether the reconstituted TME on-chip may activate T cells and/or modulate the expression of immune checkpoints in presence or absence of ICI, by analyzing by flow cytometry the T cell markers (listed in Figure 9a) after the ToC co-cultures.

The experiment workflow, illustrated in Figure 11a, consists in culturing on-chip T cells with or without the autologous cancer cells, in presence or absence of anti-PD-1 (Nivolumab, 10 µg/ml). The ToCs are kept in humidified chambers in the incubator for 3 days. After that time, the cells are harvested from the gel by collagenase digestion, stained with the mix of antibodies for T cell markers and analyzed at a ZE5 Biorad flow cytometer (see Materials and Methods).

The 3.41 $mm^3$ chamber of the microfluidic device contain approximatively 20 thousands T cells; the recovery after collagenase digestion is about 5% of cells (after gating); few thousands cells is the minimal number of cells for accurate flow cytometer measurements; consequently, for each condition, the cells from 4 identical chips (equal to12 gel chambers) were pooled before the flow cytometer analysis.

Figure 11b shows the gating strategy for a representative experiment of T cells plasticity analysis. First, we select the population of interest containing T cells, then we gate on viable cells (negative for NIR viable staining), we exclude doublets and lastly we gate on the $CD4^+$/$CD8^+$ T cells. In order to fit the panel for P62 ($CD4^+$) and H5B ($CD8^+$) cell types, we used either an anti-CD4 or anti-CD8 antibody, which are coupled with the same fluorochrome.

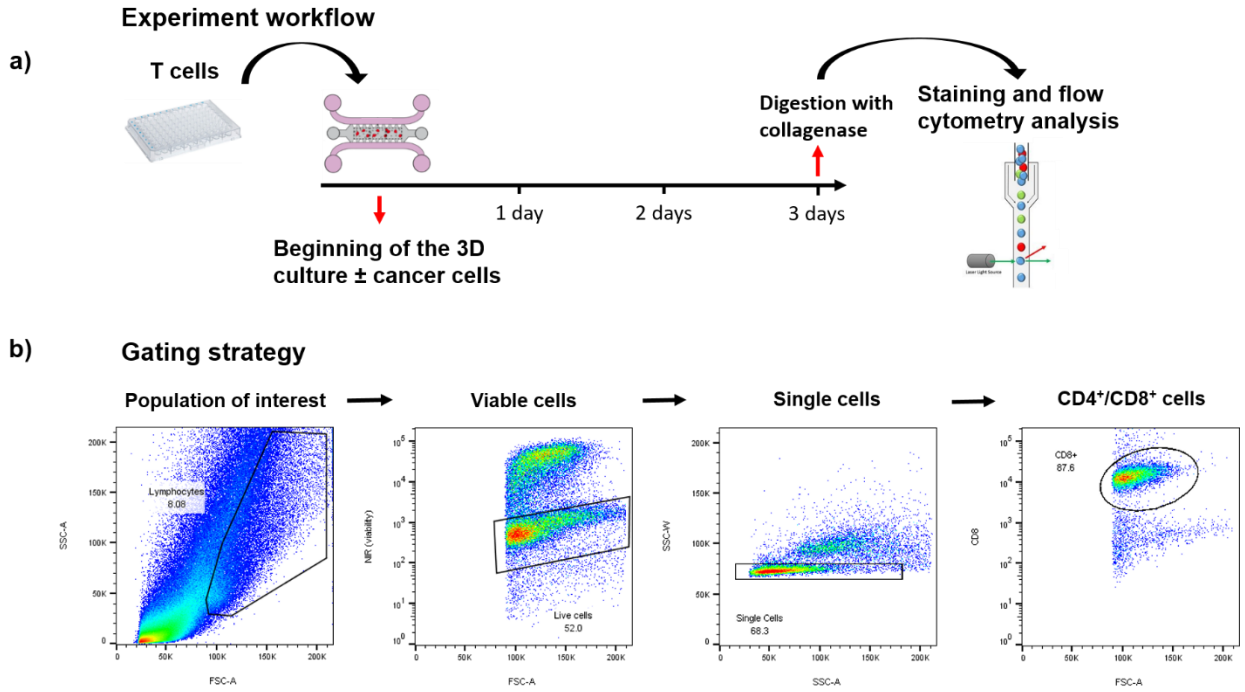


*Figure 11 Experiment workflow and gating strategy to analyse T cell plasticity by flow cytometry after ToC co-cultures*

*a) Experiment workflow: T cells are seeded in the microfluidic devices either alone or in co-culture with the autologous cancer cells; after three days of 3D culture, gel is digested with collagenase and the cells are harvested, stained with the panel of T cell markers and analysed by flow cytometry. b) Gating strategy steps: selection of the population of interest, selection of viable cells by the negativity of NIR staining, exclusion of doublets and selection of CD4+ or CD8+ cells. This way we are able to exclude the non-T cells from the analysis. SSC-A and FSC-A refer to the area of the side scatter and forward scatter distribution.*

### 4.4.1 Impact of 3D chip setting on T cell markers

First, we checked whether the 3D culture on-chip, compared to the 2D culture in dish, could have an impact on T cells. To do so, we compared the T cell markers, in H5B bulk and in P62 T cells, when cultured alone in dish or alone in chip (therefore embedded in the collagen gel).

Figure 12 shows the quantifications of the 11 makers analyzed by flow cytometry on H5B (Figure 12a) and on P62 (Figure 12b) T cells, respectively. In both cases, the left graph represents the % of cells positive for the marker and the right graph shows the quantification of the specific MFI (speMFI, calculated as the ratio between the median of the antibody mean

fluorescence intensity and its isotype control). The latter is an indicator proportional to the expression of the given marker by each cell.

The analysis showed that the 3D culture in chip does not activate the T cells and poorly modulates the expression of immune checkpoints. Notably, the only marker that significantly increased upon culture on-chip for both cell types were PD-1 and OX-40 (limitedly to the MFI), while LAG-3 increased exclusively for the T cell clone P62. We can conclude that the 3D culture has a negligible impact on the expression of T cell markers. Therefore, in the following experiments we will consider the T cells alone in the gel as a control condition.

in presence of immunotherapy

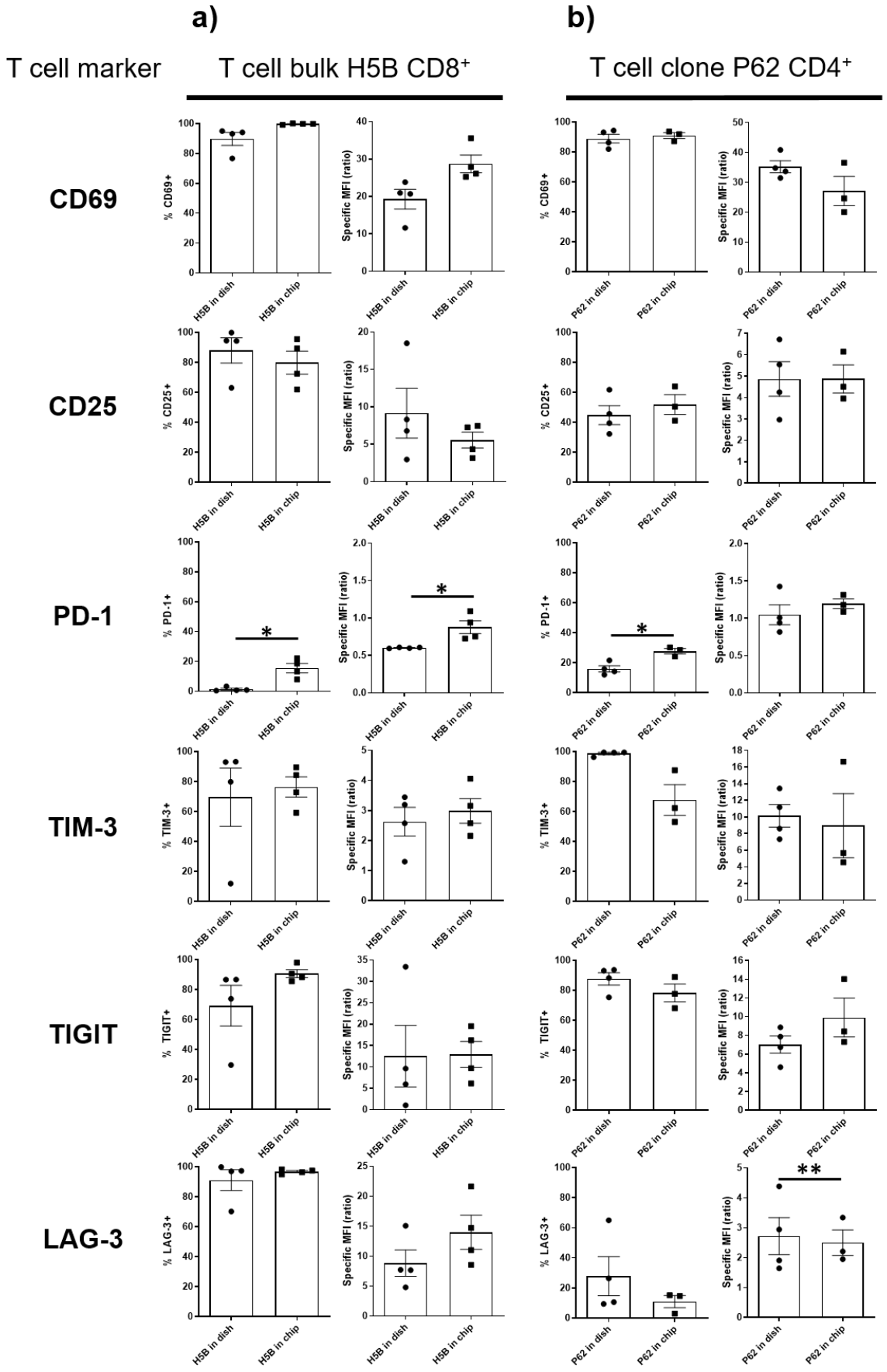

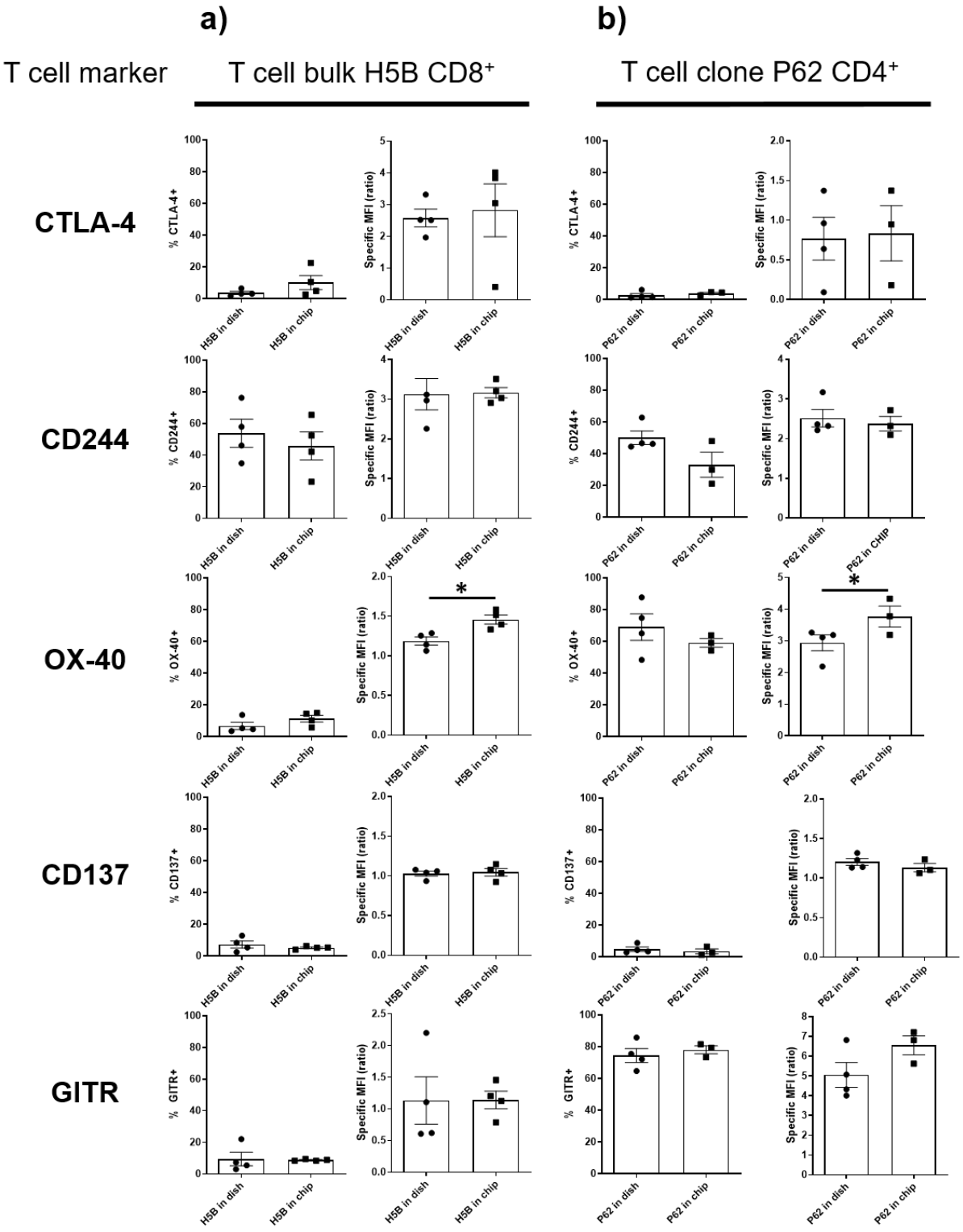


*Figure 12: The culture of T cells in chip poorly modulates the expression of T cell markers compared to the culture in dish*

*a) Expression of T cell markers in bulk T cells H5B cultured in dish and cultured in chip; representation of the % of positive cells on the left and of the specific MFI (ratio with the*

*isotype control) on the right, graphs show the mean ±SEM from 4 independent experiments.*

*b) Expression of T cell markers in T cell clone P62 cultured in dish and cultured in chip; representation of the % of positive cells on the left and of the specific MFI (ratio with the isotype control) on the right, graphs show the mean ±SEM from 4 independent experiments.*

*For comprehensive presentation, all the measurements were reported. Only for those measurements that were paired (i.e. dish and chip in the same experiment).*

*Paired t test was used for statistical analysis; *p<0.05, **p<0.01.*

### 4.4.2 Impact of ToC co-culture and anti-PD-1 treatment on T cell markers

Next, we characterized the T cells status after ToC culture with the autologous cancer cells and the impact of the presence of anti-PD-1 (Nivolumab, 10µg/ml) on the expression of other immune checkpoints.

Figure 13 shows the quantification of the expression of the activation markers CD69 and CD25 measured by flow cytometry; the left graph shows the % of positivity for the marker while the right graph indicates the specific MFI. The conditions in presence of anti-PD-1 are in blue color. Figure 13a compares H5B T cells alone in the chip ± anti-PD-1 with the H5B in co-culture with IGR-Heu cancer cells ± anti-PD-1. Similarly, Figure 13b compares the culture of P62 T cells ± anti-PD-1 with the IGR-Pub co-culture ± anti-PD-1. For CD69, while the % of positive cells is high in both T cells and cannot further increase, the speMFI increases significantly in presence of autologous cancer cells, meaning that the co-culture activates the T cells. For CD25 as well, we observed a clear increase tendency upon co-culture with cancer cells, even though the statistical significance was reached only when we compare the P62 alone with the cancer cells co-culture. Interestingly, the presence of anti-PD-1 does not have any effect on T cells activation, independently of the presence of cancer cells.

in presence of immunotherapy

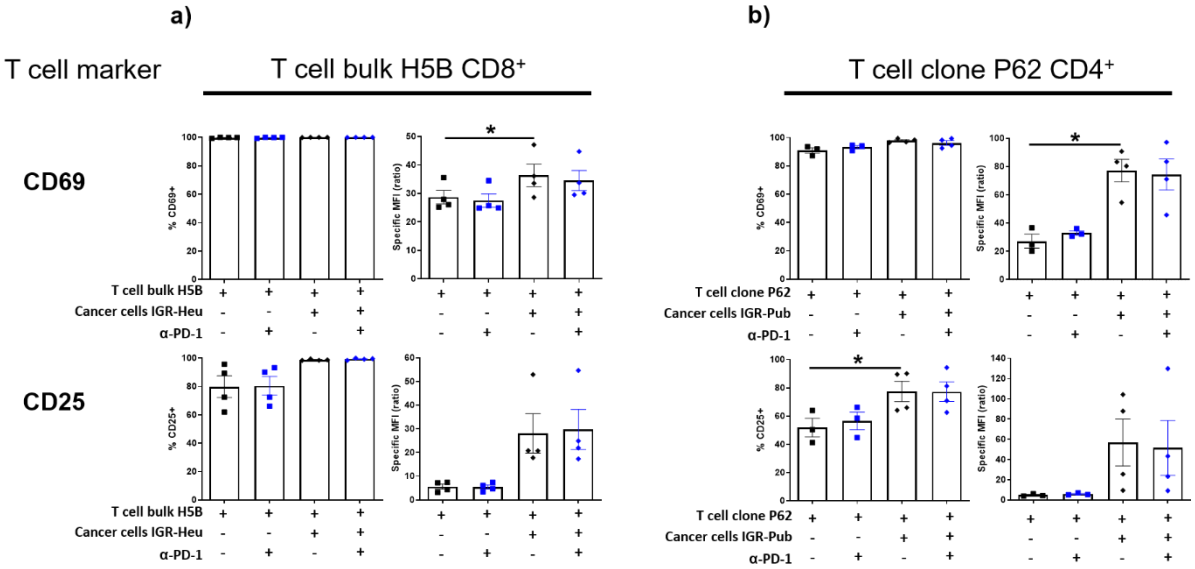


*Figure 13 T cell activation is induced by ToC co-cultures with autologous cancer cells and it is not affected by anti-PD-1 treatment*

*a) Expression of activation markers CD69 and CD25 in bulk T cells H5B cultured in chip ± IGR-Heu cancer cells and ± anti-PD-1; representation of the % of positive cells on the left and of the specific MFI on the right, graphs show the mean ±SEM from 4 independent experiments.*

*b) Expression of activation markers CD69 and CD25 in T cell clone P62 cultured in chip ± IGR-Pub cancer cells and ± anti-PD-1; representation of the % of positive cells on the left and of the specific MFI on the right, graphs show the mean ±SEM from 4 independent experiments.*

*Paired t-test was used for statistics; *p<0.05, **p<0.01*

Afterwards, we evaluated if anti-PD-1 treatment has an impact on the expression of several immune checkpoint inhibitors. Adaptive resistance to anti-PD-1 treatment could appear in patients through the expression of alternative immune checkpoints, whose pathways are not impacted from the PD-1 axis blockade. Therefore, the observation of an increased expression of another targetable immune checkpoint could provide a rationale for combined immuno-therapy treatments.

Figure 14 shows the quantifications of the expression of 6 inhibitory immune checkpoints (PD-1, TIM-3, TIGIT, LAG-3, CTLA-4 and CD244). The left graph displays the % of positive cells and the right one the speMFI.

in presence of immunotherapy

Analyzing PD-1 expression, the measurements in presence of anti-PD-1 were heavily underestimated and clearly unreliable, because of steric competition between the antibody treatment and the antibody used for flow cytometry staining. These measurements therefore are not reported in the graphs. Overall, the expression of these 6 inhibitory immune checkpoints was only mildly affected by either the presence of cancer cells or anti-PD-1 treatment. As shown in Figure 14a, the presence of cancer cells induced an increase the % of TIM-3$^+$ T cells in both treated with isotype control and treated with anti-PD-1. Similarly we observed an increase of the speMFI of TIM-3 in H5B T cells co-cultured and treated with anti-PD-1 compared to T cells alone in the chip. Strikingly, the speMFI of TIM-3 increased in co-cultured T cells in presence of ICI compared to the co-culture condition with isotype control. The % of positivity for TIGIT in H5B T cells, already pretty high (>80%), slightly increased with the cancer cells co-culture both in presence of isotype control and anti-PD-1. Studying LAG-3 expression, we observed an increase of positivity induced by the co-culture in presence of anti-PD-1 treatment. CTLA-4 as well increased the speMFI when T cells were co-cultured in presence of anti-PD-1. CD244 was not significantly modulated on H5B T cells by the presence of cancer cells nor immunotherapy.

Regarding the profiling of P62 T, Figure 14b shows mild effects, not statistically significant, induced by the co-culture and no impact by the anti-PD-1 treatment. The only the exception is represented by CD244, for which in presence of anti-PD-1 the % of positive P62 T cells decreases when co-cultured compared to T cells alone in the chip. In the other condition and cell model CD244 was not modulated neither from cancer cells nor by treatment.

TIM-3 and TIGIT are both highly expressed by H5B and P62 T cells and their expression levels remain high upon co-culture and treatment. The same observation stands for LAG-3 in H5B, whereas in P62 a tendency of increase is observed only after ToC co-culture with cancer cells. In all conditions CTLA-4 is expressed at very low levels, that we consider negligible. We could detect an increase in the speMFI of H5B T cells induced by the addition of cancer cells only in presence of anti-PD-1.

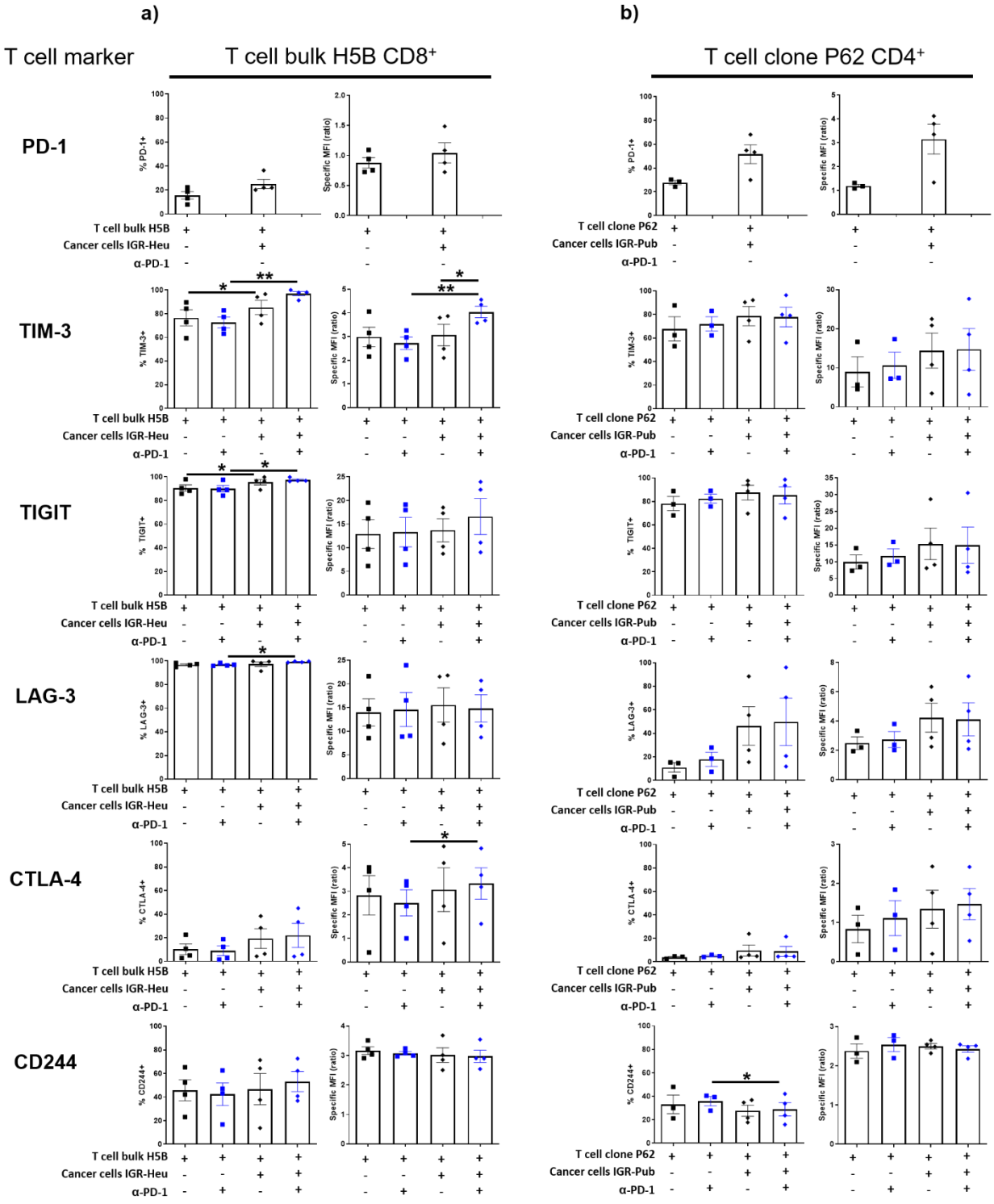


*Figure 14 : ToC co-cultures with cancer cells and treatment with anti-PD-1 have mild effects on the expression of inhibitory immune checkpoints on T cells*

*a) Expression of inhibitory immune checkpoints in bulk T cells H5B cultured in chip ± IGR-Heu cancer cells and ± anti-PD-1; representation of the % of positive cells on the left and of the specific MFI (ratio with the isotype control) on the right, graphs show the mean ±SEM*

*from 4 independent experiments.*

*b) Expression of inhibitory immune checkpoints in T cell clone P62 cultured in chip ± IGR-Pub cancer cells and ± anti-PD-1; representation of the % of positive cells on the left and of the specific MFI (ratio with the isotype control) on the right, graphs show the mean ±SEM from 4 independent experiments.*

*Paired t test was used for statistical analysis; *p<0.05, **p<0.01.*

In conclusion, in both T cell models the co-culture has a tendency to mildly increase the expression of inhibitory immune checkpoints, in presence or absence of anti-PD-1, but often without reaching statistical significance. Anti-PD-1 treatment does not modulate expression of inhibitory immune checkpoints, with the only exception of TIM-3 in the H5B T cell bulk, not for the P62 clone.

Lastly, we evaluated the expression of co-stimulatory immune checkpoints expressed on H5B T cells (Figure 15a) and the clone P62 (Figure 15b). In H5B T cells we did not observe any modulation on the expression of OX-40. On the contrary, the % of P62 positive for OX-40 as well as the speMFI, dramatically increase in presence of cancer cells. Intriguingly, the speMFI of this co-stimulatory immune checkpoint decreases when P62 T cells are co-cultured with IGR-Pub in presence of anti-PD-1. While we do not observe any changes in CD137 expression in P62 T cells, the H5B cells increase both the speMFI and the % of positivity in presence of IGR-Heu cancer cells. Similarly, in both ToC co-culture with autologous cancer cells GITR expression increases; this effect is statistically significant in both % of positive cells and speMFI for the P62 clone and in % of positivity in H5B T cells. Notably, the speMFI of GITR decreases in presence of Nivolumab in P62 cells.

in presence of immunotherapy

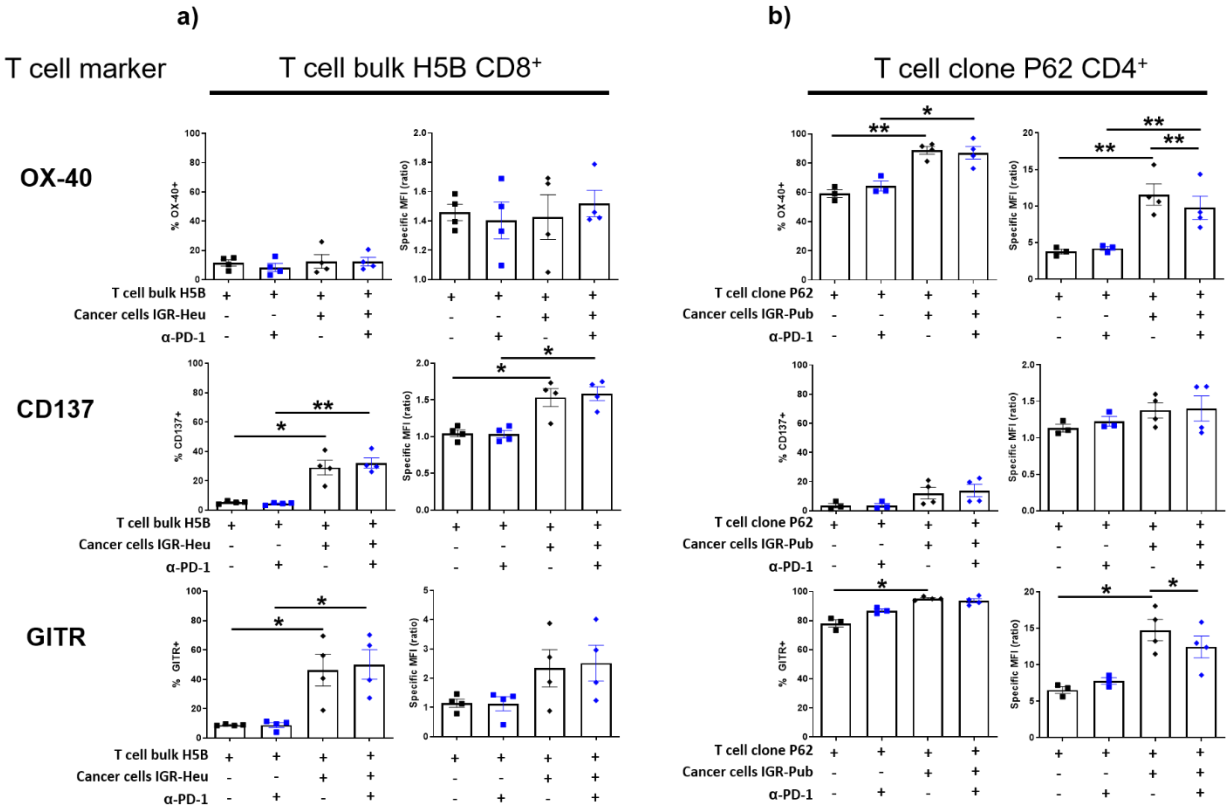


*Figure 15 : ToC co-cultures with cancer cells increase the expression of activatory immune checkpoints on T cells, while the treatment with anti-PD-1 drug has mild effects*

*a) Expression of co-stimulatory immune checkpoints in bulk T cells H5B cultured in chip ± IGR-Heu cancer cells and ± anti-PD-1; representation of the % of positive cells on the left and of the specific MFI (ratio with the isotype control) on the right, graphs show the mean ±SEM from 4 independent experiments.*

*b) Expression of co-stimulatory immune checkpoints in T cell clone P62 cultured in chip ± IGR-Pub cancer cells and ± anti-PD-1; representation of the % of positive cells on the left and of the specific MFI (ratio with the isotype control) on the right, graphs show the mean ±SEM from 4 independent experiments.*

*Paired t test was used for statistical analysis; *p<0.05, **p<0.01.*

In conclusion, ToC co-cultures with cancer cells increase the expression of activatory immune checkpoints on T cells. With the exception of the OX-40 decrease in P62 cells, the treatment with anti-PD-1 drug has only mild effects.

## 4.5 Real-time quantification of T cell toxicity upon perfusion of immunotherapy

Next, we aimed to link the T cells activation and exhaustion state as defined by their markers with their cytotoxic effector functions before and after the addition of ICI. To do so, we performed live imaging of ToC co-cultures and measured with our STAMP method the cytotoxic activity through the apoptosis reporter Cell Event (Thermofisher).

The experimental strategy to reproduce the effect of ICI addition in a reconstituted *in vitro* 3D microenvironment is illustrated in Figure 9a. First, two identical ToC containing IGR-Heu and H5B T cells (E:T ratio 1:2) were prepared without any drug addition, connected to the microfluidic setup and live-imaged every hour in transmission and fluorescence channels for a total duration of 48 hours in a video-microscope. After 16 hours of co-culture, new medium containing either anti-PD-1 (Nivolumab, 10µg/ml) or Isotype control (human IgG2a, 10µg/ml) was perfused in the chip. A low flowrate (1,5 µl/min per channel) was chosen to limit the sheer stress on the gel and not to perturb the ToC co-culture. The overnight time interval before the drug perfusion allows the stabilization of the co-cultures in 3D, presumably including a lot of cell adaptation processes, such as the above reported up-regulation of PD-1 (Figure 12 and Figure 14).

Figure 16b pictures the 37°C-heated microscope chamber ($pCO_2$= 5%), containing the chips connected to the microfluidic control system. Thanks to the collaboration with Stéphanie Descroix at Institut Curie/ Institut Pierre-Gilles de Gennes, we adapted a microfluidic system to the chamber of the Leica microscope used for live imaging. The latter consists of a MFCS pressure controller (Fluigent) that pressurizes the air and pumps it in medium reservoirs; here, the pressure applied by the air at the liquid surface is transferred on the fluid and results in the exit of the medium into the tubing system. Next, a flow unit (M, Fluigent) measures the flow rate and return the information to the controlling software; then, through custom-designed and 3D printed connectors the medium enters the two lateral chambers of the microfluidic device and in the same way exit to be collected in waste falcons.

The video analysis with the STAMP method shows (Figure 16c) that the perfusion of anti-PD-1 reduces the % of surviving cancer cells compared to the isotype control, in a robust and reproducible manner (n=4). Notably, the isotype control survival curve is not perturbed by antibody injection and flow rate variations.

In Figure 9d, the STAMP quantification of apoptosis rates, referred as the % of apoptotic cells detected in 4 hours-time-intervals, shows that the addition of anti-PD-1 almost doubles the cytotoxic activity compared to the average rate before perfusion. Of note, the apoptosis rate of the isotype control condition remains stable over time.

Representative videos of the ToC co-culture can be downloaded at the following links:

Link to video n°1 (Co-culture of IGR-Heu and autologous H5B T cells with perfusion of isotype control): http://xfer.curie.fr/get/eAiKVahZHYb/Video1_IGR-Heu%2BH5B_Isotype%20control.avi

Link to video n°2 (Co-culture of IGR-Heu and autologous H5B T cells with perfusion of anti-PD-1): http://xfer.curie.fr/get/VhU73e74awj/Video2_IGR-Heu%2BH5B_anti-PD-1.avi

Importantly, these data demonstrate that we can reproduce the response to ICI in an immunocompetent 3D *ex-vivo* lung cancer model.

Before achieving the microfluidic drug perfusion, preliminary experiments were performed without flow, in parallel chips, with isotype control or with anti-PD-1 drug. The results were not always consistent, due to the fact that a very modest experimental variation of TIL concentration substantially affected the cytotoxic measures. The microfluidic setting allows, within the same established co-culture, to measure the apoptosis induced by cytotoxic TILs before and after drug perfusion, in a very controlled and precise manner.

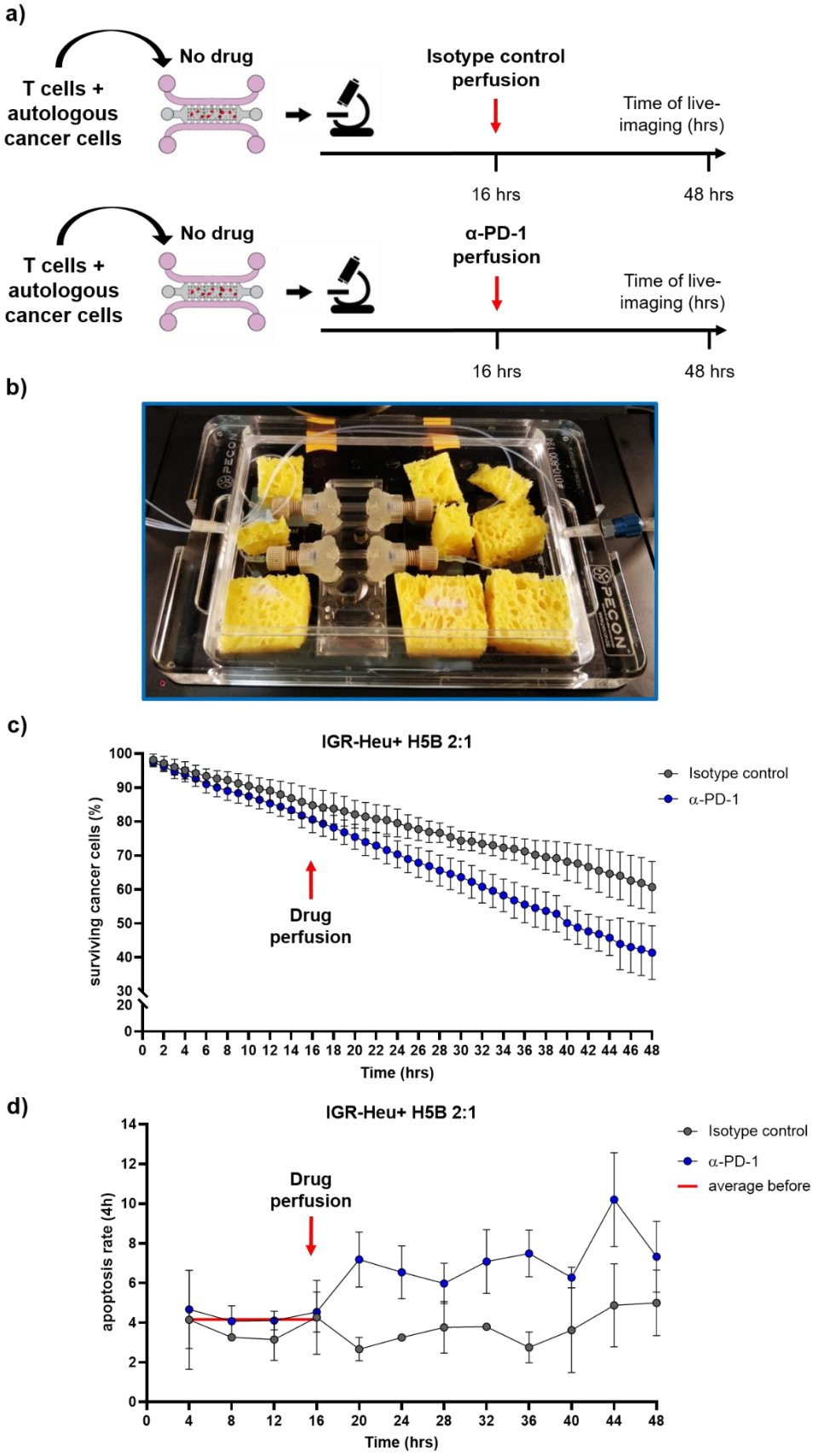


*Figure 16 Effects of treatment with anti-PD-1 drug on cancer cell viability in ToC co-cultures*

*a) Experiment workflow: T cells are embedded in the gel with autologous cancer cells and seeded in parallel chips with T cell medium; live imaging acquisition is performed every hour in transmission channel, green fluorescence channel and red fluorescent channel; the microfluidic setup allows to perfuse either isotype control or anti-PD-1 after 16hrs of ToC co-culture; the flow applied per each channel is 1.5 µl/min.*

*b) Image of the chip in the microscope chamber; custom printed connectors allow the perfusion of medium in different ToCs; sponges soaked with ddH2O contribute to the chamber humidification.*

*c) Survival curves of IGR-Heu co-cultured with the autologous T cells H5B quantified with the STAMP algorithm; the graph shows the % of surviving cancer cells calculated respect their number at t0; the curves represent the mean ±SEM of average measures of 4 independent experiments. The addition of anti-PD-1 increases the cytotoxic activity of the T cells, which results in a decreased survival of the cancer cells over time.*

*d) Comparison of the apoptosis rate quantified with the STAMP algorithm, before and after treatment. The graph reports the means ±SEM of average measures from 4 independent experiments. The red line corresponds to the basal apoptosis rate, calculated from the average of measures during the 16 hrs before drug injection.*

Next, we applied this perfusable system to assess the effect of CAF07-AD on the response to anti-PD1 in immunocompetent ToC co-cultures.

The experimental strategy, illustrated in Figure 17a, includes the imaging for 2 days of ToC co-culture of the autologous IGR-Heu cancer cells and H5B T cells alone, as control condition, or with the addition of CAF07-AD. As before, after 16 hours of co-culture without drugs, the chips are perfused with either anti-PD-1 (Nivolumab, 10µg/ml) or isotype control (human IgG2a, 10µg/ml).

Figure 17b shows a picture of the 3 parallel conditions, from which we can deduce the impossibility to add further chips in the current setting.

These experiments are still preliminary (n=2), further ToC investigations to evaluate the role of lung CAFs on immunotherapy response are on-going.

Surprisingly, in these first experiments, the addition of CAF to the ToC reduces cancer cells viability (Figure 17c) and increases apoptosis rate (Figure 17d), as compared to the IGR-Heu

+ H5B co-culture with isotype control. Strikingly, the addition of anti-PD-1 does not increase the cytotoxic activity in presence of CAF, respect to the same tri-culture perfused with isotype control.

However, future experiments will need to be performed with optimized protocols. In fact, the apoptosis rate of the conditions in presence of CAFs seems to increase upon drug or isotype perfusion, compared to the condition without CAF, suggesting some non-drug-dependent effects. A possible explanation of this phenomenon is that, as it can be observed in representative videos of the tri-culture (links below), the 16 hours before drug injection is too short for a full adaptation of the CAF in the 3D matrix.

Link to video n°3 (Tri-culture of IGR-Heu, H5B T cells and CAFs with perfusion of isotype control): http://xfer.curie.fr/get/MGiYWObe1Ob/Video3_IGR-Heu%2BH5B%2BCAF_Isotype%20control.avi

Link to video n°4 (Tri-culture of IGR-Heu, H5B T cells and CAFs with perfusion of anti-PD-1): http://xfer.curie.fr/get/NLuCAyDt1nY/Video4_IGR-Heu%2BH5B%2BCAF_anti-PD-1.avi

These experiments suggest that CAFs might promote resistance to anti-PD-1 in a ToC lung cancer model, originally responsive to immunotherapies. Moreover, they confirm the power of this microfluidic platform to recapitulate complex interactions in a 3D, albeit simplified,

upon perfusion of immunotherapy

TME thanks to more physiological culture conditions (compared to *in vitro* 2D cultures).

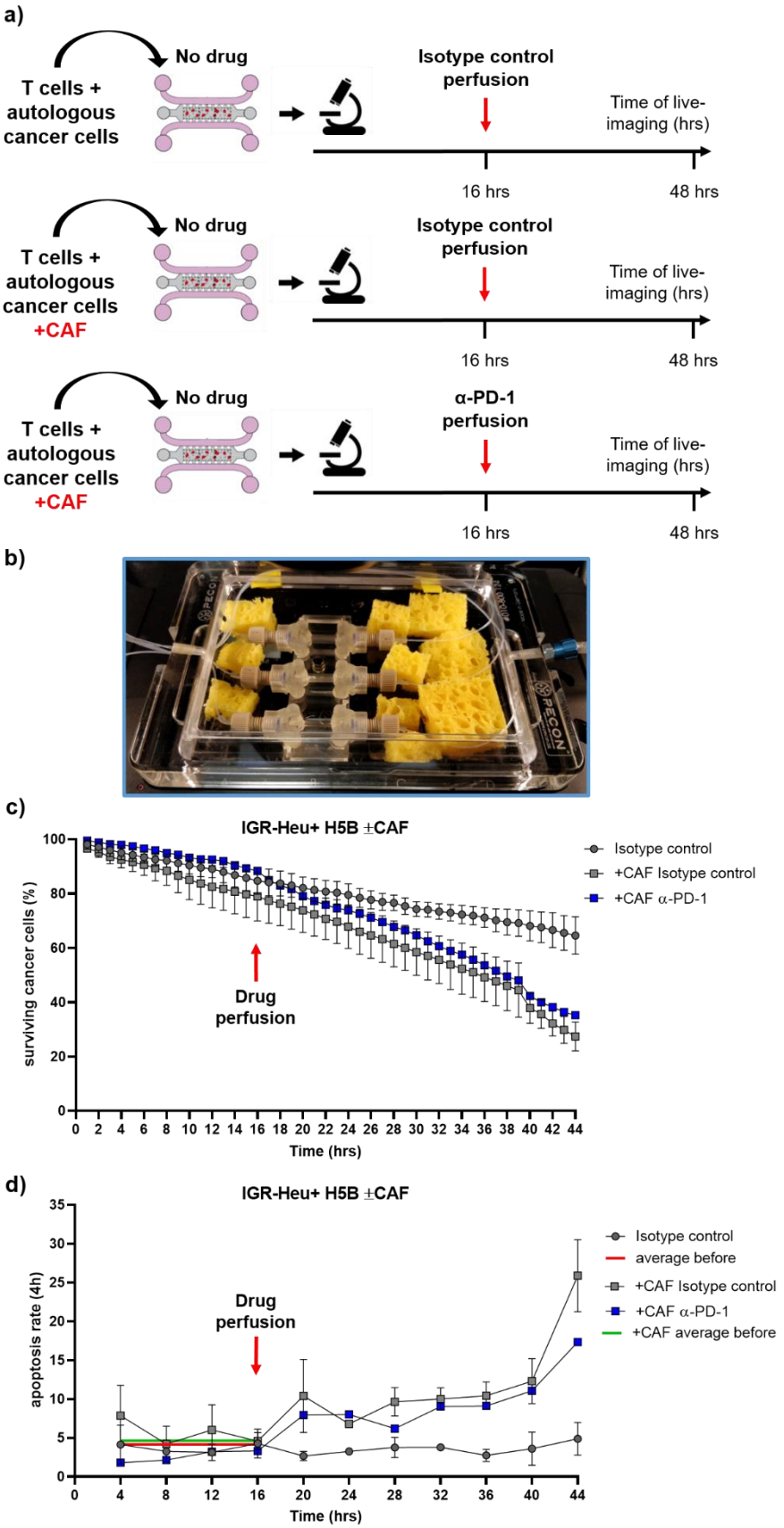

*Figure 17 Effects of CAFs on anti-PD-1 drug response in ToC co-cultures*

*a) Experiment workflow: T cells are embedded in the gel with autologous cancer cells ±CAF07-AD cells and seeded in parallel chips with T cell medium; live imaging acquisition is performed every hour in transmission channel, green fluorescence channel and red fluorescent channel. The microfluidic setup allows the perfusion of either isotype control or anti-PD-1 after 16hrs of ToC co-culture; the flow applied per each channel is 1.5 µl/min.*

*b) Image of the chip in the microscope chamber; 3 gels are connected to the microfluidic system, allowing the perfusion of medium ±ICI in different ToCs; sponges soaked with ddH2O contribute to the chamber humidification.*

*c) Survival curves of IGR-Heu co-cultured with the autologous T cells H5B quantified with the STAMP algorithm; the graph shows the % of surviving cancer cells calculated respect their number at t0; the curves represent the mean ±SEM of average measures of 2 independent experiments.*

*d) Comparison of the apoptosis rate, quantified with the STAMP algorithm, before and after treatment in ToC cultures in presence of CAF. The graph reports the mean ±SEM of average measures of 2 independent experiments. The red and green lines correspond to the basal apoptosis rate, calculated from the average of measures during the 16 hours before drug injection, in condition without and with CAF, respectively.*

# 5 Discussion

## 5.1 ToC as emerging *ex vivo* cancer models: pros and cons

The research field of 3D *ex vivo* cancer models experienced a fast development in the past decade. Concomitantly, the low reproducibility of cancer research and the mismatching results of *in vitro* and *in vivo* models compared to patients, solicit the exploration of new and more reliable cancer models. In fact, the report that only 50% of the publications in cancer biology are reproducible [213] led to the institution of a collaborative initiative, "Reproducibility Project: Cancer Biology" (RP:CB) (https://www.cos.io/rpcb), whose aim is to conduct direct replications of 50 high-impact cancer biology studies to assess reproducibility rates.

3D cancer models include different culture systems, namely 1) the organoids, self-organizing spherical structures useful to study the responses to treatment, 2) tissue slices, which best represent the original topology of the tumor, and 3) tumors-on-chip, co-cultures in micro-engineered microfluidic devices. The technical advancements in the microengineering of microfabrication and microfluidics allow now to reconstitute specific tissue features in which address biological questions. Remarkable progresses were achieved in the reconstitution of several organs-on-chip, notably the air-liquid interface of the lung, the villi of the intestine, vascular networks, the liver, the blood brain barrier and the bone with conserved functions [189], [200], [214], [215] [216], [217].

The structural complexity and the highly controllable culture conditions achieved in the organ-on-chip cultures inspired promising ideas for 3D cancer modelling. Tumors-on-chip introduce cancer cells in 3D artificial microstructures, simulating the tumor ecosystem of origin. Recent studies used ToCs to evaluate various aspects of cancer growth and invasion, such as cancer cells extravasation, vascularization and the response to treatments, specifically in lung and breast cancer models [195]–[198].

The high controllability of culture conditions allows at the same time to rationally choose the spatial disposition and ratios of cell subpopulations, to setup biochemical gradients (via

microfluidics), to modify the chemical and physical properties (e.g. stiffness) of the ECM, to regulate the availability of oxygen, and more. Indeed, the versatility of ToCs can be used on one side to reconstitute *ex vivo* complex features of the TME and on the other side, thanks to its simplification, to address the role of specific cell subtypes in cancer.

During the work of my thesis, I realized that ToCs present also some disadvantages in being used as a model to study cancer.

The very same diversity of microfluidic techniques imposes a meticulous, often time-consuming, setup to achieve suitable culture conditions. In fact, the tiniest details need to be considered to achieve successful cultures-on-chip. Evaporation, gel solutions, $CO_2$ availability, leakages and bubbles in the microfluidic system, cell staining and the timing of the experimental procedure are all possible obstacles to a successful culture on-chip.

Foremost, even the most complex 3D cultures in microfluidic devices cannot fully recapitulate the physiological TME, it will always be a simplified version of it. In fact, the in-vivo TME is greatly influenced by systemic factors (coming through the blood stream from other organs) and by the immune system (which is underrepresented when we consider only the infiltrated immune cells). Notably, the heterogeneity in cancer and in the other cell types inhabiting the TME greatly increases the complexity of the interactions occurring in it. Nevertheless, the possibility to culture on-chip homogeneous populations could help to dissect complex cancer-related mechanisms and better understand the "talk" between different cell types within the TME.

So far, the vast majority of studies exploiting ToCs favor cell lines over primary cells. Principally, because immortalized cell lines are much more resistant and assure a better and longer survival in ToCs. Secondly, because of the difficult sourcing of human primary cells, especially if they derive from fresh tumor samples.

Finally, the short time of ToC cultures (of few days) limits the observation to fast reactions of cells within the reconstituted TME, either with respect to other cells or in response to treatments. Consequently, patient-derived ToCs are not suitable to study long-term effects

induced by the TME. This is a major disadvantage, considering the striking characteristic of ICI to induce durable responses, recently observed to last up to 5 or 10 years. Many efforts are now directed to the profiling of the immune system in responders, in order not only to find predictive factors, but also to identify the mechanisms and cell subpopulations responsible for the favorable responses or the adverse resistance. The long-lasting nature of ICI may imply the involvement of memory cells. It is still unclear whether the "precursor exhausted" T cells are the ones (more) responsive to ICI treatments and whether in a second time differentiate in memory T cells, leading to durable responses. This kind of questions, linked to the durability of immune responses, will be difficult to address in ToCs.

Table 3 displays a summarized view of the pros and cons of 3D *ex vivo* cancer models.

*Table 3: pros and cons of 3D ex vivo cancer models*

| 3D ex vivo cancer model | Pros | Cons |
|---|---|---|
| Organoids | • Reproduce cellular architecture and functions of the original tissue<br>• PDOs reproduce the clinical responses of corresponding patients<br>• Include also stromal and immune components of the original tumor<br>• Limited manipulation | • Need of relatively big specimens<br>• End-point read-outs<br>• Need of laser-based microscopy: limited visualization of cell TME dynamics<br>• Long time cultures of few weeks (not suitable for rapid personalized drug testing)<br>• Autologous immune cells do not survive for a long time<br>• Complexity of protocols and media<br>• Absence of systemic factors (blood circulation, whole immune system, liver metabolism etc...) |
| Organotypic cultures (tissue slices) | • Original tissue topology and cell ratios<br>• Preserve the composition and physico-mechanical properties of the matrix<br>• Direct visualization and live imaging | • Need of relatively big specimens<br>• Limited time of culture (several days)<br>• Need of laser-based microscopy<br>• Lack of fine control of experimental conditions<br>• Absence of systemic factors (blood circulation, whole immune system, liver metabolism etc...) |
| Tumors-on-chip | • Very few cells are needed<br>• High time-lapse resolution of cell imaging<br>• Highly controllable conditions (spatial disposition and ratios of cell subpopulations, biochemical gradients, chemical and physical properties of the ECM)<br>• Customizability of architectural designs by microfabrication<br>• Miniaturization allows limited dilutions of secreted factors | • Limited time of culture (2-6 days)<br>• Complexity of the experimental setup<br>• Over-simplification of the TME<br>• Requirement of highly interdisciplinary expertise<br>• Absence of systemic factors (blood circulation, whole immune system, liver metabolism etc...)→ body on-chip? |

## 5.2 The new challenges in 3D video imaging

The advancements and the refinement of *ex* vivo 3D cancer models have not been followed by an equivalent rapid development of image analysis tools adapted to these novel 3D culture methods.

Organoids, tissue slices and tumors-on-chip show evident structural differences and distinct possible read-outs, which require the development of new imaging strategies. A limiting factor for plenty of studies exploiting *ex vivo* 3D cancer models is the fact that the imaging read-out is often an endpoint measurement. This implies the loss of a considerable amount of information that is contained in the temporal dynamics of the ongoing co-cultures. Confocal microscopy is the most commonly used imaging strategy in end-point analysis of fixed 3D cancer models. Alternatively, two-photon microscopy, usually used in whole animal intravital imaging, was applied to live-image tissue slices thank to its high penetrance and low phototoxicity. However, the live staining with fluorescent antibodies of the cells has a limited duration in time (due to photobleaching) and it may alter the normal behaviors of cells (for example antibodies binding to CD3 or the co-receptors CD8 and CD4 may not-physiologically activate T cells). With the aim of performing few-day-lasting acquisitions, the microfluidic devices we used for our ToC cultures offered a good optical compromise. In fact, these devices present lower thickness of the hydrogel chambers (250 µm) compared to the dimension of organoids (~500 µm) or tissue slices (300µm-1mm) and the cells dispersed in the gel are easier to track and analyze individually. Accordingly, recent studies profit from the customable geometries of microfluidic devices to study the motility of immune cells. Garcia-Arcos and colleagues accurately described how microstructures can deconstruct the variety of physical obstacles the cells encounter and how these microfluidic platforms can be exploited to study in original ways cell motility [218].

As a matter of fact, the structural differences of the culture supports and the biological phenomena to be studied, require an adapted imaging setup and an associated analysis. At this time, a multitude of imaging tools already exist, but the scaling-up of data generated by

live-imaging need automation. The architectural differences in 3D culture systems aforementioned impose different imaging settings and this necessitates the development of multiple automated image analysis strategies, as each experimental setup is different and needs an adapted algorithm.

Starting from the practical need of an automated method to quantify the cytotoxic activity of T cells in our autologous lung ToCs, in collaboration with Prof Eugenio Martinelli and Prof. Arianna Mencattini from University of Roma Tor Vergata, we developed the "STAMP method", reported in a paper recently submitted (see Results). The STAMP method localizes and tracks the cells of interest in the fluorescence channel, then specifically quantifies their death in time and in space thanks to an apoptosis fluorescence reporter. Intrigued by the observation that the apoptosis rate of cancer cells was increasing over time, we defined a novel mathematical concept, "the potential of death", to understand whether the death of a cancer cell could influence the death of the surrounding cells. We demonstrated that dying cells could increase the probability of encountering death in the cells nearby. The increase of potential of death overtime could be explained by the release of "death signals"/small death-associated molecules to the closer cancer cells. An alternative explanation could be that the apoptotic bodies, expressing high levels of PtdSer [219], could locally retain T cells through its interaction with TIM-3 [220]. This local retention would lead to the preferential killing of nearby cancer cells/accumulation of T cells in "death zones".

Of note, the STAMP method is now the object of a patent filed on September 2020 (P36165-FR – 7688716).

Cancer cells death is only one aspect of 3D co-cultures that could be quantified in the videos. In a past publication, our team used short time intervals (with acquisitions in the bright field every 2min) to track the interactions between immune cells and cancer cells [203]. A later work of our collaborators identified that 20s-time-intervals is the optimal acquisition setting to study immune cells movements and interactions with cancer cells [221]. Aware of this

assessment, we started to acquire 20s-time-intervals videos in bright field, in order to compare the morphodynamics of T cells before and after the addition of ICI in lung ToCs.

Initially, we questioned ourselves on which quantifiable parameters, or "descriptors" could describe differences in T cells morphology and dynamics, when co-cultured in ToC in presence or absence of ICI. We considered to study the morphology of T cells, their dimension, the dynamics and directionality of T cells, or the analyze the time of interactions between cancer and T cells (duration of contacts with a particular cancer cell and total time of contacts with other cancer cells). Eventually, inspired by the expanding computer vision field of Artificial Intelligence (AI) and machine learning, also applied to biology, we realized that within the co-culture videos there is a multitude of unknown "features" that could be used to classify the complex cellular behaviors within the 3D cultures, of which many are not perceptible by the human eye. For example, our collaborators recently published a novel AI-based method to perform a comprehensive and fully automated analysis of cell motility behaviors captured in time-lapse microscopy images and to correctly classify drug-treated and not-treated ToC [222].

In a newly started collaboration, with Auguste Genovesio at Ecole Normale Superieure (ENS), we are using a machine learning approach to characterize T cells morphodynamics in presence or absence of ICI, exploiting the vides of our autologous lung ToCs. This innovative AI image analysis approach could give us some unexpected insights on cancer-T cells interactions and reveal some differences in morphodynamics that could be correlated with the ICI treatment.

Further computational big data analysis could use the entire set of descriptors and features to find causality correlations between these numerous parameters and the responses to ICI.

## 5.3 Clinical relevance of ToC

### 5.3.1 Ex-vivo evaluation of responses to ICI

Clinical data show that biomarkers such as PD-L1 expression and Tumor Mutational Burden (TMB) are not reliable to predict an efficient response in the patient. This is partly due to the

lack of standardized procedures to analyze these markers, but also due to the limited specificity of those markers, as their presence depend on multiple factors. Reducing the complexity of the TME using ToC strategies may help to better describe the interactions occurring in it and define which factors may influence the response to ICI.

Nowadays, many studies aim to characterize the populations within the TME, through scRNA-seq and immunophenotyping approaches in order to find the actors of the response to ICI. Nonetheless, the complexity of the TME not only can be described by its cellular composition and spatial distribution within the ECM, but also by the nature of the dynamic interactions happening between the cells. Part of the difficulties in deciphering the TME resides in the richness of interactions between cell types (by direct contact, receptor-ligands interactions, autocrine, paracrine and endocrine signals) and additionally between the cells and the surrounding environment via mechanosensing.

With this work, we demonstrate that autologous lung ToC platforms are useful tools to recapitulate immune responses to immune checkpoint inhibitors (see Results). The high clinical impact and the broad use of anti-PD-1 treatment oriented our choice for our first ICI drug to test in chip. Even though PD-1 was mildly expressed by our T cell clones when cultured alone, we observed that the co-culture with cancer cells increased the expression of this inhibitory receptor (see Figure 14). Moreover, our cellular model displays similar levels of expression of PD-1 if compared to the ones observed in NSCLC lung cancer patients [168].

The effector functions of immune cells in ToCs can be precisely measured using the STAMP method, where the cytotoxic activity of T cells is quantified through counting the death of target cells. This kind of functional assay directly describes effector functions of T cells, differently from the commonly used essays, such as ELISpot (Enzyme-Linked ImmunoSpot) or ELISA (Enzyme-Linked ImmunoSorbent Assay), measuring the release of cytokines by effector T cells, classically IFN-γ or IL-2. Nevertheless, it would be interesting to include the analysis of the secretome in the profiling of immune responses occurring in autologous ToCs. In line with this purpose, the same AIM-biotech commercial microfluidic device, that we used

for our experiments, was used by Roger Kamm's team to analyze a panel of cytokines released upon ToC co-cultures, showing the feasibility of the analysis of the secretome in our same settings [204].

Moreover, during this thesis, by harvesting the immune cells from the chip after few days of co-culture, T cell were stained and analyzed by flow cytometry in order to characterize their activation and exhaustion status. Therefore, for the first time we have an insight on the specific cytotoxic activity of TILs and the associated expression profile of various immune checkpoints. Often, the expression of immune checkpoints in patient TILs has been automatically overlapped with a dysfunctional status of T cells, but in our system we observe a marked cytotoxic activity even though T cells express immune checkpoint receptors.

The fact that in our work we observe effector functions in T cells expressing immune checkpoints, could be due to the over-simplification of the TME, meaning that the presence of other cell types of the TME is needed the additively contribute to an immunosuppressive environment. Conversely, the cancer cells in ToCs could need more time to create an immunosuppressive environment and we should adjust our observation window. Indeed, in patients it would not be possible to assess the contribution of a single T cell subpopulation to the response to ICI directly, as the response to the treatment is influenced by the whole TME.

### 5.3.2 Study of resistance mechanisms to ICI

In immunocompetent ToCs we detected extrinsic (TME-dependent) mechanisms of resistance to ICI. First, after the treatment with anti-PD-1 we observed the upregulation of TIM-3, an alternative immune checkpoint, on $CD8^+$ TILs. This overexpression could have lead over time to a dysfunctional phenotype, as the high expression of this immune checkpoint in TILs is correlated with poor prognosis in lung cancer [223]. Moreover, adding primary cancer-associated fibroblasts to the autologous cancer-TILs co-culture dampened the effect of anti-PD-1, thus recapitulating an extrinsic mechanism of resistance to ICI. These interesting preliminary results showed a surprising effect of CAF presence on cancer cells viability, which decreased independently from ICI treatment. Unfortunately we lack of a good "normal fibroblast" control. When we characterized the fibroblasts (see Results), the so-called normal

human lung fibroblasts (NHLF) appeared activated, showing a CAF-S1-like phenotype. Further experiments are in progress to test if the CAF-like phenotype could be reversed by the culture in the 3D matrix, assuming that the activation of NHLF is due to 2D culture conditions (particularly by plastic stiffness).

### 5.3.3 Testing of combination therapies

A future perspective of the project is to use lung ToCs to test new combinations of ICI and to compare it to ICI monotherapy or to the combination of chemotherapy plus ICI (taxol/pemetrexed followed by anti-PD-1 treatment). The last two treatments (more commonly used in clinics) could be used as a baseline to assess the efficacy of ICI combinations. Thanks to the microfluidic implementation, it will be possible to sequentially perfuse ToCs, in order to evaluate if the injection of the second ICI could potentiate the T-cell cytotoxicity of the first ICI or overcome a potential resistance to the first ICI. It would be interesting to perform a long–lasting experiment (1 or 2 weeks) with continuous perfusion to see if the cytotoxic activity would decrease over time and, in case, if T cells could be reinvigorated by the addition of a second ICI.

While profiling both autologous pairs of TILs co-cultured in ToCs, we noted that TIM-3 and TIGIT are two inhibitory checkpoints that are highly expressed in presence of cancer cells. Interestingly, their expression remains high (TIM-3 even increases in $CD8^+$ T cells) upon anti-PD-1 treatment. Therefore, it will be interesting to test the following combinations of ICIs: anti-PD-1 followed by anti-TIM-3 and in alternative anti-TIGIT followed by anti-PD-L1 [139]. Both combinations are currently tested in phase II clinical trials. Interesting results are also obtained with TIM-3+PD-1 bispecific antibodies. Moreover, since very encouraging results have been reported in patients treated with the combination of Atezolizumab (anti-PD-L1) with Tiragolumab (anti-TIGIT), we will test the combination of those two Genentech molecules in lung ToCs.

### 5.3.4 Towards fresh-tumor-derived ToCs

A promising future application is the generation of patient-derived ToCs for patients preclinical profiling and for correlation studies between clinical responses and ToC responses.

We are currently setting up the necessary steps to achieve this crucial progress in the clinical pertinence of the ToC cell models: from immortalized cell lines or amplified frozen clones, to primary cells from fresh lung cancer samples. In collaboration with Pr. Gérard Zalcman, head of the thoracic oncology department of Bichat hospital, Dr. Solenn Brosseau will coordinate the transfer of fresh samples of resectable lung cancers to Institut Curie. The samples will come from resectable lung tumors, in patients naïve from any kind of anti-tumor treatments. After tumor samples digestion, we will perform fluorescence-activated cell sorting (FACS) in order to isolate the populations of interest (cancer cells, TILs and CAFs) and reconstitute ToC co-cultures. Specific cell populations will be included or excluded to build ToC "à la carte", allowing to weight the specific contribution of each of these cell populations to the responsiveness to ICI. Afterwards, it would be interesting to compare these "à la carte" ToCs with "full menu" ToC, i.e. complete ToCs composed of the whole digested tumor, from which the global content of viable cells will be sorted without any population selection. The impact of a single population (or subpopulation) could be inversely tested by reconstituting a "reduced-menu" ToC, excluding exclusively the population of interest from the whole digested tumor.

Since a very small amount of cells (in the order of few thousands) is needed to establish co-cultures on-chip, the remaining sorted cells could be further characterized by flow cytometry. This would allow us to describe the cellular phenotypes of the samples received and to associate it to the response to immunotherapies observed in the ToCs. Furthermore, these data will be integrated with the clinical responses that will be observed in the treated patients. Succeeding in this attempt would provide a strong proof-of-concept of the feasibility and reliability to use the tumors-on-chip for patients pre-clinical profiling.

In long term, patients could benefit from the approach developed in this PhD thesis. As illustrated in Figure 18, the possibility of performing a parallelized characterization of the fresh tumor samples (ToC behaviors, cellular phenotyping and clinical responses) could uncover new insights on predictive factors to ICI responses and be used to identify adapted targets for patient's treatment, moving a step forward in the field of precision medicine.

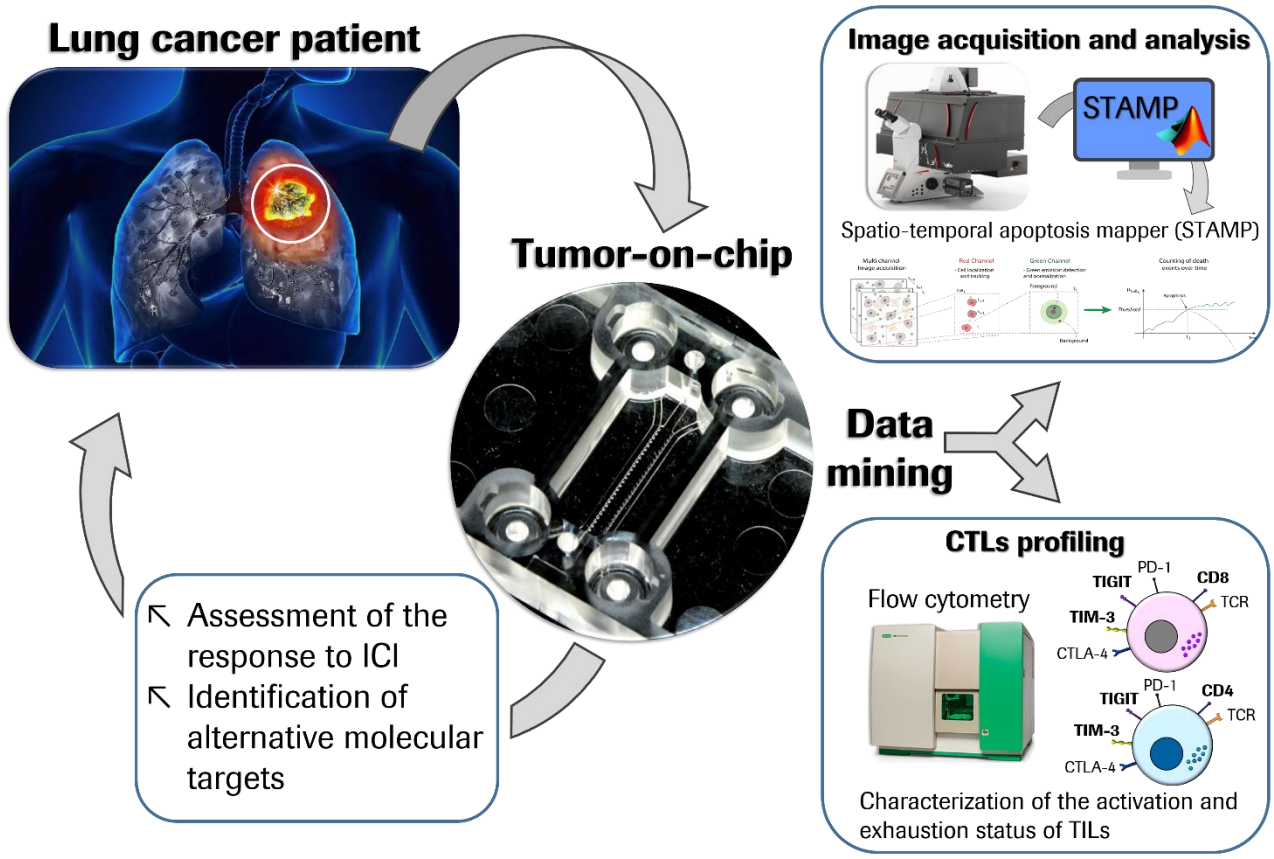


*Figure 18 : Graphical abstract illustrating the global approaches and results of this PhD thesis*

.

# 6 Bibliography

[1] F. Bray, J. Ferlay, I. Soerjomataram, R. L. Siegel, L. A. Torre, and A. Jemal, "Global cancer statistics 2018: GLOBOCAN estimates of incidence and mortality worldwide for 36 cancers in 185 countries," *CA. Cancer J. Clin.*, vol. 68, no. 6, pp. 394–424, 2018.

[2] L. M. O'Keeffe, G. Taylor, R. R. Huxley, P. Mitchell, M. Woodward, and S. A. E. Peters, "Smoking as a risk factor for lung cancer in women and men: A systematic review and meta-analysis," *BMJ Open*, vol. 8, no. 10, pp. 1–12, 2018.

[3] M. J. Thun *et al.*, "50-Year trends in smoking-related mortality in the United States," *N. Engl. J. Med.*, vol. 368, no. 4, pp. 351–364, 2013.

[4] "WHO | Download the raw data files of the WHO Mortality Database." [Online]. Available: https://www.who.int/healthinfo/statistics/mortality_rawdata/en/. [Accessed: 21-Apr-2020].

[5] R. L. Siegel, K. D. Miller, and A. Jemal, "Cancer statistics, 2020," *CA. Cancer J. Clin.*, vol. 70, no. 1, pp. 7–30, 2020.

[6] M. B. Schabath and M. L. Cote, "Cancer progress and priorities: Lung cancer," *Cancer Epidemiol. Biomarkers Prev.*, vol. 28, no. 10, pp. 1563–1579, 2019.

[7] A. J. Alberg, M. V Brock, J. G. Ford, J. M. Samet, and S. D. Spivack, "Epidemiology of Lung Cancer 3rd ed : American College of Chest Physicians Evidence-Based Clinical Practice Guidelines," *Chest*, vol. 143, no. 5, pp. e1S-e29S, 2013.

[8] L. Corrales, R. Rosell, A. F. Cardona, C. Martín, Z. L. Zatarain-barrón, and O. Arrieta, "Critical Reviews in Oncology / Hematology Lung cancer in never smokers : The role of di ff erent risk factors other than tobacco smoking," *Crit. Rev. Oncol. / Hematol.*, vol. 148, no. January, p. 102895, 2020.

[9] J. E. Bailey-Wilson *et al.*, "A major lung cancer susceptibility locus maps to chromosome 6q23-25," *Am. J. Hum. Genet.*, vol. 75, no. 3, pp. 460–474, 2004.

[10] Y. Bosse and C. I. Amos, "A decade of GWAS results in lung cancer," *Cancer Epidemiol. Biomarkers Prev.*, vol. 27, no. 4, pp. 363–379, 2018.

[11] J. D. McKay *et al.*, "Large-scale association analysis identifies new lung cancer susceptibility loci and heterogeneity in genetic susceptibility across histological subtypes," *Nat. Genet.*, vol. 49, no. 7, pp. 1126–1132, 2017.

[12] R. Kalluri *et al.*, "The 2015 World Health Organization Classification of Lung Tumors: Impact of Genetic, Clinical and Radiologic Advances since the 2004 Classification," *CA. Cancer J.*

*Clin.*, vol. 10, no. 9, pp. 1243–1260, 2016.

[13] A. G. Nicholson *et al.*, "The international association for the study of lung cancer lung cancer staging project: Proposals for the revision of the clinical and pathologic staging of small cell lung cancer in the forthcoming eighth edition of the tnm classification for lung cancer," *J. Thorac. Oncol.*, vol. 11, no. 3, pp. 300–311, 2016.

[14] M. S. Lawrence *et al.*, "Mutational heterogeneity in cancer and the search for new cancer-associated genes," *Nature*, vol. 499, no. 7457, pp. 214–218, 2013.

[15] A. Marchetti *et al.*, "EGFR mutations in non-small-cell lung cancer: Analysis of a large series of cases and development of a rapid and sensitive method for diagnostic screening with potential implications on pharmacologic treatment," *J. Clin. Oncol.*, vol. 23, no. 4, pp. 857–865, 2005.

[16] J. F. Gainor *et al.*, "ALK rearrangements are mutually exclusive with mutations in EGFR or KRAS: An analysis of 1,683 patients with non-small cell lung cancer," *Clin. Cancer Res.*, vol. 19, no. 15, pp. 4273–4281, 2013.

[17] E. A. Collisson *et al.*, "Comprehensive molecular profiling of lung adenocarcinoma: The cancer genome atlas research network," *Nature*, vol. 511, no. 7511, pp. 543–550, 2014.

[18] C. M. Rudin *et al.*, "Lung cancer in never smokers: Molecular profiles and therapeutic implications," *Clin. Cancer Res.*, vol. 15, no. 18, pp. 5646–5661, 2009.

[19] K. Sehgal, R. Patell, D. Rangachari, and D. B. Costa, "Targeting ROS1 rearrangements in non-small cell lung cancer with crizotinib and other kinase inhibitors," *Transl. Cancer Res.*, vol. 7, no. Suppl 7, pp. S779–S786, 2018.

[20] R. S. Herbst, D. Morgensztern, and C. Boshoff, "Review The biology and management of non-small cell lung cancer," *Nat. Publ. Gr.*, 2018.

[21] F. Skoulidis *et al.*, "STK11/LKB1 mutations and PD-1 inhibitor resistance in KRAS-mutant lung adenocarcinoma," *Cancer Discov.*, vol. 8, no. 7, pp. 822–835, 2018.

[22] R. Cristescu *et al.*, "Pan-tumor genomic biomarkers for PD-1 checkpoint blockade-based immunotherapy," *Science (80-. ).*, vol. 362, no. 6411, 2018.

[23] S. Burdett, "Preoperative chemotherapy for non-small-cell lung cancer: A systematic review and meta-analysis of individual participant data," *Lancet*, vol. 383, no. 9928, pp. 1561–1571, 2014.

[24] F. G. Davis, T. A. Dolecek, B. J. McCarthy, and J. L. Villano, "Toward determining the lifetime occurrence of metastatic brain tumors estimated from 2007 United States cancer incidence

data," *Neuro. Oncol.*, vol. 14, no. 9, pp. 1171–1177, 2012.

[25] G. Loganadane *et al.*, "Brain radiation necrosis: Current management with a focus on non-small cell lung cancer patients," *Front. Oncol.*, vol. 8, no. SEP, 2018.

[26] F. Agustoni *et al.*, "EGFR-directed monoclonal antibodies in combination with chemotherapy for treatment of non-small-cell lung cancer: an updated review of clinical trials and new perspectives in biomarkers analysis," *Cancer Treat. Rev.*, vol. 72, no. November 2017, pp. 15–27, 2019.

[27] M. K. Mayekar and T. G. Bivona, "Current Landscape of Targeted Therapy in Lung Cancer," *Clin. Pharmacol. Ther.*, vol. 102, no. 5, pp. 757–764, 2017.

[28] F. Barlesi *et al.*, "Routine molecular profiling of patients with advanced non-small-cell lung cancer: Results of a 1-year nationwide programme of the French Cooperative Thoracic Intergroup (IFCT)," *Lancet*, vol. 387, no. 10026, pp. 1415–1426, 2016.

[29] E. B. Garon *et al.*, "Five-year overall survival for patients with advanced non-small-cell lung cancer treated with pembrolizumab: Results from the phase i KEYNOTE-001 study," *J. Clin. Oncol.*, vol. 37, no. 28, pp. 2518–2527, 2019.

[30] Committee for Medicinal Products for Human Use (CHMP), "EMA/CHMP/346038/2019," vol. 1, no. July, p. 10, 2019.

[31] G. C. and R. A. S. Jia Li Low, Robert J. Walsh, Yvonne Ang, "The evolving immuno-oncology landscape in advanced lung cancer: first-line treatment of non-small cell lung cancer," *Ther. Adv. Med. Oncol.*, vol. 11, no. 6, pp. 259–261, 2019.

[32] J. A. Bluestone *et al.*, "Collateral damage: Insulin-dependent diabetes induced with checkpoint inhibitors," *Diabetes*, vol. 67, no. 8, pp. 1471–1480, 2018.

[33] K. Sobierajska, W. M. Ciszewski, I. Sacewicz-Hofman, and J. Niewiarowska, "Endothelial Cells in the Tumor Microenvironment," in *Advances in Experimental Medicine and Biology*, vol. 1234, Springer, 2020, pp. 71–86.

[34] J. Goveia *et al.*, "An Integrated Gene Expression Landscape Profiling Approach to Identify Lung Tumor Endothelial Cell Heterogeneity and Angiogenic Candidates," *Cancer Cell*, vol. 37, no. 1, pp. 21-36.e13, 2020.

[35] L. Ramage, "Integrins and extracellular matrix in mechanotransduction," *Cell Health Cytoskelet.*, vol. 4, pp. 1–9, 2012.

[36] O. De Wever, P. Demetter, M. Mareel, and M. Bracke, "Stromal myofibroblasts are drivers of invasive cancer growth," *Int. J. Cancer*, vol. 123, no. 10, pp. 2229–2238, 2008.

[37] E. Henke, R. Nandigama, and S. Ergün, “Extracellular Matrix in the Tumor Microenvironment and Its Impact on Cancer Therapy,” vol. 6, no. January, pp. 1–24, 2020.

[38] T. Karampitsakos *et al.*, “Lung cancer in patients with idiopathic pulmonary fibrosis,” *Pulm. Pharmacol. Ther.*, vol. 45, pp. 1–10, 2017.

[39] E. A. De Jaeghere, H. G. Denys, and O. De Wever, “Fibroblasts Fuel Immune Escape in the Tumor Microenvironment,” *Trends in Cancer*, 2019.

[40] H. Xiang *et al.*, “Cancer-Associated Fibroblasts Promote Immunosuppression by Inducing ROS-Generating Monocytic MDSCs in Lung Squamous Cell Carcinoma,” *Cancer Immunol. Res.*, vol. 8, no. 4, pp. 436–450, 2020.

[41] M. R. Nazareth *et al.*, “Characterization of Human Lung Tumor-Associated Fibroblasts and Their Ability to Modulate the Activation of Tumor-Associated T Cells,” *J. Immunol.*, 2007.

[42] M. Huang *et al.*, “Non-small cell lung cancer cyclooxygenase-2-dependent regulation of cytokine balance in lymphocytes and macrophages: Up-regulation of interleukin 10 and down-regulation of interleukin 12 production,” *Cancer Res.*, vol. 58, no. 6, pp. 1208–1216, 1998.

[43] M. Platten, W. Wick, and B. J. Van Den Eynde, “Tryptophan catabolism in cancer: Beyond IDO and tryptophan depletion,” *Cancer Res.*, vol. 72, no. 21, pp. 5435–5440, 2012.

[44] A. Costa *et al.*, “Fibroblast Heterogeneity and Immunosuppressive Environment in Human Breast Cancer,” *Cancer Cell*, vol. 33, no. 3, pp. 463-479.e10, 2018.

[45] A. M. Givel *et al.*, “MiR200-regulated CXCL12β promotes fibroblast heterogeneity and immunosuppression in ovarian cancers,” *Nat. Commun.*, vol. 9, no. 1, 2018.

[46] F. Pelon *et al.*, “Cancer-associated fibroblast heterogeneity in axillary lymph nodes drives metastases in breast cancer through complementary mechanisms,” *Nat. Commun.*, vol. 11, no. 1, 2020.

[47] Y. Kieffer *et al.*, “Single-Cell Analysis Reveals Fibroblast Clusters Linked to Immunotherapy Resistance in Cancer,” *Cancer Discov.*, no. September, pp. 1330–1352, 2020.

[48] T. Boon, J. C. Cerottini, B. Van Den Eynde, P. Van Der Bruggen, and A. Van Pel, “Tumor antigens recognized by T lymphocytes,” *Annual Review of Immunology*, vol. 12. Annual Reviews Inc., pp. 337–365, 28-Nov-1994.

[49] B. Stankovic *et al.*, “Immune Cell Composition in Human Non-small Cell Lung Cancer,” *Front. Immunol.*, vol. 9, no. February, p. 3101, 2018.

[50] A. Ashkenazi and V. M. Dixit, “Death receptors: Signaling and modulation,” *Science (80-. ).*,

vol. 281, no. 5381, pp. 1305–1308, 1998.

[51] S. L. K. P. J. polverini Douglas A. Arenberg, I. Susan B. Morris,* Marie D. Burdick,* Mary C. Glass,* Dennis T.Taub, and and R. M. S. Mark D. Iannettoni,Richard I.Whyte, "Interferon-γ-inducible Protein 10 (IP-10) Is an Angiostatic Factor That Inhibits Human Non-small Cell Lung Cancer (NSCLC) Tumorigenesis and Spontaneous Metastases," *J Exp Med*, vol. 53, no. 9, pp. 1689–1699, 1996.

[52] H. Jian, S. Fangrong, H. Haitao, L. Chunhua, and Z. Guangbo, "Th1high in tumor microenvironment is an indicator of poor prognosis for patients with NSCLC," *Oncotarget*, vol. 8, no. 8, pp. 13116–13125, 2017.

[53] Y. Togashi, K. Shitara, and H. Nishikawa, "Regulatory T cells in cancer immunosuppression — implications for anticancer therapy," *Nat. Rev. Clin. Oncol.*, vol. 16, no. 6, pp. 356–371, 2019.

[54] K. Reynders and D. De Ruysscher, "Tumor infiltrating lymphocytes in lung cancer: A new prognostic parameter," *J. Thorac. Dis.*, vol. 8, no. 8, pp. E833–E835, 2016.

[55] E. Brambilla *et al.*, "Prognostic effect of tumor lymphocytic infiltration in resectable non-small-cell lung cancer," *J. Clin. Oncol.*, vol. 34, no. 11, pp. 1223–1230, 2016.

[56] M. Binnewies *et al.*, "Understanding the tumor immune microenvironment (TIME) for effective therapy," *Nat. Med.*, vol. 24, no. 5, pp. 541–550, 2018.

[57] L. Munoz-Erazo, J. L. Rhodes, V. C. Marion, and R. A. Kemp, "Tertiary lymphoid structures in cancer – considerations for patient prognosis," *Cell. Mol. Immunol.*, vol. 17, no. 6, pp. 570–575, 2020.

[58] Y. Lavin *et al.*, "Innate Immune Landscape in Early Lung Adenocarcinoma by Paired Single-Cell Analyses," *Cell*, vol. 169, no. 4, pp. 750-765.e17, 2017.

[59] W. H. Fridman, L. Zitvogel, C. Sautès-Fridman, and G. Kroemer, "The immune contexture in cancer prognosis and treatment," *Nat. Rev. Clin. Oncol.*, vol. 14, no. 12, pp. 717–734, 2017.

[60] A. M. G. Houghton, "Mechanistic links between COPD and lung cancer," *Nat. Rev. Cancer*, vol. 13, no. 4, pp. 233–245, 2013.

[61] G. A. Banat *et al.*, "Immune and inflammatory cell composition of human lung cancer stroma," *PLoS One*, vol. 10, no. 9, Sep. 2015.

[62] S. B. Coffelt, M. D. Wellenstein, and K. E. De Visser, "Neutrophils in cancer: Neutral no more," *Nat. Rev. Cancer*, vol. 16, no. 7, pp. 431–446, 2016.

[63] G. Mollaoglu *et al.*, "The Lineage-Defining Transcription Factors SOX2 and NKX2-1

Determine Lung Cancer Cell Fate and Shape the Tumor Immune Microenvironment," *Immunity*, vol. 49, no. 4, pp. 764-779.e9, 2018.

[64] A. J. Gentles *et al.*, "The prognostic landscape of genes and infiltrating immune cells across human cancers," *Nat. Med.*, vol. 21, no. 8, pp. 938–945, 2015.

[65] A. J. Templeton *et al.*, "Prognostic role of neutrophil-to-lymphocyte ratio in solid tumors: A systematic review and meta-analysis," *J. Natl. Cancer Inst.*, vol. 106, no. 6, 2014.

[66] C. Fu *et al.*, "Activation of the IL-4/STAT6 Signaling Pathway Promotes Lung Cancer Progression by Increasing M2 Myeloid Cells," *Front. Immunol.*, vol. 10, no. November, pp. 1–17, 2019.

[67] J. J. W. Chen *et al.*, "Tumor-associated macrophages: The double-edged sword in cancer progression," *J. Clin. Oncol.*, vol. 23, no. 5, pp. 953–964, 2005.

[68] M. S. Caetano *et al.*, "IL6 blockade reprograms the lung tumor microenvironment to limit the development and progression of K-ras-mutant lung cancer," *Cancer Res.*, vol. 76, no. 11, pp. 3189–3199, 2016.

[69] C. M. Fares, E. M. Van Allen, C. G. Drake, J. P. Allison, and S. Hu-Lieskovan, "Mechanisms of Resistance to Immune Checkpoint Blockade: Why Does Checkpoint Inhibitor Immunotherapy Not Work for All Patients?," *Am. Soc. Clin. Oncol. Educ. B.*, no. 39, pp. 147–164, 2019.

[70] G. P. Dunn, L. J. Old, and R. D. Schreiber, "The immunobiology of cancer immunosurveillance and immunoediting," *Immunity*, vol. 21, no. 2, pp. 137–148, 2004.

[71] S. H. Kim *et al.*, "Prognostic impact of CD8 and programmed death-ligand 1 expression in patients with resectable non-small cell lung cancer," *Br. J. Cancer*, vol. 120, no. 5, pp. 547–554, 2019.

[72] M. Girardi *et al.*, "Regulation of cutaneous malignancy by γδ T cells," *J. Immunol.*, vol. 200, no. 9, pp. 3031–3035, 2018.

[73] V. Shankaran *et al.*, "IFNgamma and lympohcytes prevent primary tomour development and shape tomour immunogenicity," *Nature*, vol. 410, no. 6832, pp. 1107–11, 2001.

[74] N. M. Chapman and H. Chi, "Hallmarks of t-cell exit from quiescence," *Cancer Immunol. Res.*, vol. 6, no. 5, pp. 502–508, 2018.

[75] W. Liao, J. X. Lin, and W. J. Leonard, "Interleukin-2 at the Crossroads of Effector Responses, Tolerance, and Immunotherapy," *Immunity*, vol. 38, no. 1, pp. 13–25, 2013.

[76] D. Cibrián and F. Sánchez-Madrid, "CD69: from activation marker to metabolic gatekeeper,"

*Eur. J. Immunol.*, vol. 47, no. 6, pp. 946–953, 2017.

[77] L. R. Shiow *et al.*, "CD69 acts downstream of interferon-α/β to inhibit S1P 1 and lymphocyte egress from lymphoid organs," *Nature*, vol. 440, no. 7083, pp. 540–544, 2006.

[78] D. L. Farber, N. A. Yudanin, and N. P. Restifo, "Human memory T cells: Generation, compartmentalization and homeostasis," *Nat. Rev. Immunol.*, vol. 14, no. 1, pp. 24–35, 2014.

[79] S. D. Blackburn *et al.*, "Coregulation of CD8+ T cell exhaustion by multiple inhibitory receptors during chronic viral infection," *Nat. Immunol.*, vol. 10, no. 1, pp. 29–37, 2009.

[80] O. Khan *et al.*, "TOX transcriptionally and epigenetically programs CD8+ T cell exhaustion," *Nature*, vol. 571, no. 7764, pp. 211–218, 2019.

[81] M. Singer *et al.*, "A Distinct Gene Module for Dysfunction Uncoupled from Activation in Tumor-Infiltrating T Cells," *Cell*, vol. 166, no. 6, pp. 1500-1511.e9, 2016.

[82] B. C. Miller *et al.*, "Subsets of exhausted CD8+ T cells differentially mediate tumor control and respond to checkpoint blockade," *Nat. Immunol.*, vol. 20, no. 3, pp. 326–336, 2019.

[83] D. T. Utzschneider *et al.*, "T Cell Factor 1-Expressing Memory-like CD8+ T Cells Sustain the Immune Response to Chronic Viral Infections," *Immunity*, vol. 45, no. 2, pp. 415–427, 2016.

[84] I. Siddiqui *et al.*, "Intratumoral Tcf1 + PD-1 + CD8 + T Cells with Stem-like Properties Promote Tumor Control in Response to Vaccination and Checkpoint Blockade Immunotherapy," *Immunity*, vol. 50, no. 1, pp. 195-211.e10, 2019.

[85] C. U. Blank *et al.*, "Defining 'T cell exhaustion,'" *Nat. Rev. Immunol.*, vol. 19, no. 11, pp. 665–674, 2019.

[86] D. R. Sen *et al.*, "The epigenetic landscape of T cell exhaustion," vol. 354, no. 6316, pp. 1165–1169, 2016.

[87] L. M. Francisco, P. T. Sage, and A. H. Sharpe, "The PD-1 pathway in tolerance and autoimmunity," *Immunol. Rev.*, vol. 236, no. 1, pp. 219–242, 2010.

[88] J. Romo-Tena, D. Gómez-Martín, and J. Alcocer-Varela, "CTLA-4 and autoimmunity: New insights into the dual regulator of tolerance," *Autoimmun. Rev.*, vol. 12, no. 12, pp. 1171–1176, 2013.

[89] N. Verma, S. O. Burns, L. S. K. Walker, and D. M. Sansom, "Immune deficiency and autoimmunity in patients with CTLA-4 (CD152) mutations," *Clin. Exp. Immunol.*, vol. 190, no. 1, pp. 1–7, 2017.

[90] H. Ledford, H. Else, and M. Warren, "Cancer immunologists scoop medicine Nobel prize,"

*Nature*, vol. 562, no. 7725, pp. 20–21, 2018.

[91] J. Mizuguchi, "Regulation of immune responses through antigen receptors," *Annu. Rev. Immunol.*, vol. 73, no. 2, pp. 875–904, 1999.

[92] U. Lorenz, "SHP-1 and SHP-2 in T cells: two phosphatases functioning at many levels," *Immunol Rev*, vol. 46, no. 2, pp. 26–29, 2009.

[93] T. Okazaki and T. Honjo, "PD-1 and PD-1 ligands: From discovery to clinical application," *Int. Immunol.*, vol. 19, no. 7, pp. 813–824, 2007.

[94] C. Kao *et al.*, "Transcription factor T-bet represses expression of the inhibitory receptor PD-1 and sustains virus-specific CD8+ T cell responses during chronic infection," *Nat. Immunol.*, vol. 12, no. 7, pp. 663–671, 2011.

[95] B. G. Neel, H. Gu, and L. Pao, "The 'Shp'ing news: SH2 domain-containing tyrosine phosphatases in cell signaling," *Trends Biochem. Sci.*, vol. 28, no. 6, pp. 284–293, 2003.

[96] J. M. Chemnitz, R. V. Parry, K. E. Nichols, C. H. June, and J. L. Riley, "SHP-1 and SHP-2 Associate with Immunoreceptor Tyrosine-Based Switch Motif of Programmed Death 1 upon Primary Human T Cell Stimulation, but Only Receptor Ligation Prevents T Cell Activation," *J. Immunol.*, vol. 173, no. 2, pp. 945–954, 2004.

[97] T. Okazaki, A. Maeda, H. Nishimura, T. Kurosaki, and T. Honjo, "PD-1 immunoreceptor inhibits B cell receptor-mediated signaling by recruiting src homology 2-domain-containing tyrosine phosphatase 2 to phosphotyrosine," *Proc. Natl. Acad. Sci. U. S. A.*, vol. 98, no. 24, pp. 13866–13871, 2001.

[98] V. A. Boussiotis, "Molecular and biochemical aspects of the PD-1 checkpoint pathway," *N. Engl. J. Med.*, vol. 375, no. 18, pp. 1767–1778, 2016.

[99] N. Patsoukis *et al.*, "PD-1 alters T-cell metabolic reprogramming by inhibiting glycolysis and promoting lipolysis and fatty acid oxidation," *Nat. Commun.*, vol. 6, 2015.

[100] F. Wei, S. Zhong, Z. Ma, H. Kong, A. Medvec, and G. J. Freeman, "Strength of PD-1 signaling differentially affects T-cell effector functions," *PNAS*, vol. 110, no. 27, pp. 2–11, 2013.

[101] M. J. Butte, M. E. Keir, T. B. Phamduy, A. H. Sharpe, and G. J. Freeman, "Programmed Death-1 Ligand 1 Interacts Specifically with the B7-1 Costimulatory Molecule to Inhibit T Cell Responses," *Immunity*, vol. 27, no. 1, pp. 111–122, 2007.

[102] O. S. Qureshi *et al.*, "Trans-endocytosis of CD80 and CD86: A molecular basis for the cell-extrinsic function of CTLA-4," *Science (80-. ).*, vol. 332, no. 6029, pp. 600–603, 2011.

[103] E. Chuang *et al.*, "The CD28 and CTLA-4 receptors associate with the serine/threonine

phosphatase PP2A," *Immunity*, vol. 13, no. 3, pp. 313–322, 2000.

[104] M. C. Banton, K. L. Inder, E. Valk, C. E. Rudd, and H. Schneider, "Rab8 Binding to Immune Cell-Specific Adaptor LAX Facilitates Formation of trans-Golgi Network-Proximal CTLA-4 Vesicles for Surface Expression," *Mol. Cell. Biol.*, vol. 34, no. 8, pp. 1486–1499, 2014.

[105] M. Kisielow, J. Kisielow, G. Capoferri-Sollami, and K. Karjalainen, "Expression of lymphocyte activation gene 3 (LAG-3) on B cells is induced by T cells," *Eur. J. Immunol.*, vol. 35, no. 7, pp. 2081–2088, 2005.

[106] C. J. Workman *et al.*, "LAG-3 Regulates Plasmacytoid Dendritic Cell Homeostasis," *J. Immunol.*, vol. 182, no. 4, pp. 1885–1891, 2009.

[107] B. E. Baixeras *et al.*, "Characterization of the Lymphocyte Activation Gene 3-Encoded Protein. A New Ligand for Human Leukocyte Antigen Class II Antigens," *J. Exp. Med*, vol. 176, no. August, 1992.

[108] B. Huard *et al.*, "Characterization of the major histocompatibility complex class II binding site on LAG-3 protein," *Proc. Natl. Acad. Sci. U. S. A.*, vol. 94, no. 11, pp. 5744–5749, 1997.

[109] C. J. Workman, K. J. Dugger, and D. A. A. Vignali, "Cutting Edge: Molecular Analysis of the Negative Regulatory Function of Lymphocyte Activation Gene-3," *J. Immunol.*, vol. 169, no. 10, pp. 5392–5395, 2002.

[110] N. Iouzalen, S. Andreae, S. Hannier, and F. Triebel, "LAP, a lymphocyte activation gene-3 (LAG-3)-associated protein that binds to a repeated EP motif in the intracellular region of LAG-3, may participate in the down-regulation of the CD3/TCR activation pathway," *Eur. J. Immunol.*, vol. 31, no. 10, pp. 2885–2891, 2001.

[111] T. Kouo *et al.*, "Galectin-3 shapes antitumor immune responses by suppressing CD8 T Cells via LAG-3 and Inhibiting Expansion of Plasmacytoid Dendritic Cells," *Cancer Immunol. Res.*, vol. 3, no. 4, pp. 412–423, 2015.

[112] F. Xu *et al.*, "LSECtin expressed on melanoma cells promotes tumor progression by inhibiting antitumor T-cell responses," *Cancer Res.*, vol. 74, no. 13, pp. 3418–3428, 2014.

[113] J. Wang *et al.*, "Fibrinogen-like Protein 1 Is a Major Immune Inhibitory Ligand of LAG-3," *Cell*, vol. 176, no. 1–2, pp. 334-347.e12, 2019.

[114] M. Donia *et al.*, "Aberrant expression of MHC class II in melanoma attracts inflammatory tumor-specific CD4+T-cells, which dampen CD8+T-cell antitumor reactivity," *Cancer Res.*, vol. 75, no. 18, pp. 3747–3759, 2015.

[115] S. R. Woo *et al.*, "Immune inhibitory molecules LAG-3 and PD-1 synergistically regulate T-cell

function to promote tumoral immune escape," *Cancer Res.*, vol. 72, no. 4, pp. 917–927, 2012.

[116] L. Monney *et al.*, "Th1-specific cell surface protein Tim-3 regulates macrophage activation and severity of an autoimmune disease," *Nature*, vol. 415, no. 6871, pp. 536–541, 2002.

[117] A. C. Anderson *et al.*, "Promotion of tissue inflammation by the immune receptor Tim-3 expressed on innate immune cells," *Science (80-. ).*, vol. 318, no. 5853, pp. 1141–1143, 2007.

[118] J. Fourcade *et al.*, "Upregulation of Tim-3 and PD-1 expression is associated with tumor antigen-specific CD8+ T cell dysfunction in melanoma patients," *J. Exp. Med.*, vol. 207, no. 10, pp. 2175–2186, 2010.

[119] X. Gao *et al.*, "TIM-3 expression characterizes regulatory T cells in tumor tissues and is associated with lung cancer progression," *PLoS One*, vol. 7, no. 2, pp. 1–8, 2012.

[120] G. J. Freeman, J. M. Casasnovas, D. T. Umetsu, and R. H. Dekruyff, "TIM genes: A family of cell surface phosphatidylserine receptors that regulate innate and adaptive immunity," *Immunol. Rev.*, vol. 235, no. 1, pp. 172–189, 2010.

[121] C. Zhu *et al.*, "The Tim-3 ligand galectin-9 negatively regulates T helper type 1 immunity," *Nat. Immunol.*, vol. 6, no. 12, pp. 1245–1252, 2005.

[122] M. Rangachari *et al.*, "Bat3 promotes T cell responses and autoimmunity by repressing Tim-3-mediated cell death and exhaustion," *Nat. Med.*, vol. 18, no. 9, pp. 1394–1400, 2012.

[123] J. Lee *et al.*, "Phosphotyrosine-Dependent Coupling of Tim-3 to T-Cell Receptor Signaling Pathways," *Mol. Cell. Biol.*, vol. 31, no. 19, pp. 3963–3974, 2011.

[124] Y. H. Huang *et al.*, "CEACAM1 regulates TIM-3-mediated tolerance and exhaustion," *Nature*, vol. 517, no. 7534, pp. 386–390, 2015.

[125] Y. Zhang *et al.*, "Co-expression of TIM-3 and CEACAM1 promotes T cell exhaustion in colorectal cancer patients," *Int. Immunopharmacol.*, vol. 43, pp. 210–218, 2017.

[126] M. Nakayama *et al.*, "Tim-3 mediates phagocytosis of apoptotic cells and cross-presentation," *Blood*, vol. 113, no. 16, pp. 3821–3830, 2009.

[127] S. Chiba *et al.*, "Tumor-infiltrating DCs suppress nucleic acid-mediated innate immune responses through interactions between the receptor TIM-3 and the alarmin HMGB1," *Nat. Immunol.*, vol. 13, no. 9, pp. 832–842, 2012.

[128] K. Grabmeier-Pfistershammer *et al.*, "Antibodies targeting BTLA or TIM-3 enhance HIV-1 specific T cell responses in combination with PD-1 blockade," *Clin. Immunol.*, vol. 183, pp.

167–173, 2017.

[129] K. S. Boles *et al.*, “A novel molecular interaction for the adhesion of follicular CD4 T cells to follicular DC,” *Eur. J. Immunol.*, vol. 39, no. 3, pp. 695–703, 2009.

[130] S. D. Levin *et al.*, “Vstm3 is a member of the CD28 family and an important modulator of T-cell function,” *Eur. J. Immunol.*, vol. 41, no. 4, pp. 902–915, 2011.

[131] N. Joller *et al.*, “Cutting Edge: TIGIT Has T Cell-Intrinsic Inhibitory Functions,” *J. Immunol.*, vol. 186, no. 3, pp. 1338–1342, 2011.

[132] D. S. Thommen *et al.*, “A transcriptionally and functionally distinct pd-1 + cd8 + t cell pool with predictive potential in non-small-cell lung cancer treated with pd-1 blockade,” *Nat. Med.*, vol. 24, no. 7, 2018.

[133] A. C. Anderson, N. Joller, and V. K. Kuchroo, “Lag-3, Tim-3, and TIGIT: Co-inhibitory Receptors with Specialized Functions in Immune Regulation,” *Immunity*, vol. 44, no. 5, pp. 989–1004, 2016.

[134] B. Lorenzo Galluzzi, Erika Vacchelii, Pedro *et al.*, “Classification of current anticancer immunotherapies,” *Oncotarget*, vol. 5, no. 24, pp. 12472–12508.

[135] M. D. Hellmann *et al.*, “Nivolumab plus ipilimumab in advanced non-small-cell lung cancer,” *N. Engl. J. Med.*, vol. 381, no. 21, pp. 2020–2031, 2019.

[136] M. D. Suzanne L. Topalian, M.D., F. Stephen Hodi, M.D., Julie R. Brahmer, M.D., Scott N. Gettinger, M.D., David C. Smith, M.D., David F. McDermott, M.D., John D. Powderly, M.D., Richard D. Carvajal, M.D., Jeffrey A. Sosman, M.D., Michael B. Atkins, M.D., Philip, M. D. Scott J. Antonia, M.D., Ph.D., Leora Horn, M.D., Charles G. Drake, M.D., Ph.D., Drew M. Pardoll, M.D., Ph.D., Lieping Chen, M.D., Ph.D., William H. Sharfman, M.D., Robert A. Anders, M.D., Ph.D., Janis M. Taube, and M. D. Tracee L. McMiller, M.S., Haiying Xu, B.A., Alan J. Korman, Ph.D., Maria Jure-Kunkel, Ph.D., Shruti Agrawal, Ph.D., Daniel McDonald, M.B.A., Georgia D. Kollia, Ph.D., Ashok Gupta, M.D., Ph.D., Jon M. Wigginton, M.D., and Mario Sznol, “Safety, Activity, and Immune Correlates of Anti–PD-1 Antibody in Cancer,” *N. Engl. J. Med.*, vol. 366, no. 26, pp. 2443–2454, 2012.

[137] M. A. Postow, R. Sidlow, and M. D. Hellmann, “Immune-related adverse events associated with immune checkpoint blockade,” *N. Engl. J. Med.*, vol. 378, no. 2, pp. 158–168, 2018.

[138] K. Haratani *et al.*, “Association of immune-related adverse events with nivolumab efficacy in non-small cell lung cancer,” *JAMA Oncol.*, vol. 4, no. 3, pp. 374–378, 2018.

[139] L. P. Andrews, H. Yano, and D. A. A. Vignali, “Inhibitory receptors and ligands beyond PD-1,

PD-L1 and CTLA-4: breakthroughs or backups," *Nat. Immunol.*, vol. 20, no. 11, pp. 1425–1434, 2019.

[140] H. O. Alsaab *et al.*, "PD-1 and PD-L1 checkpoint signaling inhibition for cancer immunotherapy: mechanism, combinations, and clinical outcome," *Front. Pharmacol.*, vol. 8, no. AUG, pp. 1–15, 2017.

[141] P. A. Mayes, K. W. Hance, and A. Hoos, "The promise and challenges of immune agonist antibody development in cancer," *Nat. Rev. Drug Discov.*, vol. 17, no. 7, pp. 509–527, 2018.

[142] H. Borghaei *et al.*, "Nivolumab versus docetaxel in advanced nonsquamous non-small-cell lung cancer," *N. Engl. J. Med.*, vol. 373, no. 17, pp. 1627–1639, 2015.

[143] L. Gandhi *et al.*, "Pembrolizumab plus chemotherapy in metastatic non-small-cell lung cancer," *N. Engl. J. Med.*, vol. 378, no. 22, pp. 2078–2092, 2018.

[144] R. S. Herbst *et al.*, "Pembrolizumab versus docetaxel for previously treated, PD-L1-positive, advanced non-small-cell lung cancer (KEYNOTE-010): A randomised controlled trial," *Lancet*, vol. 387, no. 10027, pp. 1540–1550, 2016.

[145] J. A. Rehman *et al.*, "Quantitative and pathologist-read comparison of the heterogeneity of programmed death-ligand 1 (PD-L1) expression in non-small cell lung cancer," *Mod. Pathol.*, vol. 30, no. 3, pp. 340–349, 2017.

[146] D. L. Rimm *et al.*, "A prospective, multi-institutional, pathologist-based assessment of 4 immunohistochemistry assays for PD-L1 expression in non–small cell lung cancer," *JAMA Oncol.*, vol. 3, no. 8, pp. 1051–1058, 2017.

[147] F. R. Hirsch *et al.*, "PD-L1 Immunohistochemistry Assays for Lung Cancer: Results from Phase 1 of the Blueprint PD-L1 IHC Assay Comparison Project," *J. Thorac. Oncol.*, vol. 12, no. 2, pp. 208–222, 2017.

[148] R. Govindan *et al.*, "Genomic landscape of non-small cell lung cancer in smokers and never-smokers," *Cell*, vol. 150, no. 6, pp. 1121–1134, 2012.

[149] N. A. Rizvi *et al.*, "Mutational landscape determines sensitivity to PD-1 blockade in non-small cell lung cancer," *Science (80-. ).*, vol. 348, no. 6230, pp. 124–128, 2015.

[150] M. D. Hellmann *et al.*, "Tumor Mutational Burden and Efficacy of Nivolumab Monotherapy and in Combination with Ipilimumab in Small-Cell Lung Cancer," *Cancer Cell*, vol. 33, no. 5, pp. 853-861.e4, 2018.

[151] F. Pagès, J. Galon, M. C. Dieu-Nosjean, E. Tartour, C. Sautès-Fridman, and W. H. Fridman, "Immune infiltration in human tumors: A prognostic factor that should not be ignored,"

*Oncogene*, vol. 29, no. 8, pp. 1093–1102, 2010.

[152] S. Corgnac, M. Boutet, M. Kfoury, C. Naltet, and F. Mami-Chouaib, "The emerging role of CD8+ tissue resident memory T (TRM) cells in antitumor immunity: A unique functional contribution of the CD103 integrin," *Front. Immunol.*, vol. 9, no. AUG, 2018.

[153] A. Ribas *et al.*, "PD-1 Blockade Expands Intratumoral Memory T Cells," vol. 4, no. March, pp. 194–204, 2016.

[154] B. A. Helmink *et al.*, "B cells and tertiary lymphoid structures promote immunotherapy response.," *Nature*, no. February, 2020.

[155] F. Petitprez *et al.*, "B cells are associated with survival and immunotherapy response in sarcoma.," *Nature*, vol. 577, no. January, 2020.

[156] B. Routy *et al.*, "Gut microbiome influences efficacy of PD-1-based immunotherapy against epithelial tumors," *Science (80-. ).*, vol. 359, no. 6371, pp. 91–97, 2018.

[157] I. Ilan Youngster, MD, MMSc1; Erez Baruch, MD2; Lior Katz, MD3; Adi Lahat, MD2; Tal Brosh-Nissimov, MD4; Jacob Schachter, MD2; Omry Koren, PhD5; Gal Markel, MD, PhD2 and Ben Boursi, MD, PhD2; 1Shamir Medical Center, Nes Ziona, HaMerkaz, Israel; 2Sheba Medica and Session:, "Fecal Microbiota Transplantation in Metastatic Melanoma Patients Resistant to Anti-PD-1 Treatment," vol. 6, no. Suppl 2, p. 2019, 2019.

[158] A. Bachem *et al.*, "Microbiota-Derived Short-Chain Fatty Acids Promote the Memory Potential of Antigen-Activated CD8+ T Cells," *Immunity*, vol. 51, no. 2, pp. 285-297.e5, 2019.

[159] S. Gettinger *et al.*, "Impaired HLA class I antigen processing and presentation as a mechanism of acquired resistance to immune checkpoint inhibitors in lung cancer," *Cancer Discov.*, vol. 7, no. 12, pp. 1420–1435, 2017.

[160] H. Rizvi *et al.*, "Molecular determinants of response to anti-programmed cell death (PD)-1 and anti-programmed death-ligand 1 (PD-L1) blockade in patients with non-small-cell lung cancer profiled with targeted next-generation sequencing," *J. Clin. Oncol.*, vol. 36, no. 7, pp. 633–641, 2018.

[161] T. N. Schumacher and R. D. Schreiber, "Neoantigens in cancer immunotherapy," *Science (80-. ).*, vol. 348, no. 6230, pp. 69–74, 2015.

[162] M. S. Rooney, S. A. Shukla, C. J. Wu, G. Getz, and N. Hacohen, "Molecular and genetic properties of tumors associated with local immune cytolytic activity," *Cell*, vol. 160, no. 1–2, pp. 48–61, 2015.

[163] T. K. Kim, R. S. Herbst, and L. Chen, "Defining and Understanding Adaptive Resistance in

Cancer Immunotherapy," *Trends Immunol.*, vol. 39, no. 8, pp. 624–631, 2018.

[164] C. Pereira *et al.*, " Genomic Profiling of Patient-Derived Xenografts for Lung Cancer Identifies B2M Inactivation Impairing Immunorecognition ," *Clin. Cancer Res.*, vol. 23, no. 12, pp. 3203–3213, 2017.

[165] A. Garcia-Diaz *et al.*, "Interferon Receptor Signaling Pathways Regulating PD-L1 and PD-L2 Expression," *Cell Rep.*, vol. 19, no. 6, pp. 1189–1201, 2017.

[166] P. Sharma, S. Hu-Lieskovan, J. A. Wargo, and A. Ribas, "Primary, Adaptive, and Acquired Resistance to Cancer Immunotherapy," *Cell*, vol. 168, no. 4, pp. 707–723, 2017.

[167] S. Spranger, R. Bao, and T. F. Gajewski, "Melanoma-intrinsic β-catenin signalling prevents anti-tumour immunity," *Nature*, vol. 523, no. 7559, pp. 231–235, 2015.

[168] and A. Z. Daniela S. Thommen1,2, Jens Schreiner2, Philipp M€uller2, Petra Herzig2, Andreas Roller3, Anton Belousov3, Pablo Umana4, Pavel Pisa4, Christian Klein4, Marina Bacac4, Ozana S. Fischer5, Wolfgang Moersig5, Spasenija Savic Prince6, Victor Levitsky4, Vaios K, "Progression of Lung Cancer Is Associated with Increased Dysfunction of T Cells De fi ned by Coexpression of Multiple Inhibitory Receptors," vol. 3, no. December, pp. 1344–1356, 2015.

[169] R. Y. Huang, A. Francois, A. R. McGray, A. Miliotto, and K. Odunsi, "Compensatory upregulation of PD-1, LAG-3, and CTLA-4 limits the efficacy of single-agent checkpoint blockade in metastatic ovarian cancer," *Oncoimmunology*, vol. 6, no. 1, 2017.

[170] G. Shayan, R. Srivastava, J. Li, N. Schmitt, P. Kane, and R. L. Ferris, "Adaptive resistance to anti-PD1 therapy by Tim-3 upregulation is mediated by the PI3K-Akt pathway in head and neck cancer," *Oncoimmunology*, vol. 6, no. 1, pp. 1–11, 2017.

[171] S. Koyama *et al.*, "Adaptive resistance to therapeutic PD-1 blockade is associated with upregulation of alternative immune checkpoints," *Nat. Commun.*, vol. 7, pp. 1–9, 2016.

[172] S. J. Turley, V. Cremasco, and J. L. Astarita, "Immunological hallmarks of stromal cells in the tumour microenvironment," *Nat. Publ. Gr.*, vol. 15, no. November, 2015.

[173] C. H. Wong, K. W. Siah, and A. W. Lo, "Estimation of clinical trial success rates and related parameters," *Biostatistics*, vol. 20, no. 2, pp. 273–286, 2019.

[174] G. Ross, "Observations on the living developing nerve fiber .," *SOCXETY Exp. BIOOGY Med.*, vol. 98, no. 241, 1906.

[175] M. E. Katt, A. L. Placone, A. D. Wong, Z. S. Xu, and P. C. Searson, "In vitro tumor models: Advantages, disadvantages, variables, and selecting the right platform," *Front. Bioeng. Biotechnol.*, vol. 4, no. FEB, 2016.

[176] J. G. Rheinwald and H. Green, “Serial cultivation of strains of human epidermal keratinocytes in defined clonal and serum-free culture,” *J Invest Dermatol*, vol. 6, pp. 331–344, 1975.

[177] K. Lindberg, M. E. Brown, H. V. Chaves, K. R. Kenyon, and J. G. Rheinwald, “In vitro propagation of human ocular surface epithelial cells for transplantation,” *Investig. Ophthalmol. Vis. Sci.*, vol. 34, no. 9, pp. 2672–2679, 1993.

[178] M. A. Lancaster and J. A. Knoblich, “Organogenesis in a dish: Modeling development and disease using organoid technologies,” *Science (80-. ).*, vol. 345, no. 6194, 2014.

[179] G. Vlachogiannis *et al.*, “Patient-derived organoids model treatment response of metastatic gastrointestinal cancers,” *Science (80-. ).*, vol. 359, no. February, pp. 920–926, 2018.

[180] N. Sachs *et al.*, “A Living Biobank of Breast Cancer Organoids Captures Disease Heterogeneity,” *Cell*, vol. 172, no. 1–2, pp. 373-386.e10, 2018.

[181] N. Sachs *et al.*, “Long-term expanding human airway organoids for disease modeling,” *EMBO J.*, vol. 38, no. 4, pp. 1–20, 2019.

[182] M. Kim *et al.*, “Patient-derived lung cancer organoids as in vitro cancer models for therapeutic screening,” *Nat. Commun.*, vol. 10, no. 1, 2019.

[183] M. C. Rosales Gerpe *et al.*, “Use of Precision-Cut Lung Slices as an Ex Vivo Tool for Evaluating Viruses and Viral Vectors for Gene and Oncolytic Therapy,” *Mol. Ther. - Methods Clin. Dev.*, vol. 10, no. September, pp. 245–256, 2018.

[184] H. Salmon *et al.*, “Matrix architecture defines the preferential localization and migration of T cells into the stroma of human lung tumors,” *J. Clin. Invest.*, vol. 122, no. 3, pp. 899–910, 2012.

[185] E. Peranzoni *et al.*, “Macrophages impede CD8 T cells from reaching tumor cells and limit the efficacy of anti–PD-1 treatment,” *Proc. Natl. Acad. Sci. U. S. A.*, vol. 115, no. 17, pp. E4041–E4050, 2018.

[186] S. Z. Martin *et al.*, “Ex vivo tissue slice culture system to measure drug-response rates of hepatic metastatic colorectal cancer,” *BMC Cancer*, vol. 19, no. 1, pp. 1–14, 2019.

[187] A. F. Van De Merbel *et al.*, “An ex vivo tissue culture model for the assessment of individualized drug responses in prostate and bladder cancer,” *Front. Oncol.*, vol. 8, no. OCT, pp. 1–8, 2018.

[188] E. Karekla *et al.*, “Ex Vivo explant cultures of non-small cell lung carcinoma enable evaluation of primary tumor responses to anticancer therapy,” *Cancer Res.*, vol. 77, no. 8,

pp. 2029–2039, 2017.

[189] 4* Dongeun Huh,1,2 Benjamin D. Matthews,2,3 Akiko Mammoto,2 Martín Montoya-Zavala,1,2 Hong Yuan Hsin,2 Donald E. Ingber1,2, “Reconstituting Organ-Level Lung Functions on a Chip,” *Science (80-. ).*, no. June, pp. 1662–1668, 2010.

[190] K. H. Benam *et al.*, “Small airway-on-a-chip enables analysis of human lung inflammation and drug responses in vitro,” *Nat. Methods*, vol. 13, no. 2, pp. 151–157, 2016.

[191] A. Jain *et al.*, “Primary Human Lung Alveolus-on-a-chip Model of Intravascular Thrombosis for Assessment of Therapeutics,” *Clin. Pharmacol. Ther.*, vol. 103, no. 2, pp. 332–340, 2018.

[192] D. Huh *et al.*, “A human disease model of drug toxicity-induced pulmonary edema in a lung-on-a-chip microdevice,” *Sci. Transl. Med.*, vol. 4, no. 159, 2012.

[193] M. J. S. Benjamin M. Davis, Glen F. Rall, “Microfluidics: A new tool for modeling cancer-immune interactions,” *Trends Cancer*, vol. 176, no. 1, pp. 139–148, 2017.

[194] I. K. Zervantonakis, S. K. Hughes-Alford, J. L. Charest, J. S. Condeelis, F. B. Gertler, and R. D. Kamm, “Three-dimensional microfluidic model for tumor cell intravasation and endothelial barrier function,” *Proc. Natl. Acad. Sci. U. S. A.*, vol. 109, no. 34, pp. 13515–13520, 2012.

[195] J. S. Jeon, I. K. Zervantonakis, S. Chung, R. D. Kamm, and J. L. Charest, “In Vitro Model of Tumor Cell Extravasation,” *PLoS One*, vol. 8, no. 2, 2013.

[196] D. H. T. Nguyen *et al.*, “Biomimetic model to reconstitute angiogenic sprouting morphogenesis in vitro,” *Proc. Natl. Acad. Sci. U. S. A.*, vol. 110, no. 17, pp. 6712–6717, 2013.

[197] * Yoonseok Choi2,¶, Eunjeh Hyun3,¶, Jeongyun Seo1, Cassidy Blundell1, Hee Chan Kim4, Eunhee Lee2, Suhyun Lee2, Aree Moon5, Woo Kyung Moon2,*, and Dongeun Huh1, “A microengineered pathophysiological model of early-stage breast cancer,” *Syst. Biol. Cancer*, vol. 15, no. 16, pp. 345–360, 2015.

[198] B. A. Hassell *et al.*, “Human Organ Chip Models Recapitulate Orthotopic Lung Cancer Growth, Therapeutic Responses, and Tumor Dormancy In Vitro,” *Cell Rep.*, vol. 21, no. 2, pp. 508–516, 2017.

[199] K. E. Sung and D. J. Beebe, “Microfluidic 3D models of cancer,” *Adv. Drug Deliv. Rev.*, vol. 79, pp. 68–78, 2014.

[200] S. Kim, H. Lee, M. Chung, and N. L. Jeon, “Engineering of functional, perfusable 3D microvascular networks on a chip,” *Lab Chip*, vol. 13, no. 8, pp. 1489–1500, 2013.

[201] E. Agliari *et al.*, “Cancer-driven dynamics of immune cells in a microfluidic environment,”

*Sci. Rep.*, vol. 4, pp. 11–13, 2014.

[202] L. Businaro *et al.*, "Cross talk between cancer and immune cells: Exploring complex dynamics in a microfluidic environment," *Lab Chip*, vol. 13, no. 2, pp. 229–239, 2013.

[203] M. Nguyen *et al.*, "Dissecting Effects of Anti-cancer Drugs and Cancer-Associated Fibroblasts by On-Chip Reconstitution of Immunocompetent Tumor Microenvironments," *Cell Rep.*, vol. 25, no. 13, pp. 3884-3893.e3, 2018.

[204] A. R. Aref *et al.*, "3D microfluidic: Ex vivo culture of organotypic tumor spheroids to model immune checkpoint blockade," *Lab Chip*, vol. 18, no. 20, pp. 3129–3143, 2018.

[205] H. Echchakir *et al.*, "Evidence for in situ expansion of diverse antitumor-specific cytotoxic T lymphocyte clones in a human large cell carcinoma of the lung," vol. 12, no. 4, pp. 537–546, 2000.

[206] K. Ichinokawa *et al.*, "Downregulated expression of human leukocyte antigen class I heavy chain is associated with poor prognosis in non-small-cell lung cancer," *Oncol. Lett.*, vol. 18, no. 1, pp. 117–126, 2019.

[207] Y. He *et al.*, "MHC class II expression in lung cancer," *Lung Cancer*, vol. 112, no. July, pp. 75–80, 2017.

[208] L. Jiang *et al.*, "PD-L1 expression and its relationship with oncogenic drivers in non-small cell lung cancer (NSCLC)," *Oncotarget*, vol. 8, no. 16, pp. 26845–26857, 2017.

[209] A. Le Floc'h *et al.*, "αEβ7 integrin interaction with E-cadherin promotes antitumor CTL activity by triggering lytic granule polarization and exocytosis," *J. Exp. Med.*, vol. 204, no. 3, pp. 559–570, 2007.

[210] G. Dorothée *et al.*, " Tumor-Infiltrating CD4 + T Lymphocytes Express APO2 Ligand (APO2L)/TRAIL upon Specific Stimulation with Autologous Lung Carcinoma Cells: Role of IFN-α on APO2L/TRAIL Expression and -Mediated Cytotoxicity ," *J. Immunol.*, vol. 169, no. 2, pp. 809–817, 2002.

[211] H. N. Chia, M. Vigen, and A. M. Kasko, "Effect of substrate stiffness on pulmonary fibroblast activation by TGF-β," *Acta Biomater.*, vol. 8, no. 7, pp. 2602–2611, 2012.

[212] X. Huang *et al.*, "Matrix stiffness-induced myofibroblast differentiation is mediated by intrinsic mechanotransduction," *Am. J. Respir. Cell Mol. Biol.*, vol. 47, no. 3, pp. 340–348, 2012.

[213] C. Van Dang, "The half-Lives of facts, paradigm shifts, and reproducibility in cancer research," *Cancer Res.*, vol. 78, no. 15, pp. 4105–4106, 2018.

[214] H. J. Kim, D. Huh, G. Hamilton, and D. E. Ingber, “Human gut-on-a-chip inhabited by microbial flora that experiences intestinal peristalsis-like motions and flow,” *Lab Chip*, vol. 12, no. 12, pp. 2165–2174, 2012.

[215] D. Bovard *et al.*, “A lung/liver-on-a-chip platform for acute and chronic toxicity studies,” *Lab Chip*, vol. 18, no. 24, pp. 3814–3829, 2018.

[216] N. R. Wevers *et al.*, “A perfused human blood-brain barrier on-a-chip for high-throughput assessment of barrier function and antibody transport,” *Fluids Barriers CNS*, vol. 15, no. 1, pp. 1–12, 2018.

[217] S. Hao *et al.*, “A Spontaneous 3D Bone-On-a-Chip for Bone Metastasis Study of Breast Cancer Cells,” *Small*, vol. 14, no. 12, pp. 1–10, 2018.

[218] J. M. Garcia-Arcos *et al.*, “Reconstitution of cell migration at a glance,” *J. Cell Sci.*, vol. 132, no. 4, pp. 0–2, 2019.

[219] M. R. Elliott and K. S. Ravichandran, “The Dynamics of Apoptotic Cell Clearance,” *Dev. Cell*, vol. 38, no. 2, pp. 147–160, 2016.

[220] R. Tang, M. Rangachari, and V. K. Kuchroo, “Tim-3: A co-receptor with diverse roles in T cell exhaustion and tolerance,” *Semin. Immunol.*, vol. 42, no. August, p. 101302, 2019.

[221] M. C. Comes *et al.*, “The influence of spatial and temporal resolutions on the analysis of cell-cell interaction: a systematic study for time-lapse microscopy applications,” *Sci. Rep.*, vol. 9, no. 1, pp. 1–11, 2019.

[222] A. Mencattini *et al.*, “Discovering the hidden messages within cell trajectories using a deep learning approach for in vitro evaluation of cancer drug treatments,” *Sci. Rep.*, vol. 10, no. 1, pp. 1–11, 2020.

[223] H. Su *et al.*, “Characterization of TIM-3 expression and its prognostic value in patients with surgically resected lung adenocarcinoma,” *Lung Cancer*, vol. 121, no. April, pp. 18–24, 2018.

université PARIS-SACLAY | ÉCOLE DOCTORALE Cancérologie : biologie - médecine - santé (CBMS)

**Titre :** Caractérisation de la réponse à l'immunothérapie sur puce microfluidique dans un modèle de cancer du poumon

**Mots clés :** cancérologie, immunothérapie, médecine de précision, microfluidique, tumeurs-sur-puce

**Résumé :** Le cancer du poumon non à petites cellules (CPNPC) est l'une des rares maladies tumorales, avec mélanome et carcinome vésical, pour lesquelles les médicaments immuno-oncologiques ont conduit à une révolution thérapeutique. Seuls 20 à 30% des patients atteints de CPNPC bénéficient de la monothérapie avec inhibiteurs des points de contrôle immunitaires (ICP) avec des réponses durables, tandis que les combinaisons ont conduit à réponse longue dans jusqu'à 40% des patients. Notre étude vise à mieux caractériser la modulation du microenvironnement tumoral lors d'un traitement ICP, plus ou moins une chimiothérapie concomitante, afin de guider des stratégies d'immunothérapie plus convaincantes.

Inspiré par la technologie d'organes sur puce, nous avons reconstitué *ex vivo* un microenvironnement de tumeur pulmonaire immunocompétent simplifié en réalisant des co-cultures 3D dans des dispositifs microfluidiques. Cette approche nous a permis de réaliser une imagerie en direct et une quantification des effets de l'ICP sur l'écosystème tumoral.

L'architecture de la puce se compose de trois micro-chambres parallèles, séparées par des micro-piliers qui permettent le confinement d'un hydrogel biomimétique dans le canal central par capillarité. En co-cultivant des cellules CPNPC et des lymphocytes T cytotoxiques autologues (récoltés à partir des TIL du même patient et amplifiés ultérieurement *in vitro*), nous pourrions récapituler, visualiser et quantifier une activité cytotoxique efficace et spécifique des cellules T contre les cellules cancéreuses autologues.

Pour cela, nous avons développé un nouvel algorithme qui pourrait localiser les cellules cancéreuses et, grâce à un rapporteur fluorescent de l'activité caspase, mesurer leur mort d'une manière spécifique au temps et à l'espace. Dans ces co-cultures 3D, l'activité cytotoxique des cellules T a été renforcée par le traitement avec l'inhibiteur PD-1 et l'inhibiteur PD-L1, reconstituant ainsi sur puce une réponse ICI.

De plus, cette méthode nous a permis d'extraire un paramètre, le potentiel d'induction de la mort, qui estime mathématiquement la «contagiosité de la mort» en calculant la proximité dans l'espace et le temps des signaux de mort.

Fait intéressant, cette analyse nous a révélé que la mort des cellules cancéreuses causée par la chimiothérapie ou par les cellules T cytotoxiques est contagieuse, alors que dans les conditions témoins, la mort des cellules cancéreuses est stochastique. De plus, afin d'avoir un aperçu moléculaire de l'impact de la co-culture sur les cellules T, en présence ou en l'absence d'ICI, nous avons analysé par cytométrie de flux l'expression de plusieurs marqueurs de cellules T. Après 3 jours de co-culture sur puce, les lymphocytes T ont montré une expression accrue des marqueurs d'activation, tels que CD69 et CD25, ainsi qu'une augmentation de l'expression des marqueurs d'épuisement, notamment PD-1, TIGIT, TIM-3, LAG- 3, CD137 et OX-40.

Le couplage de l'analyse d'image et de l'étude de la plasticité des lymphocytes T, nous a permis d'associer pour la première fois l'activité cytotoxique finement quantifiée des lymphocytes T avec leur statut d'activation / épuisement et de décrire un phénotype réactif aux immunothérapies.

Dans cette thèse, nous avons démontré que la tumeur-sur-puce peut être exploité pour évaluer l'efficacité des inhibiteurs de points de contrôle immunitaires, potentiellement pour déterminer l'effet de médicaments combinés et enfin pour étudier les mécanismes de résistance primaire des cellules cancéreuses.

**Université Paris-Saclay**
Espace Technologique / Immeuble Discovery
Route de l'Orme aux Merisiers RD 128 / 91190 Saint-Aubin, France

université PARIS-SACLAY | ÉCOLE DOCTORALE Cancérologie : biologie - médecine - santé (CBMS)

**Title :** Lung cancer on-chip for immunotherapy response profiling

**Keywords :** cancerology, immunotherapy, precision medicine, microfluidics, tumors-on-chip

Non-small cell lung cancer (NSCLC) is one of the few tumor diseases, with melanoma and vesical carcinoma, for which immuno-oncology drugs led to a therapeutic revolution. Only 20 to 30% of the NSCLC patients benefit from immune checkpoint inhibitors (ICI) monotherapy with durable responses, while combinations led up to 40% of long responder patients. Our study aims to better characterize the modulation of the tumor microenvironment upon ICI treatment, plus or minus concurrent chemotherapy, in order to guide more compelling immunotherapy strategies.

Inspired by the organ-on-a-chip technology, we implemented the reconstitution ex vivo of a simplified immunocompetent lung tumor microenvironment by performing 3D co-cultures in microfluidic devices. This approach allowed us to perform live-imaging and quantification of the effects of ICI on the tumor ecosystem. The design of the chip consists of three parallel micro-chambers, separated by micro-pillars that allow the confinement of a biomimetic hydrogel in the central channel by capillarity.

By co-culturing autologous NSCLC cells and cytotoxic T lymphocytes (harvested from the TILs of the same patient and furtherly amplified in vitro) we could recapitulate, visualize and quantify an efficient and specific cytotoxic activity of the T cells against the autologous cancer cells. For this purpose, we developed a novel algorithm that could localize the cancer cells and, thanks to a fluorescent reporter of the caspase activity, measure their death in a time- and space-specific manner.

In these 3D co-cultures the cytotoxic activity of T cells was enhanced by the treatment with PD-1 inhibitor and PD-L1 inhibitor, therefore reconstituting on-chip an ICI response. Furthermore, this method allowed us to extract a parameter, the potential of death induction, which mathematically estimates the "contagiousness of death" by computing the proximity in space and time of death signals. Interestingly, this analysis revealed us that the death of cancer cells caused by either chemotherapy or cytotoxic T cells is contagious, whereas in control conditions the cancer cells death is stochastic.

Furthermore, in order to have a molecular insight on the impact of the co-culture on T cells, in presence or absence of ICI, we analyzed by flow cytometry the expression of several T cell markers. After 3 days of co-culture on chip, the T cells showed an increased expression of activation markers, such as CD69 and CD25, as well as an increased expression of exhaustion markers, notably PD-1, TIGIT, TIM-3, LAG-3, CD137 and OX-40. The coupling of image analysis and the study of T cell plasticity, allowed us to associate for the first time the finely quantified cytotoxic activity of the T cells and their activation/exhaustion status and describe a responsive phenotype to immunotherapies.

In this thesis, we demonstrated that the tumor-on-chip is suitable to evaluate the efficacy of immune checkpoint inhibitors, to potentially assess the effect of combined drugs and to study the mechanisms of cancer cell primary resistance.